

This is to certify that the
dissertation entitled

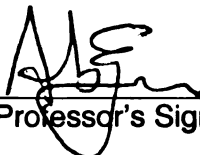
IMPELLER-DIFFUSER-VOLUTE MODELING AND FLOW
ANALYSIS TOGETHER WITH TEST VALIDATION

presented by

YINGHUI DAI

has been accepted towards fulfillment
of the requirements for the

Ph.D. degree in Mechanical Engineering



Major Professor's Signature

08/19/04

Date



PLACE IN RETURN BOX to remove this checkout from your record.
TO AVOID FINES return on or before date due.
MAY BE RECALLED with earlier due date if requested.

DATE DUE	DATE DUE	DATE DUE

**IMPELLER-DIFFUSER-VOLUTE MODELING AND FLOW
ANALYSIS TOGETHER WITH TEST VALIDATION**

By

Yinghui Dai

A DISSERTATION

Submitted to
Michigan State University
in partial fulfillment of the requirements
for the degree of

DOCTOR OF PHILOSOPHY

Department of Mechanical Engineering

2004

ABSTRACT

IMPELLER-DIFFUSER-VOLUTE MODELING AND FLOW ANALYSIS TOGETHER WITH TEST VALIDATION

By

Yinghui Dai

Although the axial flow compressor is preferred for the increasingly larger engines which are required for aircraft propulsion, the efficiency of axial compressors drops sharply at very low air mass flow rates and the blade is small and difficult to manufacture accurately. Under this situation, centrifugal compressors are widely used.

One of the main objectives of turbomachinery researchers is to design a compact, efficient and uniform circumferential pressure distribution volute. It is well known that non-uniform static pressure variation along the impeller periphery due to the volute can influent the flow inside the impeller and hurt the efficiency of the whole machine. And, the non-uniform static pressure distribution also creates radial forces on the impeller shaft and it might end up with the failure of the bearings because of too much loading. So, the volute study is very important for the centrifugal compressor design process.

An integrated tool that includes the volute and diffuser grids generation is introduced in this study. For a new case, this tool can also create the sub-grid attachment/append, boundary condition definition, initial guess, time-step selection and post-processing automatically. Two new functions for the volute/impeller interaction study and performance improvement are added in the integrated tool, too. They are very

helpful for the volute design. It has been proved that this integrated tool is very effective and pretty robust in the practical application.

With the help of this tool, this study presents the experimental and numerical investigation on the matching of four different overhung volutes with four different impellers that are used for pipeline applications. Two computational models, “stage” and “frozen” model using the k- ϵ turbulence model and the wall function built in the commercially available CFD software TASCFlow, have been used to predict the internal flow of all the compressor configurations. A good agreement between experimental data and numerical simulation results is found. The overall/component performance and the flow structure in the impeller, diffuser and volute are also discussed in detail.

The influences of some key geometry parameters on the compressor performance are also investigated. Since the experiment test is only from flange to flange, diffuser stall and volute stall phenomenon can only be explained from the CFD results. For different cases, some suggestions have been proposed to improve the compressor performance based on the CFD analysis.

Copyright by
Yinghui Dai
2004

ACKNOWLEDGMENTS

I express my sincerest gratitude to my advisor, Professor Abraham Engeda at Michigan State University, for his elaborate outline of this project, advices, assistance and encouragement.

I would like to thank Professors Indrek Wichman, Professor Norbert Müller, and Professor Chichia Chiu for their suggestions, discussions and interest in this project that made this work possible.

I am also very thankful to Mr. Michael Cave, Dr. Jean-Luc Di Liberti, Mr. Ed Fowler, Mr. Tim David and Mr. Johnathan Burningham at Solar Turbines, Inc. and Dr. Fahua Gu at Concept NREC for their great help and fruitful discussions.

Thanks are also extended to Mr. Donghui Zhang, Mr. Faisal Mahroogi, Mr. Zeyad Alsuhaibani, Mr. Mukarram Raheel, Mr. Jaewook Song, and all other students at the turbomachinery lab at Michigan State University.

Last, but by no means least, I would like to thank my wife, Xiaoling Sheng, my parents, Shanwu Xu and Zequn Dong, my daughter, Connie Dai, whose quiet patience and support enabled this dissertation to be prepared.

TABLE OF CONTENTS

LIST OF FIGURES	VIII
NOMENCLATURE	XII
CHAPTER 1	1
INTRODUCTION.....	1
1.1 HISTORY AND APPLICATIONS.....	1
1.2 CENTRIFUGAL COMPRESSOR COMPONENTS	3
1.3 THE PURPOSE OF VOLUTE STUDY	4
1.4 OBJECTIVES OF THE CURRENT STUDY	5
CHAPTER 2	8
LITERATURE SURVEY	8
2.1 INTRODUCTION.....	8
2.2 VOLUTE ALONE STUDY.....	9
2.2.1 <i>Flow model in volute</i>	9
2.2.2 <i>Loss mechanisms inside volute</i>	14
2.3 THE INTERACTION BETWEEN VOLUTE AND OTHER COMPONENTS.....	22
2.3.1 <i>Influence of volute geometrical parameters on compressor performance</i>	22
2.3.1.3 <i>Radial Position of the Cross Section</i>	39
2.3.1.4 <i>Tongue Geometry</i>	40
2.3.1.5 <i>Radial Forces</i>	40
2.4 THE VELOCITY AND PRESSURE DISTRIBUTION IN VOLUTE	43
CHAPTER 3	49
THEORY BACKGROUND AND THE INTEGRATED TOOL DEVELOPMENT	49
3.1 COMPUTATIONAL METHODS AND CFD MODELS.....	49
3.1.1 <i>Turbulence Model--k - ϵ model</i>	49
3.1.2 <i>Two CFD models for centrifugal compressors</i>	51
3.2 INTEGRATED TOOL DEVELOPMENT	57
3.2.1 <i>Sub-grid generation</i>	57
3.2.2 <i>Sub-grids attachment and append</i>	58
3.2.3 <i>Boundary Conditions</i>	60
3.2.4 <i>Initial guess</i>	61
3.2.5 <i>Post-processing</i>	63
3.3 CODE ROBUSTNESS AND GRID IMPROVEMENT.....	65
3.3.1 <i>Code robustness</i>	65
3.3.2 <i>Two new functions in the code</i>	66
3.3.3 <i>Grid quality improvement</i>	68
3.4 AERO TEST FACILITY	70
CHAPTER 4	73

SOLUTION REPEATABILITY AND PREVIOUS WORK VERIFICATION	73
4.1 INTRODUCTION	73
4.2 THE STUDY FOR D3-1 COMPRESSOR	73
4.3 THE STUDY FOR D2 COMPRESSOR.....	86
CONCLUSIONS	90
CHAPTER 5	94
PERFORMANCE INVESTIGATION OF TWO DIFFERENT VOLUTES AND SAME IMPELLER	94
5.1 INTRODUCTION	94
5.2 THE INVESTIGATED COMPRESSORS	96
5.3 TEST FACILITY AND TEST PROCEDURE.....	98
5.4 COMPUTATIONAL METHOD	99
5.5 RESULTS AND DISCUSSIONS	101
5.5.1 <i>Compressor Performance</i>	102
5.5.2 <i>Impeller and Vaneless Diffuser Performance</i>	107
5.5.3 <i>Volute Performance</i>	114
CONCLUSIONS	118
CHAPTER 6	120
FLOW STRUCTURES INVESTIGATION AND COMPARISON.....	120
6.1 INTRODUCTION	120
6.2 COMPRESSOR GEOMETRY AND COMPUTATIONAL METHOD	123
6.3 TEST FACILITY AND EXPERIMENTAL METHOD	125
6.4 RESULTS AND DISCUSSION.....	126
CONCLUSIONS	145
BIBLIOGRAPHY	147

LIST OF FIGURES

FIGURE 1.1 A SINGLE STAGE CENTRIFUGAL COMPRESSOR	4
FIGURE 2.1 STRAIGHT VOLUTE MODEL IN VAN DEN BRAEMBUSSCHE EXPERIMENT (1990) 10	
FIGURE 2.2 SUPERPOSITION OF VORTEX TUBES IN A VOLUTE (1990)	10
FIGURE 2.3 PARTICLE TRACING INSIDE THE VANELESS DIFFUSER AND VOLUTE (1994)	11
FIGURE 2.4 SWIRL VELOCITY (A) AND TOTAL PRESSURE (B) DISTRIBUTION	13
AT MEDIUM MASS FLOW	13
FIGURE 2.5 VOLUTE PRESSURE RECOVERY COEFFICIENT COMPARISON OF THEORY AND DATA (AFTER JAPIKSE, 1982)	17
FIGURE 2.6 VOLUTE PRESSURE LOSS COEFFICIENT COMPARISON OF THEORY AND DATA....	17
(AFTER JAPIKSE, 1982)	17
FIGURE 2.7 TYPES OF VOLUTES	25
FIGURE 2.8 PERFORMANCE WITH MINIMUM AREA (AFTER LOPEZ PENA, 1987)	26
FIGURE 2.9 STATIC PRESSURE DISTRIBUTION ALONG THE VOLUTE AND DIFFUSER OF THE STANDARD COMPRESSOR	27
FIGURE 2.10 PERFORMANCE WITH MEDIUM AREA	29
FIGURE 2.11 PERFORMANCE WITH MAXIMUM AREA	31
FIGURE 2.12 COMPRESSOR PERFORMANCE MAP	33
FIGURE 2.13 CROSS SECTIONS OF VOLUTES	34
FIGURE 2.14 TOTAL PRESSURE RATIO OF COMPRESSOR WITH DIFFERENT VOLUTES AT ACTUAL TIP SPEEDS OF 700 TO 1300 FEET PER SECOND	35
FIGURE 2.15 GLOBAL PUMP CHARACTERISTICS WITH SYMMETRIC AND ASYMMETRIC VOLUTE	36
FIGURE 2.16 COMPARISON OF PERFORMANCE FOR DIFFERENT VOLUTE GEOMETRIES	37
FIGURE 2.17 EFFECT OF CROSS-SECTIONAL SHAPES ON SCROLL PERFORMANCE.....	38
FIGURE 2.18 MEASURED VELOCITY AND PRESSURE FOR SMALL MASS FLOW	43

FIGURE 2.19 MEASURED VELOCITY AND PRESSURE FOR OPTIMUM MASS FLOW	44
FIGURE 2.20 MEASURED VELOCITY AND PRESSURE FOR LARGE MASS FLOW	45
FIGURE 2.21 LONGITUDINAL AND CIRCUMFERENTIAL STATIC PRESSURE VARIATION CORRESPONDING TO SMALL (A), OPTIMUM (B) AND LARGE (C) MASS FLOW	48
FIGURE 3.1 THE STAGE ROTOR.....	54
FIGURE 3.2 THE FROZEN ROTOR.....	56
FIGURE 3.3 BUTTERFLY GRID OF VOLUTE.....	58
FIGURE 3.4 AVERAGED AREA AT DIFFUSER OUTLET	65
FIGURE 3.5 ONE EXAMPLE OF CODE ROBUSTNESS	65
FIGURE 3.6 ENLARGED VOLUTE	67
FIGURE 3.7 REDUCED-WIDTH VANELESS DIFFUSER	68
FIGURE 3.8 GRID IMPROVEMENT (1).....	69
FIGURE 3.9 GRID IMPROVEMENT (2).....	70
FIGURE 4.1 COMPRESSOR PERFORMANCE.....	74
FIGURE 4.2 EFFICIENCY OF DIFFERENT STATIONS AT DIFFERENT MASS FLOWS	75
FIGURE 4.3 TOTAL PRESSURE OF DIFFERENT STATIONS AT DIFFERENT MASS FLOWS	76
FIGURE 4.4 STATIC PRESSURE AT DIFFERENT STATIONS AT DIFFERENT MASS FLOWS.....	78
FIGURE 4.5 STATIC PRESSURE DISTRIBUTION AT THREE MASS FLOWS	81
FIGURE 4.6 RADIAL VELOCITY DISTRIBUTION AT THREE MASS FLOWS	82
FIGURE 4.7 TANGENTIAL VELOCITY DISTRIBUTION AT THREE MASS FLOWS	83
FIGURE 4.8 DIFFUSER STALL	84
FIGURE 4.9 THE CONTOUR PLOT OF RADIAL VELOCITY	85
FIGURE 4.10 COMPRESSOR PERFORMANCE.....	87
FIGURE 4.11 EFFICIENCY OF DIFFERENT STATIONS AT DIFFERENT MASS FLOWS	88

FIGURE 4.12 PERFORMANCE COMPARISON OF THE TWO VOLUTES	89
FIGURE 4.13 EFFICIENCY COMPARISON BETWEEN LARGE VOLUTE AND THE ORIGINAL ONE	91
FIGURE 4.14 TOTAL PRESSURE COMPARISON BETWEEN LARGE VOLUTE THE ORIGINAL ONE	92
FIGURE 4.15 STATIC PRESSURE COMPARISON BETWEEN LARGE VOLUTE AND THE ORIGINAL ONE	93
FIGURE 5.1 TESTED IMPELLER	96
FIGURE 5.2 SMALL AND LARGE VOLUTES	97
FIGURE 5.3 COMPRESSOR CONFIGURATIONS	98
FIGURE 5.4 COMPRESSOR PERFORMANCE.....	103
FIGURE 5.5 COMPRESSOR EFFICIENCY	104
FIGURE 5.6 PRESSURE RECOVERY AND LOSS COEFFICIENT AT EXIT CONE.....	106
FIGURE 5.7 IMPELLER PERFORMANCE	109
FIGURE 5.8 CIRCUMFERENTIAL STATIC PRESSURE DISTRIBUTION AT PINCH POSITION	112
FIGURE 5.9 SPANWISE AND CIRCUMFERENTIAL AVERAGED AREA	112
FIGURE 5.10 STATIC PRESSURE DISTRIBUTION AT VANELESS DIFFUSER OUTLET.....	113
FIGURE 5.11 PRESSURE RECOVERY AND LOSS COEFFICIENT AT VOLUTE THROAT	115
FIGURE 5.12 PRESSURE RECOVERY AND LOSS COEFFICIENT AT TONGUE POSITION	116
FIGURE 5.13 STATIC PRESSURE DISTRIBUTION IN VOLUTES	118
FIGURE 6.1 COMPRESSOR CONFIGURATIONS.....	123
FIGURE 6.2 VOLUTE GEOMETRY AT STATION 7.....	124
FIGURE 6.3 STATIC PRESSURE AT HIGH MASS FLOW	130
FIGURE 6.4 MIDSPAN STATIC PRESSURE DISTRIBUTION AT HIGH MASS FLOW	131
FIGURE 6.5 STATIC PRESSURE AT LOW MASS FLOW	134

FIGURE 6.6 MIDSPAN STATIC PRESSURE DISTRIBUTION AT LOW MASS FLOW	135
FIGURE 6.7 CIRCUMERENTIAL STATIC PRESSURE DISTRIBUTION.....	140
FIGURE 6.8 VOLUTE FLOW PATTERNS AT LOW MASS FLOW	141
FIGURE 6.9 STATIC PRESSURE AT LOW MASS FLOW	144
FIGURE 6.10 TOTAL PRESSURE AT LOW MASS FLOW	145

Nomenclature

A	area
AR	area ratio
C _p	specific heat at constant pressure
C _v	specific heat at constant volume
c _p	pressure recovery
g	gravity acceleration
K	specific heat ratio
L	length, loss vector
M	Mach number
m	mass flow rate
p	pressure
R	gas constant
r	radius
V	velocity

Greek

α	absolute flow angle from radial or axial
β	relative flow angle from radial or axial
ϕ	flow coefficient
ψ	isentropic head coefficient
η	efficiency
λ	volute inlet swirling parameter
ω	loss coefficient, impeller rotating speed
Ω	rotation speed
ρ	density

Superscripts

0	stagnation
n	iteration
r	rotor
s	stator
-	average

Subscripts

0	stagnation, tongue
1	inlet of impeller
2	exit of impeller
3	inlet of diffuser
4	grid interface between impeller and diffuser
5	diffuser exit

7	critical surface, $\theta = 0$
8	exit flange of the compressor
e	exit
EC	exit cone
f	friction
i	inlet
isen	isentropic
mi	meridional
MVDL	meridional velocity fump loss
R	radial
T	tangential
TVDL	tangential velocity dump loss

Chapter 1

INTRODUCTION

1.1 History and applications

The gas turbine has been a major driving force in the development of compressible flow machines, both axial and radial. The multi-stage axial compressor and the centrifugal compressor are competitors for the delivery of large volume flow rates of air to the engine with very high-pressure ratio at the inception of gas turbine engine development. Because the centrifugal compressor can make use of the radius change across the impeller, it can produce a higher specific work transfer than an axial machine at the same speed and mass flow rate. So if the pressure ratios are only up to 6, a single-stage centrifugal compressor could replace a several-stages axial compressor. However, since the centrifugal compressor delivers the air unhelpfully in the radial direction and requires an exit volute, it is unattractive to build a multi-stage centrifugal compressor, at least for aircraft applications. Multi-stage centrifugal compressor is often used only when size and weight are of secondary importance comparing to capacity and pressure ratio.

In the early 40's, an enormous volume of effort was invested in the development of gas turbines. In Germany, the major efforts were based on the axial flow compressor, but in Britain, the centrifugal compressor was mainly developed. At the same time, the internal combustion engine turbocharger provided a large market for small high-speed centrifugal compressors as the centrifugal compressor had a wider margin between surge and choke than its axial counterpart. As power requirements grew and massive projects of research and development was invested into axial compressor in the World War II,

however, the axial flow compressor even had higher efficiencies than the turbines and was more suitable for large engines.

By the late 50s, people realized that smaller gas turbines would have to use centrifugal compressors, and it provided the necessary impetus for further rapid development of the centrifugal compressor. In the mid-60s, the need for advanced military helicopters powered by small gas turbine engines started the serious research and development work on centrifugal compressor again. Small turboprops, turboshafts and auxiliary power units were made in very large numbers and nearly all used centrifugal compressors. The reasons why the centrifugal compressor was preferred were not only for their suitability for handling small volume flows, but for other advantages including a short length than an equivalent axial compressor, low maintenance demand, less susceptibility to loss of performance by build-up of deposits on the blade surfaces and the ability to operate over a wider range of mass flow at a particular rotational speed.

A pressure ratio around 4:1 can readily be obtained from a single-stage compressor made of aluminium alloys. If the titanium alloys that permit much higher tip speeds would be used, the pressure ratios greater than 8:1 could be achieved in a single stage under the advanced aerodynamics design. When higher pressure ratios are required, the centrifugal compressor may be used in conjunction with an axial flow compressor, or as a two-stage centrifugal. However, as mentioned above, the latter arrangement involves rather complex ducting between stages that is only regarded as a practical proposition when the capacity and pressure ratio are of most importance.

In recent years, many significant improvements in the performance of centrifugal compressor have been made, such as many new design procedures, mixed-flow design,

back swept vanes, and especially the computer aided design and analysis techniques. All of these improvements make the centrifugal compressors not only used in the fields mentioned above, but also employed in refrigerating plants, ventilation and in the process industries.

1.2 Centrifugal Compressor Components

A single stage centrifugal compressor or pump consists essentially of a rotating impeller, a non-rotating diffuser and a stationary volute. Figure 1.1 shows the various elements of a single stage centrifugal compressor. Before the eye of impeller, sometimes inlet guide vanes are used to guide the inlet fluid flow. Because of the whirling of the impeller, the angular momentum of the fluid is increased which means both the static pressure and the velocity are increased within the impeller. The diffuser is used to convert the kinetic energy available at the impeller exit into static pressure by decelerating the fluid. Vaneless and front-pinch diffuser is shown in Figure 1.1. A volute that is used for collecting the fluid from the periphery of the diffuser and delivering the fluid to the outlet pipe follows diffuser. Usually the part between station 7 and 8 has a specific name — exit cone. The exit cone is essentially a divergent device where the fluid in it is further diffused. In this dissertation, the exit cone is referred as one part of volute.

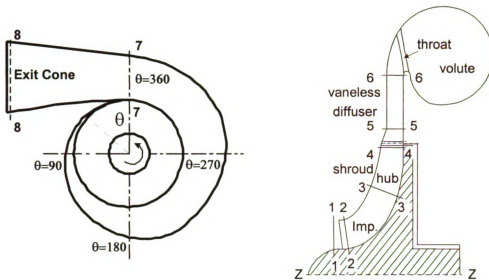


Figure 1.1 A single stage centrifugal compressor

1.3 The purpose of volute study

The volute surrounds the impeller, and it is well known that the fluid particles leaving the impeller have logarithmic spiral shape. So the complicated swirling motion inside three-dimensional volutes makes the design of the volute, matching with the design mass flow of the impeller, very difficult. In one word, volute studies are important for three reasons:

The first one is that the performance of the centrifugal compressor strongly depends on the match of the impeller, diffuser and volute. The overall performance can be completely different from any component performance, especially the impeller performance.

Secondly, a circumferential constant pressure distribution downstream the impeller is essential to realize a uniform energy transfer in the impeller, which is a condition for a high impeller efficiency, because non axisymmetric pressure distributions

downstream the impeller cause flow unsteadiness and additional losses in the impeller.

So, even the impeller performance is also affected by the volute part.

Thirdly, for the same reason as above, volute can cause a circumferential pressure distortion at off-design operation, resulting in an unsteady impeller flow and additional radial forces on the shaft. It can significantly increase the bearings loading.

The fourth reason is that volute can influence the operating range of the compressor by a shift of the surge line and rotating stall limit to higher mass flow. The operating range of the compressor becomes wider with the circumferentially more uniform static pressure distribution.

Thus, we can say that compactness, efficiency and the absence of circumferential pressure distortion are the main design targets for compressor volutes.

1.4 Objectives of the current study

So far, many CFD companies have developed various commercial software packages for impeller grid generation, such as Bladegen and TASCGen. However, no commercial software is generated specifically for the volute grid generation. So, developing a volute grid generation tool to facilitate the volute analysis is the first goal of this study.

The second target is to use the volute grid to match different diffuser and impeller grids and in-depth study the aerodynamic performance and interaction of the impeller, diffuser and volute. It should be very helpful on the understanding of the flow structure in the three components. The investigation of the effects of the different volute geometrical parameters on the volute flow field was paid more attention.

Experiments were done in test facilities at the company that give us this project. The experimental results are used in the verification of the simulation method. The final purpose is to investigate the design and optimization method for volute.

This dissertation starts with a literature survey on the volute research to appreciate the progress in this field. The main body begins from volute flow model, and then goes through loss mechanisms inside volute, volute/impeller interaction, ends at the radial force on the shaft because of the non-uniform pressure distribution circumferentially.

Chapter 3 focuses on the theory that would be used in the current study and the integrated tool development. The theory, the first part of this chapter, would be verified in the following chapters. The introduction for the integrated tool, the second part of this chapter, is to clear the need for this kind of tool, the difficulty to make the tool and the basic way to use this tool.

Chapter 4 describes an assessment of the theory background and the integrated tool introduced in chapter 3. Theoretical and numerical analysis is employed to investigate the performance and basic flow structures in the volutes and diffusers of two different compressors. The numerical analysis is compared with experimental data. The basic flow structure in diffuser and volute shown in the literature survey has been validated in the circular overhung volutes.

Chapter 5 presents the experimental and numerical investigation on the performance of the two different overhung volutes with flat-top circular cross sectional area to the same centrifugal compressor impeller. Attention is paid on the agreement between CFD results and test data, the two CFD models comparison and the effect of the two volutes on the whole compressors. It was found that the “stage rotor” model is not so

accurate only on the prediction of the impeller performance. On the whole machine performance, its prediction is not worse than “frozen rotor” although it cannot give the difference exists in the two configurations at high mass flow.

Chapter 6 presents the investigation of the detailed flow structure in the impellers and volutes. The effects of the tongue position of volute, the static/total pressure distributions, and velocity distributions in the two volutes are the main research interest. It reveals that the second flow strongly depends on the volute channel curvature and the leak flow around the tongue. This phenomenon can occur either at low mass flow or at high mass flow, or either downstream of the tongue or upstream of the tongue.

Chapter 2

Literature Survey

2.1 Introduction

The volutes—the last component of a centrifugal compressor—just captured the turbomachinery researcher’s attention recently since it has been proved that a good design of volute can improve the compressor performance greatly. The reason why the volute was neglected relative to the impeller and diffuser was primarily due to the complex volute geometry, the strong interaction of volute with other components and the high total cost of analysis that includes the geometry set up time, the volute grid generation time, the analysis time, etc.

After more and more researches focused on the volute part recently, there are quite a few publications for the volute part appeared in the past 20 years although they are still small in quantities compared to the large number of papers about the other components of the radial machines. So far, a popular way that is put forward by Erkan Ayder divided the volute study into three groups. The first group investigates the basic flow model in the volute and gives an insight into the sources of losses by providing detailed information about the volute flow field. The second one deals with the influence of global volute geometrical parameters on the overall characteristics of compressor. Its main purpose is to predict the performance of volute. The third group is oriented towards mechanical problems and investigates the radial force on the impeller shaft caused by the volute. Actually, all of these three groups can be divided into two big groups. One group

focuses only on the volute study. Another one is concentrated on the interaction between volute and other compressor components.

Basically, all the literature available would be presented in this chapter according to the two big groups as follows.

2.2 Volute Alone Study

2.2.1 Flow model in volute

R. A. Van Den Braembussche, et al (1990) did the measurements of the three-dimensional flow in a simplified model of a centrifugal compressor overhung volute at design and off-design operations. The figure 2.1 below is the straight volute model in Braembussch's experiment. Since the curvature radius of volute tongue and outlet are normally much larger than the volute cross section radius, their influences on the flow is not importance. This is the theoretical base for the straight volute model.

Escudier, et al. (1980) indicate that in the vortex tube the fluid enters at the constant outer radius firstly, then move from the outer radius to the center. It results in an increase of the radial velocity due to the conservation of momentum. The vortex tubes, therefore, have a free vortex circulation near the walls and a forced vortex circulation in the center. But, in Braembussche's experiment, the flow in volute is completely different from this theory. The fluid entering close to tongue at small radius fills the center of the volute. New fluid enters further downstream at large radius and starts rotating around the upstream fluid. Vortex tubes of increasing radius are wrapped around each other, shown in figure 2.2. And, each part of the fluid remains at constant radius.

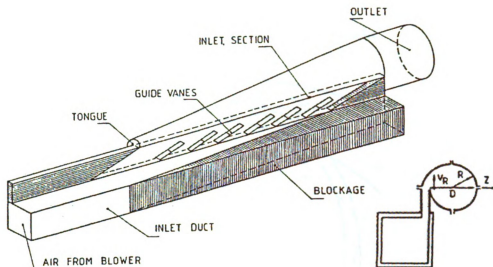


Figure 2.1 Straight volute model in Van den Braembussche experiment (1990)

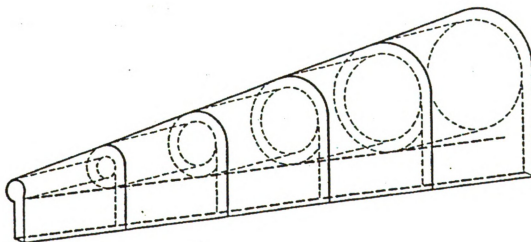


Figure 2.2 Superposition of vortex tubes in a volute (1990)

This flow model was also proved by E. Ayder (1994). Figure 2.3 is the calculated results at medium mass flow. We can see the fluid entering the volute at a position close to the tongue (A) remains in the center of the volute until the compressor exit. Fluid

entering the volute farther downstream (B, C, D) wraps around the previous one, which confirms the volute flow model suggested by Van den Braembussche.

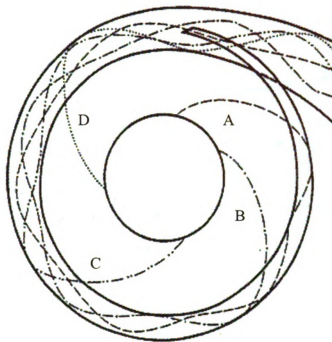
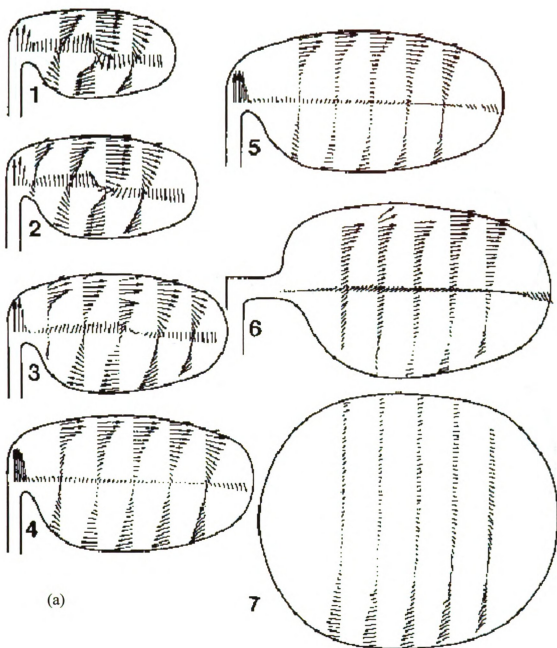
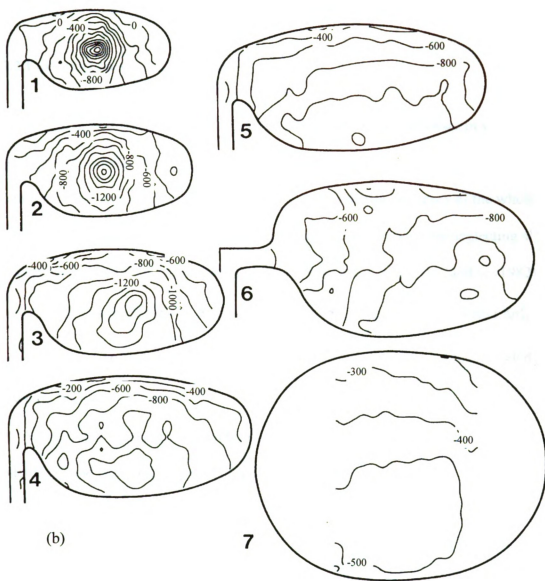


Figure 2.3 Particle tracing inside the vaneless diffuser and volute (1994)

Also, Ayder (1993) got the experimental data in a centrifugal compressor volute with elliptical cross section. Figure 2.4 provides a clear picture of the three-dimensional swirling flow inside an elliptical volute at different circumferential positions. It also can be a proof of the flow model in Van den Braembussche paper. Besides the swirl velocity distribution, this paper also showed the total pressure distribution. Firstly, the reason for this kind of total pressure distribution was explained either from internal friction or from a particular radial velocity distribution at the volute inlet. Finally, the detailed flow measurements have been used to give the mechanism for the reason, which is the high losses and low total pressure in the center of the cross sections.





**Figure 2.4 Swirl velocity (a) and total pressure (b) distribution
at medium mass flow**

2.2.2 Loss mechanisms inside volute

Although different configurations have different losses, the losses in volutes, especially at off-design conditions, can be significantly high. A good understanding of the loss mechanisms in volute can help improve the prediction accuracy of the whole centrifugal compressor although this kind of model was put forward by neglecting all the other component influences. The overall volute losses are modeled by Japikse (1982), Weber and Koronowski (1986). Normally, Meridional Velocity Dump Losses (Δp_{MVDL}^o), Friction Losses (Δp_f^o) and Tangential Velocity Dump Losses (Δp_{TVDL}^o) are included in the volute losses.

Usually, it is assumed the meridional velocity is lost totally, the friction losses are modeled as pipe flow and only part of the tangential velocity can be lost. All of these three kind of losses are expressed by following equations,

$$\Delta p_{MVDL}^o = \frac{1}{2} \rho V_{mi}^2 \quad (2.1)$$

$$\Delta p_f^o = \omega_f \frac{L}{D_{hyd}} \frac{1}{2} \rho V_t^2 \quad (2.2)$$

$$\Delta p_{TVDL}^o = \omega_t \rho \frac{1}{2} (V_{ti} - V_{te})^2 \quad (2.3)$$

where $\omega_t = 1$.

The meridional velocity is the meridional velocity at the volute inlet, which is assumed to be lost and it is called meridional velocity dump losses. The amount of losses is expressed by the equation (2.1).

The friction losses are calculated in function of the roughness of the wall, the hydraulic diameter of the volute channel (D_{hyd}), the path length of the fluid particles (L) within the volute (which is assumed to be equal to the length of the volute channel) and the through flow velocity (V_t) inside the volute. Only the through flow velocity is considered for the friction losses since complete dissipation of the meridional velocity is already accounted for in the meridional velocity dump losses. The friction coefficient depends on the Reynolds number and relative surface roughness and can be obtained from the standard friction charts for pipes (equation 2.2).

In order to calculate the tangential velocity dump losses, two assumptions are made. Firstly if the tangential velocity accelerates from the volute inlet to the volute outlet ($V_{ti} < V_{te}$), then it is assumed that no tangential velocity dump loss occurs. However if the tangential velocity decreases from the volute inlet to the exit ($V_{ti} > V_{te}$), then the flow diffuses and it is assumed that the total pressure loss is equivalent to the total pressure losses in a sudden expansion mixing process. See equation (2.3)

This theory has been used by Japikse (1982) to calculate the performance of a volute, specified by means of the volute loss coefficient (ω) and static pressure recovery coefficient C_p .

$$C_p = \frac{p_e - p_i}{p_i^0 - p_i} \quad (2.4)$$

in function of the ratio of volute outlet area to volute inlet area

$$AR = A_e / A_i = \pi D_e^2 / 8 \pi r_i b_i \quad (2.5)$$

and the volute inlet swirling parameter

$$\lambda = V_{ti} / V_{ri} \quad (2.6)$$

Flow is treated as incompressible and the friction losses are neglected. The following simple relations have been obtained in the case of accelerating tangential velocity from volute inlet to outlet ($V_{ti} < V_{te}$).

$$\text{For the loss coefficient } \omega = \frac{1}{1 + \lambda^2} \quad (2.7)$$

$$\text{and the static pressure recovery coefficient } C_p = \frac{\lambda^2 - 1/AR^2}{1 + \lambda^2} \quad (2.8)$$

In case of decelerating through flow ($V_{ti} > V_{te}$)

$$\text{velocity from volute inlet to outlet } \xi = \frac{1}{1 + \lambda^2} + \frac{(\lambda - 1/AR)^2}{1 + \lambda^2} \quad (2.9)$$

$$\text{and the static pressure recovery coefficient } C_p = \frac{2(\lambda - 1/AR)}{AR(1 + \lambda^2)} \quad (2.10)$$

The calculated and measured variations of C_p and ω with volute inlet swirl parameter λ and the volute outlet to inlet area ratio AR are compared in figure 2.5 and 2.6. Measured and calculated static pressure rise coefficients agree well and it seems that this model provides a useful basis for the prediction of volute static pressure rise but not for the losses. The difference between the calculated and measured values of loss coefficient for high mass flows (small λ) can be due to neglecting the remaining swirl at the exit of the volute in the model but not in the measurements. The assumptions of uniform inlet and outlet flow conditions may not be satisfied.

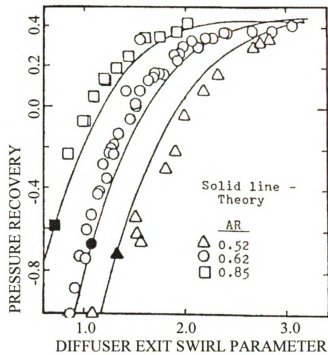


Figure 2.5 Volute pressure recovery coefficient comparison of theory and data (after Japikse, 1982)

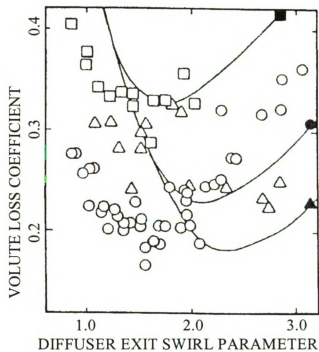


Figure 2.6 Volute pressure loss coefficient comparison of theory and data (after Japikse, 1982)

The experimental and theoretical investigations of Weber and Koronowski (1986) reveal that the modeling of the tangential velocity dump losses without taking into account the variation of the central radius of the volute channel causes an incorrect prediction of the losses especially for the internal type of volutes ($R_{volute} < R_i$). Therefore they have modified the modeling of tangential velocity dump losses.

They introduce an intermediate station in the volute channel at the 50% collection point (where 50% of mass flow is collected by the volute). The through flow velocity at this intermediate station (f) and at the volute exit (e) are calculated from the conservation of mass, assuming an uniform velocity over the cross section,

$$V_{Tf} = Q / (2A_f) \quad (2.11)$$

$$V_{Te} = Q / A_e \quad (2.12)$$

The effective theoretical velocity at the volute inlet can be calculated from the conservation of angular momentum between volute inlet (i) and the intermediate station (f).

$$V_{Ti-f} = V_{Tf} r_f / r_i \quad (2.13)$$

The second value of the through flow velocity at the inlet of the volute can be calculated from the through flow velocity at the exit of the volute and the conservation of angular momentum between the volute inlet and exit.

$$V_{Ti-e} = V_{Te} r_e / r_i \quad (2.14)$$

In the new model, the tangential velocity dump losses consist of two components: If the measured tangential velocity at the volute inlet (V_{Ti}) is larger than V_{Ti-f} then the

flow is accelerating in the first part of the volute and the first component is obtained by the following relation

$$\Delta P^0_{TVDLf} = \omega_T \rho (V_{Ti}^2 - V_{Ti-f}^2) / 2 \quad (2.15)$$

where $\omega_T = 0.5$ for volutes and 1.0 for plenum.

If V_{Ti} is smaller than V_{ti-f} , first component of losses is calculated by

$$\Delta P^0_{TVDLf} = \frac{\rho (V_{Ti} - V_{ti-f})^2}{2} \quad (2.16)$$

In case of measured value V_{Ti} is larger than V_{Ti-3} , means flow is accelerating and the second component of the tangential velocity dump losses is given by

$$\Delta P^0_{TVDL_e} = \omega_T \rho (V_{Ti}^2 - V_{Te}^2) / 2 \quad (2.17)$$

and otherwise

$$\Delta P^0_{TVDL_e} = \frac{\rho (V_{Ti} - V_{te})^2}{2} \quad (2.18)$$

The total tangential velocity dump losses is given by

$$\Delta P^0_{TVDL} = \Delta P^0_{TVDLf} + \Delta P^0_{TVDL_e} \quad (2.19)$$

Adding the exit cone losses to the volute losses provides a complete prediction model for the losses between volute inlet and compressor outlet. The exit cone losses are treated as gradual expansion and expressed by

$$\Delta P^0_{EC} = \omega_{EC} \rho \frac{(V_{ECi} - V_{ECe})^2}{2} \quad (2.20)$$

ω_{EC} depends on the total opening angle of the cone and varies from 0.15 for an opening angle of 10 degree to a value of the order 1 for an opening angle 60 degree. Since the opening angle of a well designed volute exit cone does not exceed 10 degree, a

constant value of 0.15 is proposed by Weber and Koronowski (1986). The equation description above mostly is referenced therein from Ekan Ayder (1993).

Based on the observations of Ayder (1994), it has been decided to solve the problem by adding second-order dissipation and wall shear forces to an Euler solver, rather than resorting to a more expensive and time-consuming solution of the Navier-Stokes equations. The experimental results of Ayder have shown that the flow in volutes is affected more by the losses in the core than by the wall boundary layer. Increased turbulent mixing on the concave walls (Johnston, 1970) limits the growth of the boundary layers, which are absorbed in any case by the core flow after each rotation. Boundary layer blockage can therefore be neglected, and its influence may be limited to the shear forces on the walls. The internal friction is approximated by a viscous term. The additional momentum caused by wall friction is included by adding a term $L_{i,j,k}$ to the momentum equations.

$$\Omega_{i,j,k} \left(\frac{d}{dt} W_{i,j,k} \right) + Q_{i,j,k} - D_{i,j,k} - L_{i,j,k} = 0 \quad (2.21)$$

and the wall shear stress can be defined by the following relation:

$$\tau_{wall} = C_f \frac{1}{2} \rho V^2 \quad (2.22)$$

resulting in the following components on each element of the wall:

$$\tau_x = -\frac{u}{V} \tau_{wall}, \tau_y = -\frac{v}{V} \tau_{wall}, \tau_z = -\frac{w}{V} \tau_{wall} \quad (2.23)$$

and, the energy dissipation due to wall friction

$$- \tau V (S_x + S_y + S_z) \quad (2.24)$$

must be added to the loss vector L.

$$L = \begin{pmatrix} 0 \\ \tau_x(S_x + S_y + S_z) \\ \tau_y(S_x + S_y + S_z) \\ \tau_z(S_x + S_y + S_z) \\ \tau V(S_x + S_y + S_z) \end{pmatrix} \quad (2.25)$$

As the loss vector is calculated only on the solid wall surfaces, it influences only the vertices of the volumes adjacent to the solid walls and creates a local velocity gradient perpendicular to the wall.

Viscous energy dissipation, at all regions of nonzero velocity gradient (at the wall and at the vortex center), is achieved by second-order dissipation

$$k2(W_{i-1,j,k} + W_{i+1,j,k} + W_{i,j-1,k} + W_{i,j+1,k} + W_{i,j,k-1} + W_{i,j,k+1} - 6W_{i,j,k}) \quad (2.26)$$

The coefficient $k2$ is adjusted empirically to simulate the viscous terms in the Navier-Stokes equations. Actual calculations are done with a $k2$ value of 0.002.

The calculations underestimate the concentration of low total pressure at the center of the first cross section. And the calculated magnitude of the total pressure and static pressure over some sections are different from the measured ones for high mass flow. The author admits the reason for this phenomenon is unknown.

The flow field measurements were carried out by Hagelstein, et al (2000) at the diffuser exit and at several peripheral positions in the volute and in the exit pipe diffuser, respectively. And, Hagelstein also use the same methods to simulate the flow in volute. The results are compared with those obtained using the calculation method of Ayder (1993). Again, they have the same problem. But, the author think the result should be satisfying if one considers the complexity of the flow and the small computation time.

In Gu, et al. (2001) study, they suggest that for the design and high mass flow rates, the friction loss due to the through flow accounts for more than half of the volute losses. It implies that the assumption in Young and Japikse's model is too pessimistic; at least half of the inflow Meridional kinetic energy is preserved. For the low mass flow, the friction loss only takes a small part of the total loss; it indicates that there should be some other loss mechanisms. The obvious one is the diffusion loss, which is not considered in the friction model. For the low mass flow, the equivalent diffuser ratio is 1.228. The flow structure in the volute will be investigated by attempting to find out some loss mechanisms.

One point of this paper is to show that the inlet meridional velocity component will not totally lose; it creates the swirling flow in the volute. And at high mass flow, the production and diffusion of the counter clock-wise vortex are believed to be an additional source that increases the volute loss.

2.3 The interaction between volute and other components

2.3.1 Influence of volute geometrical parameters on compressor performance

There are quite a few key volute geometrical parameters commonly are recognized in the parametrical studies in the available literature. Generally, the following geometrical parameters are more important as Ayder's suggested in 1993:

- Circumferential variations of the cross sectional areas
- Shapes of the cross sections
- Radial position of the cross section

- Positions of the volute inlet (Tangential or Central)
- Tongue geometry

What follows will try to evaluate the actual knowledge about each of these parameters as it appears from the literature.

2.3.1.1 CIRCUMFERENTIAL VARIATION OF THE CROSS SECTIONAL AREA

Stiefel (1972) has studied the performances of two compressors with different volutes but with the same impellers and vaneless diffusers (fig. 2.12). Figure 2.12a shows the volute that the pressure ratio is 3.8. Figure 2.12b presented a 30% smaller volute performance and the pressure ratio is 6. The author explained that the wavy curves at high pressure ratio in figure 2.12a results from an unsteady state. The reason for this unsteady flow is the flow separation. The smaller volute exhibits a wider operation range after comparison of figures 2.12a and 2.12b. And, Stiefel also pointed out that generally the best compressor efficiency is achieved when the volute cross sectional area is 10-15% smaller than the area calculated according to the frictionless flow.

The comparison study of the volutes with constant and circumferential-increasing cross section area has been done by Lopez Pena (1987). All the four different volutes in this research (figure 2.7) belong to the turbocharger compressor field and can be divided into two types. The first type is the standard volute of a turbocharger compressor. It has a cross section of elliptical shape and a circumferentially increasing area. The other three volutes can be included in another type, i.e., they have a rectangular cross sectional shape and a circumferentially constant area distribution. The differences among these three volutes only lie in the cross section area. According to the area, the three volutes were

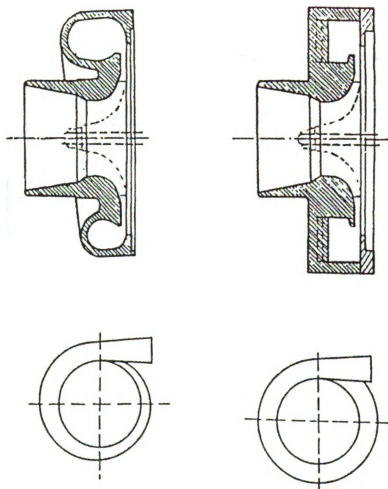
referenced as minimum, medium and maximum volutes respectively. The static pressure distributions at the impeller exit, the diffuser exit and on the volute wall have been measured for all the investigated volutes.

The results of the first type volute and the minimum volute, which is 23% smaller than the exit area of the first type volute, have been shown in figure 2.8a. In order to compare the whole machine performance, four different rotation speeds have been tested. We can see the surge line of the first type volute, or say the standard volute, is at a higher mass flow than the surge line of the minimum volute. Figure 2.9 shows the static pressure distributions at minimum, medium and maximum flows. It can be seen the static pressure at minimum mass flow increases along the azimuth angle. This circumferential pressure distortion propagated through the diffuser back to the impeller exit. It will cause unsteady flow, initiate surge and hurt impeller efficiency. According to the author, the minimum volute has a larger part of flow separation. This is the reason why the minimum volute causes a lower pressure ratio and efficiency than the standard volute. Medium mass flow is near design point. This is not the research interest. At maximum mass flow, the static pressure decreases after 130 degrees or so. This means the air will accelerate until the end of the volute. Before this angle, a constant pressure region can be found that indicates a separation zone.

The results of the first type volute and the medium volute, which is 3% smaller than the exit area of the first type volute, have been shown in figure 2.10. From figure 2.10a, the operating range of the medium volute is a little bit wider than the operating range of the standard volute. Figure 2.10b, the curves at minimum mass flow is flatter

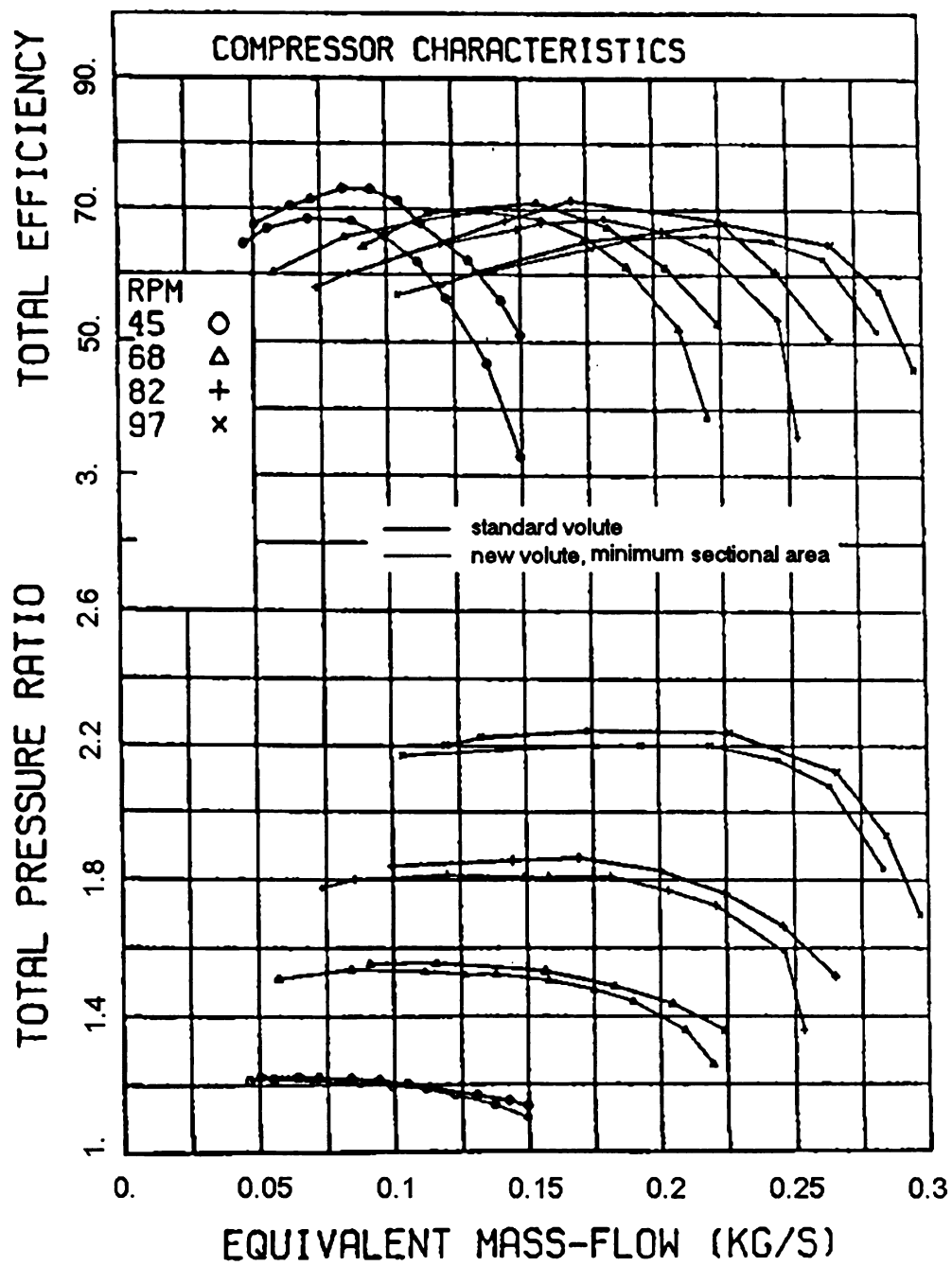
than the curves of the minimum volute. At maximum mass flow, the circumferential static pressure distribution is more uniform than the distributions in figure 2.9.

Figure 2.11 shows the performance of the standard volute and the maximum volute, which is 17% larger than the exit area of the standard volute. The efficiency drops and pressure recovery losses become bigger from medium mass flow to maximum mass flow. The author was also uncertain about this phenomenon.



(a) Increasing cross sectional area (b) Constant cross sectional area

Figure 2.7 Types of volutes



(a) Compressor performance

Figure 2.8 Performance with minimum area (after Lopez Pena, 1987)

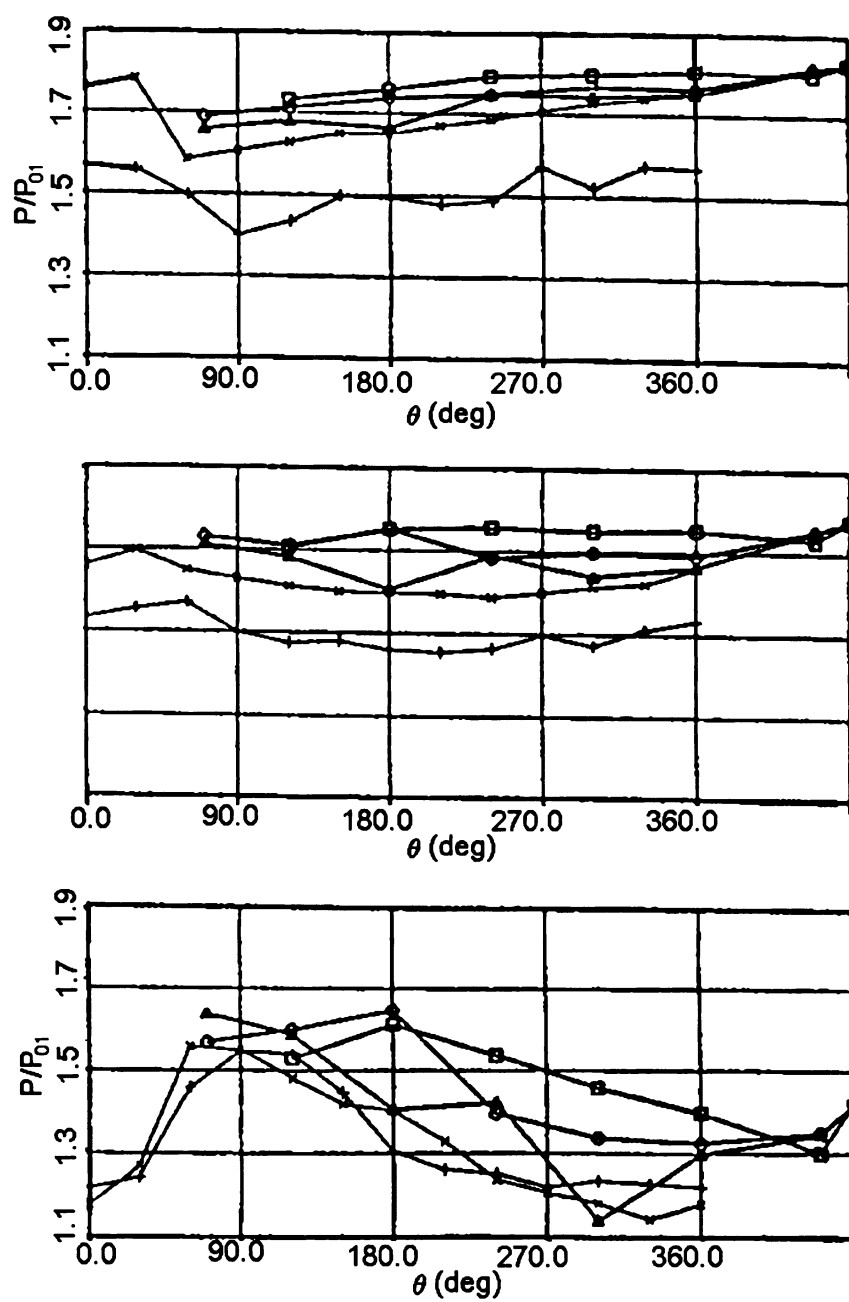
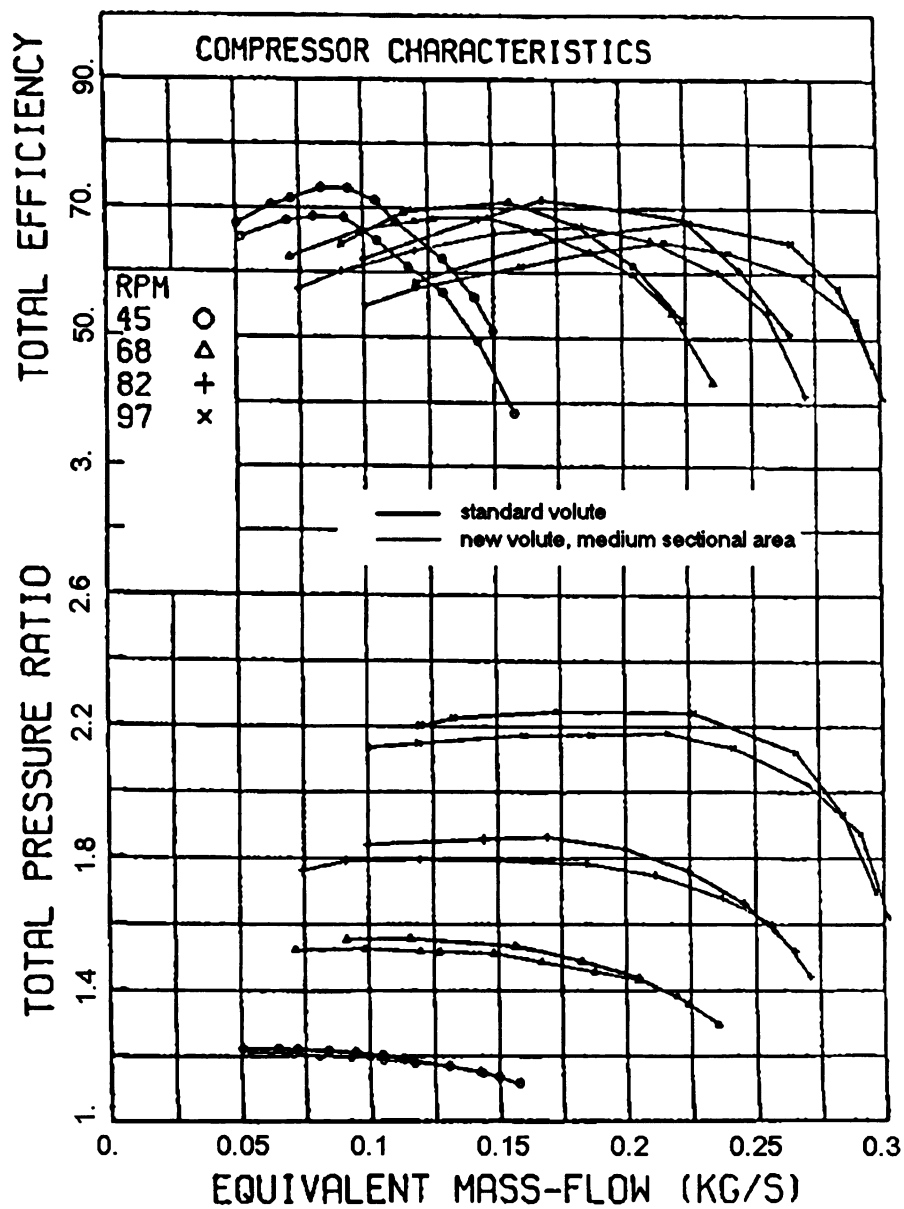
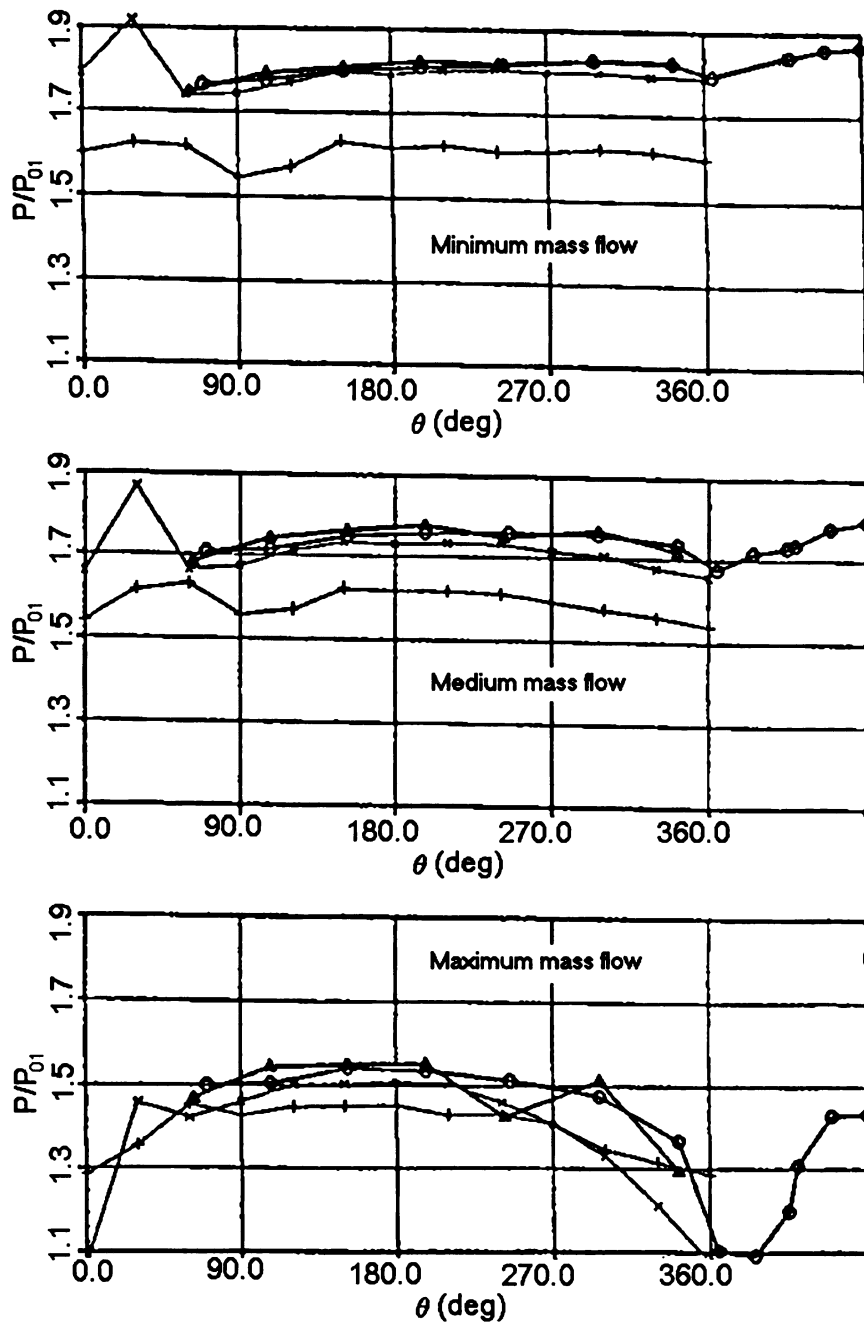


Figure 2.9 Static pressure distribution along the volute and diffuser of the standard compressor

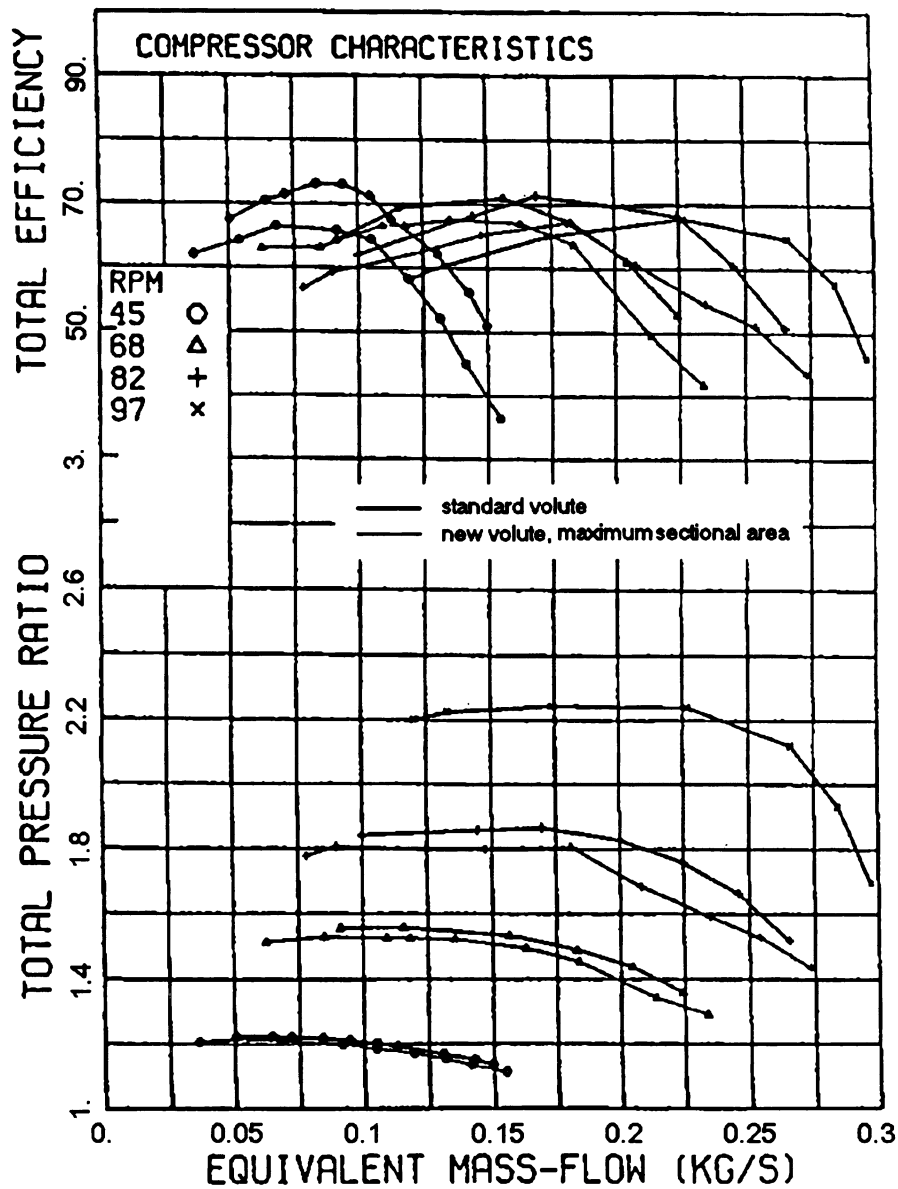


(a) Compressor performance

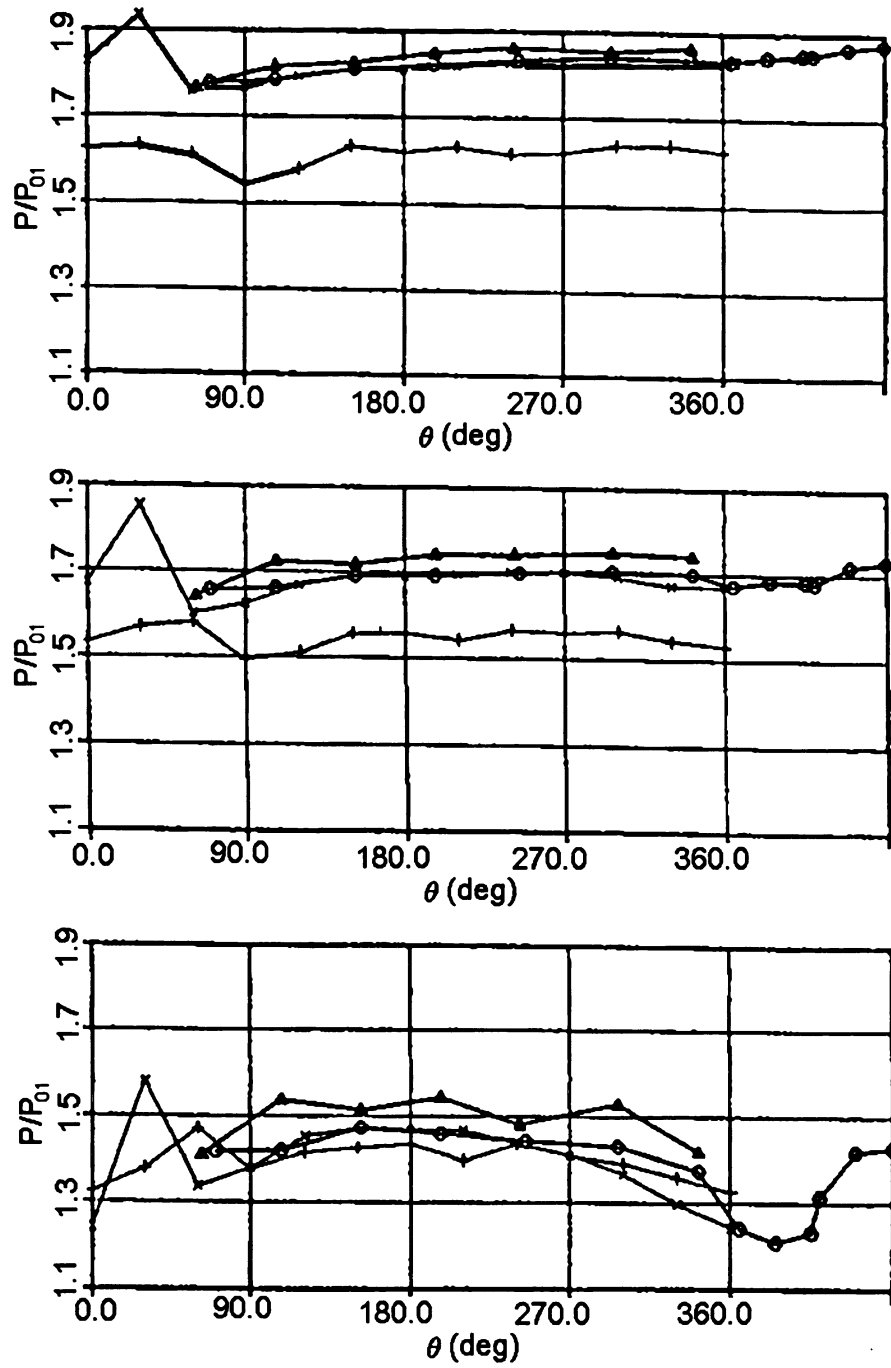


(b) Static pressure along volute and diffuser

Figure 2.10 Performance with medium area

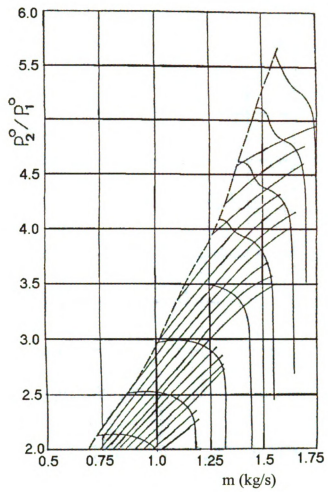


(a) Compressor performance

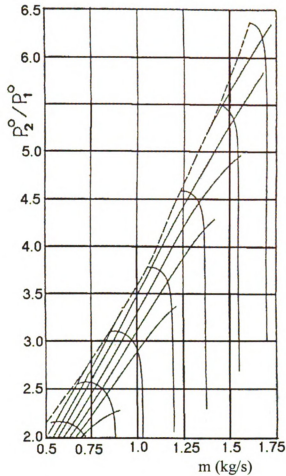


(b) Static pressure along volute and diffuser

Figure 2.11 Performance with maximum area



(a) Design pressure ratio 3.8



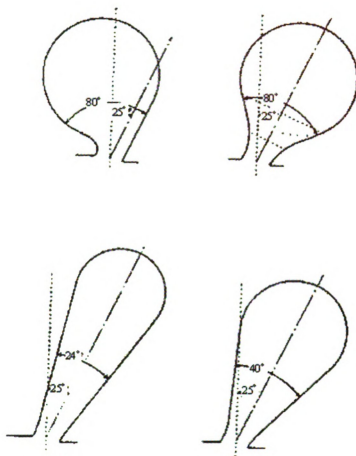
(b) Design pressure ratio 6

Figure 2.12 Compressor performance map

2.3.1.2 SHAPE OF THE CROSS SECTION

The effects of the chosen cross sectional shapes on the performance of the compressor have been studied by Brown and Bradshaw (1947). The four volutes having different cross sectional shapes and same circumferential variation of the cross sectional area are shown in figure 2.13. The total pressure and adiabatic efficiency of the compressor with different volutes are shown in figure 2.14. The x-axis is the corrected

load coefficient. The author concluded that the shape influence on the compressor performance could be neglected in the four volute configurations.



- (a) 80° asymmetrical (b) 80° symmetrical
(c) 24° symmetrical (d) 40° symmetrical

Figure 2.13 Cross sections of volutes

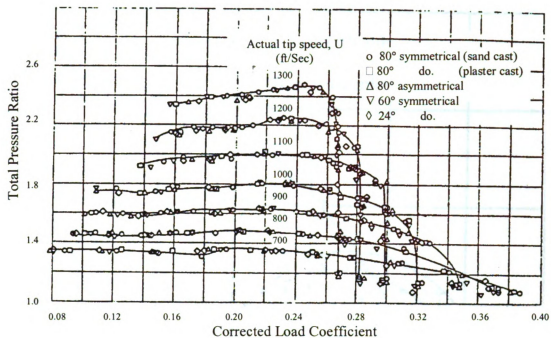


Figure 2.14 Total pressure ratio of compressor with different volutes at actual tip speeds of 700 to 1300 feet per second

Hubl studied the influence of the symmetric and asymmetric volute inlet on a pump performance in 1975. The results are shown in figure 2.15. Both the volutes have the same circumferential variation of the cross sectional area. For a symmetric volute, the efficiency of the symmetric volute is smaller than the efficiency of the asymmetric volute when the x coordinate is higher than 0.65. And, the maximum efficiency occurs at a smaller mass flow than the one of an asymmetric volute. When the mass flow goes higher further from the maximum efficiency point, the asymmetric volute efficiency becomes better and better. The interesting thing is that the symmetric volute exhibits a higher head at low mass flow because more energy is added to the fluid by the impeller.

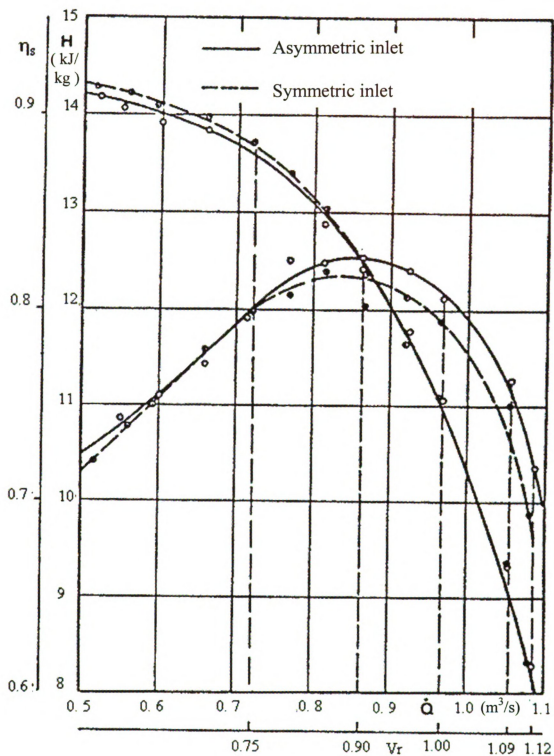


Figure 2.15 Global pump characteristics with symmetric and asymmetric volute

Lendorff and Meienberg (1944/1945) investigated the two symmetric volutes and one overhung volute (figure 2.16). The data of this figure show a preference for the overhung volute. Similar experimental results were reported by Mishina and Gyobu (1978). Figure 2.17 shows that the losses in an asymmetric volute appear to be reasonably insensitive to the flow angle; the losses of a volute with a circular cross section are lower than those of a square or a rectangular cross section; a small centroid diameter appears to deteriorate the volute performance significantly. Performance of a collector with a square cross section was also found to have high losses. All the description in this paragraph was referenced therein from Japikse's book (1996).

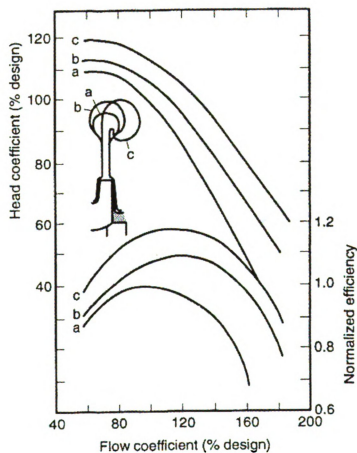


Figure 2.16 Comparison of performance for different volute geometries

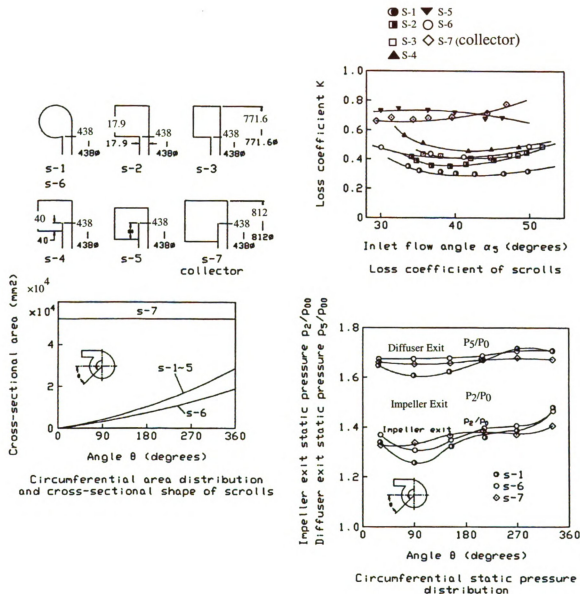


Figure 2.17 Effect of cross-sectional shapes on scroll performance

2.3.1.3 Radial Position of the Cross Section

According to the radial positions of their cross-sectional area, volutes can be subdivided into two groups, i.e. the external volute and the internal volute. If the radii of all the cross-sections of a volute are larger than the radius of the diffuser outlet, this kind of volute will be referenced as an external volute. Contrary to this definition, an internal volute is the radii of the cross-sections of a volute smaller than the radius of the diffuser outlet. This is only a coarse rule to distinguish all the volutes in the world. For example, a volute can have a constant radius of outer (or say, inner) wall, which might be either an external or internal volute because it can be an external volute at some cross-sections and an internal volute at other cross-sections. The radial position variation of volutes depends on their applications. Actually, it is limited by the available installation spaces and the cost considerations.

Mishina and Gyobu studied quite a few volutes in 1978. Their results have been shown in figure 2.17, where s-1 is a circular volute while all the other volutes are rectangular ones. The circumferential variations of the sectional areas are also shown in this figure. We can see these curves are almost constant along the periphery. The s-2, s-4 and s-5 volutes are located at a decreasing radius. The authors pointed out that the internal type volute (s-5) and the collector (s-7) have a very high loss coefficient for all operating points. By moving the volute channel to a larger radius (s-4), the loss coefficient of the volute can be decreased by 30%. Since the angular momentum is conserved (equation 2.27), we can expect a better volute performance. Actually, the authors of this paper have done that by giving the s-2 example.

$$V_{Ti}R_i = V_T R \quad (2.27)$$

Stiefel's results (1972) also confirmed this theory. In his case, compressor efficiency with the volute located at the larger radius is better than the one located at smaller radius from low mass flow to high mass flow.

2.3.1.4 Tongue Geometry

Almost all the literatures about the tongue geometry are about pump. Lipski (1979) has concluded that the increasing radial distance between the impeller and the tongue by shortening the tongue but keeping the setting angle constant results in more flat characteristics. Short tongues cause higher efficiencies and total head for all mass flows.

It has been observed that for mass flows smaller than the optimum mass flow the tongue is pulled towards the impeller. The force acting on the tongue changes direction near the best efficiency point and tongue is pushed away from the impeller for mass flows higher than optimum one.

Keep in mind that all of these conclusions are based on pump study, not on centrifugal compressor.

2.3.1.5 Radial Forces

The nonuniform static pressure distribution in a volute can propagate back to the circumference of the impeller outlet. Thus, the radial force on the impeller shaft could be created. So far, many researches focus on the source of the circumferential static pressure variation.

Agostinelli, et al (1960) measured the radial forces. Different ratios of collector width to impeller width and the ratios of collector outer wall diameter to impeller exit diameter were taken into account. From his results, it shows that there is some combinations exist to provide an effective means for minimizing the unbalanced radial fore on the impeller shaft.

Lorett and Gopalakrishnan (1986) pointed out that the difference in momentum of the flows entering and leaving the volute element must cause a change (if the two is not equal to each other) in the static pressure within the length of the volute element. And, when the static pressure is lower at the impeller periphery, the outflow radial velocity from the impeller is higher, vice versa. Thus, the maximum radial force should be at the lowest static pressure zone and in the direction from low pressure to high static pressure. Of course, this qualitative conception should be taken into account the static pressure forces.

Sideris (1988) shows that the continuity equation gives an uniform circumferential distribution along the periphery of the impeller outlet regardless of the mass flow at some volute sections. His volute's cross section area is linearly increasing. The radial velocity at the volute inlet is also constant. However, this is never observed in experiment.

Fatsis, et al. (1997) conducted a numerical investigation of the centrifugal impeller response to downstream static pressure distortions imposed by volutes at off-design operations. The calculation of the radial force adopts two different methods. The first one is the integration of pressure on the blade and hub surfaces of an impeller with a coarse grid. The second one, for a fine grid, uses a control volume for the moment of

momentum to take into account of the momentum in and out of the control volume. According to the authors, the two methods give the same radial load. It is also found the circumferentially nonuniform outlet static pressure distribution results the largest distribution of the radial force for a backswept impeller. The force is in the opposite direction of the outlet radial momentum although it is much smaller. For the radial-ending impeller, the total force is much smaller than the total force of the backswept impeller. The authors explained this phenomenon from the tangential variation of momentum since it can cause the large variation of static pressure.

Flathers and Bache (1999) claimed that a viscous code is the first time to be used in a whole compressor with all the impeller passages and the volute. Their investigation predicted magnitude and direction of the radial force are in agreement with the experimental investigation. However, significant errors existed between the CFD results and the experimental data at low mass flow.

2.4 The velocity and pressure distribution in volute

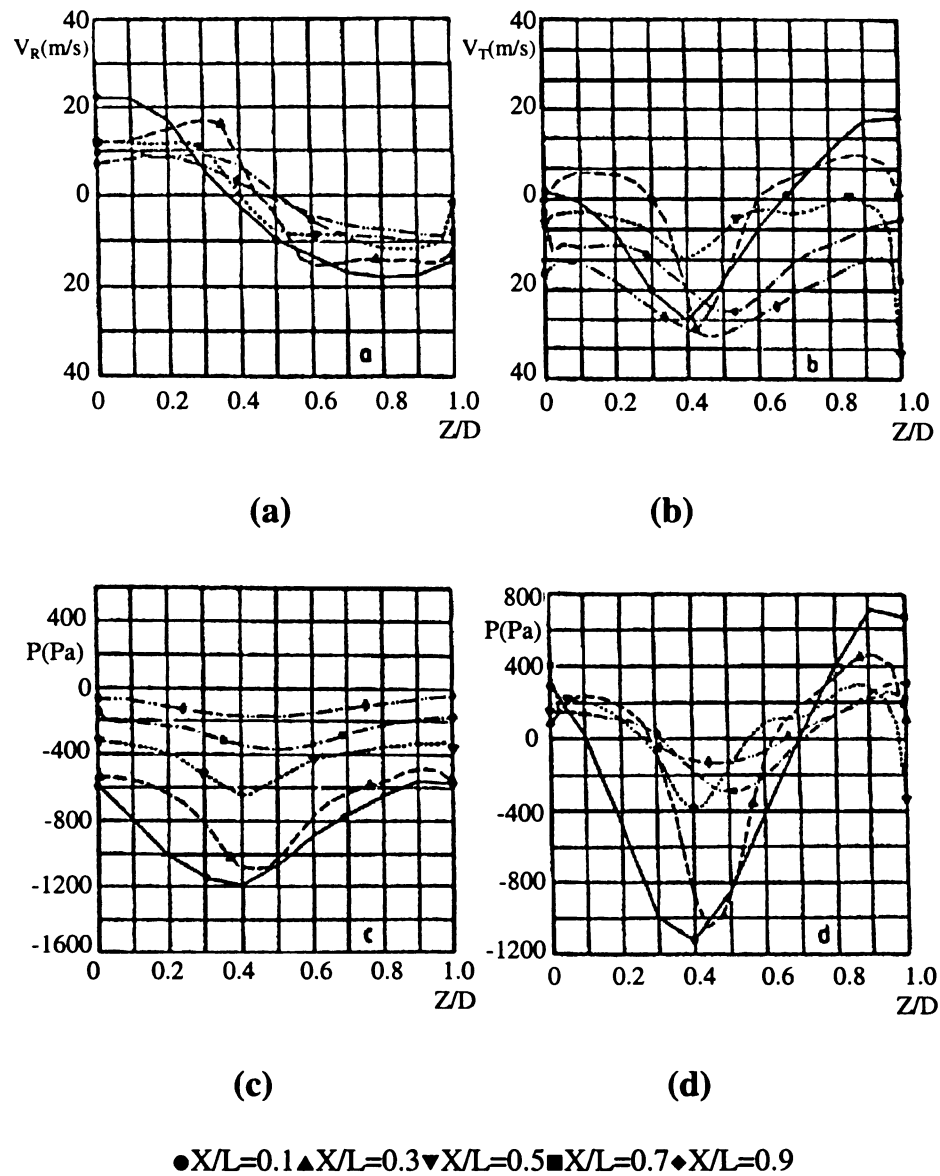
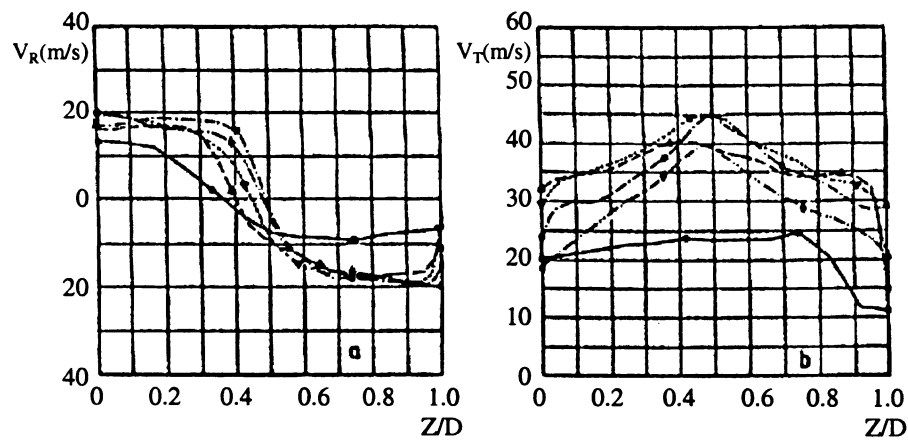
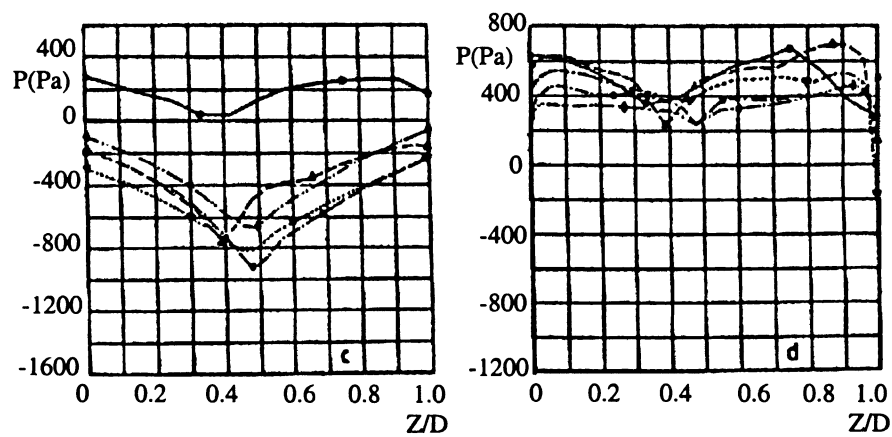


Figure 2.18 Measured velocity and pressure for small mass flow



(a)

(b)



(c)

(d)

● $X/L=0.1$ ▲ $X/L=0.3$ ▼ $X/L=0.5$ ■ $X/L=0.7$ ◆ $X/L=0.9$

Figure 2.19 Measured velocity and pressure for optimum mass flow

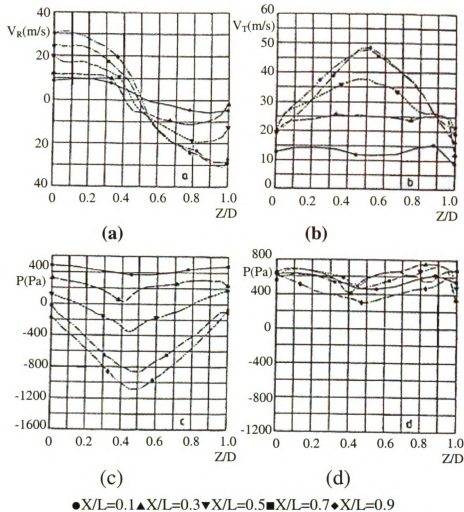


Figure 2.20 Measured velocity and pressure for large mass flow

Van den Braembussche and Hande (1990) presented a comparison of the performances of compressor volute in different operations. From fig. 2.18, 2.19 and 2.20, it is shown the swirl velocity V_r is constant in the region close to the walls and has a forced vortex distribution in the center. And, the velocity close to the walls is decreasing from volute tongue to outlet at minimum mass flow (fig. 2.18a). This results from a larger V_r at the volute inlet close to the tongue, where the static pressure is low and more fluid is aspirated. The opposite situation is clearly observed at maximum mass flow (fig.

2.20a). And, the forced vortex type region occupies almost the 30% part of the middle axial locations no matter how large the mass flow is.

For V_t , it shows a minimum in the volute center at low mass flow (fig. 2.18b) and a maximum at the high mass flow operating points (fig. 2.20b). At low mass flow, a deceleration of the tangential velocity takes place from tongue to outlet and the volute acts like a diffuser. The swirl component keeps the fluid close to the walls and a zone of low through-flow velocity occurs in the center. This reduces the effective cross section, decreases the static pressure recovery and avoids flow separation at the walls. An opposite phenomenon takes place at high mass flow. The increasing through flow velocity towards the center of the cross section can explained by the following relation

$$P^0 - P = \frac{\rho}{2} (V_T^2 + V_s^2) \quad (2.28)$$

The variation of static pressure over the cross sections is determined by the radial equilibrium between the static pressure gradient and the centrifugal forces resulting from the swirling flow

$$\rho \frac{V_s^2}{R_c} = \frac{dP}{dR} \quad (2.29)$$

The static pressure therefore increases from the center towards the walls at all three operating points (fig. 2.18c, 2.19c, 2.20c).

From equation (2.28) and (2.29), we can see a decreasing static pressure and decreasing swirl velocity towards the center of the vortex lead to an increasing through flow velocity towards the center (fig. 2.20b). The small difference between the total pressure and static pressure at the center of the cross section at low mass flow results in a low through flow velocity (fig. 2.20b).

The static and total pressures show nearly symmetric distributions over each cross section with a minimum at the center. The minimum static pressure occurs close to the volute tongue at low mass flow (fig. 2.18c) and close to the volute outlet at high mass flow (2.20c). The largest total pressure variations are observed at low mass flow (2.18d). These are much smaller at medium and maximum mass flow (fig. 2.19d and 2.20d) where a variation between volute tongue and outlet is observed.

The measurements indicate that the large variation in maximum total pressure between each cross section is mainly due to diffusion and friction in the inlet duct and inlet section. The cross-wise total pressure variation, and only part of the decrease of maximum total pressure are due to the swirling flow inside the volute. Friction in the volute is the main source of the total pressure losses at maximum mass flow.

For fig. 2.21, the pressure is increasing from volute tongue to outlet at less than optimum mass flow (fig. 2.21a). For optimum mass flow (fig. 2.21b), only a small pressure increase was observed and the discontinuous change of pressure for $0.0 < x < 0.2$ is typical for the flow perturbation in the tongue region. At high mass flow (fig. 2.21c), the volute is too small to accumulate so much fluid and the through-flow velocity is increasing towards the outlet. This results in a static pressure decrease between volute tongue and outlet.

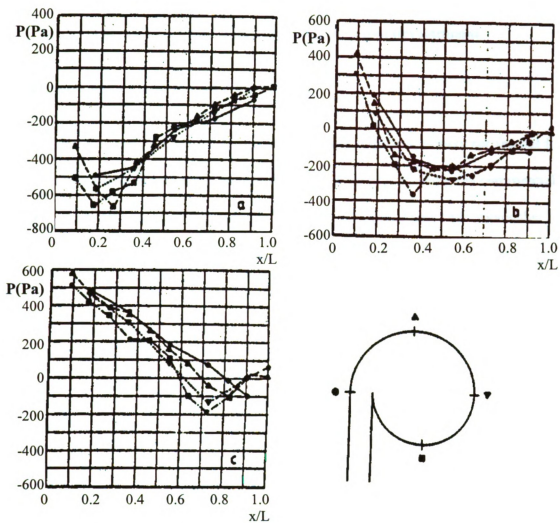


Figure 2.21 Longitudinal and circumferential static pressure variation corresponding to small (a), optimum (b) and large (c) mass flow

Chapter 3

Theory background and the integrated tool development

3.1 Computational Methods and CFD Models

Three-dimensional, compressible, steady flow computations were carried out for five compressor configurations, at Michigan State University, by using the commercially available computational fluid dynamics code, CFX-TASCflow. This code solves the Reynolds averaged Navier-Stokes equations in primitive variable form. The k- ϵ turbulence model was employed for these simulations. “Wall functions” were supplied to model the momentum and heat transfer processes for turbulent flows in the near-wall region.

3.1.1 Turbulence Model—k - ϵ model

It is well known that the derivation of the k- ϵ model is made for incompressible flows. But, the state of development of this turbulence model is such that it is also applied, essentially unmodified, for compressible flows. Actually, the k- ϵ turbulence model is used throughout this dissertation.

The equations for an incompressible flow are,

$$\frac{\partial}{\partial x_i}(\rho u_i) = 0 \quad (3.1)$$

$$\frac{\partial}{\partial t}(\rho u_i) + \frac{\partial}{\partial x_j}(\rho u_i u_j) = -\frac{\partial P}{\partial x_i} - \frac{\partial}{\partial x_j}(\tau_{ij} + \overline{\rho u'_j u'_i}) + S_{ui} \quad (3.2)$$

where the convention that any variable without a superscript is a mean flow variable. The term $\overline{\rho u'_i u'_j}$ that appears in the momentum equations is identified as the turbulent Reynolds stresses. The gradient diffusion hypothesis suggested by Boussinesq, is used to model the Reynolds stresses for a compressible fluid as:

$$-\overline{\rho u'_i u'_j} = \mu_t \left(\frac{\partial u_i}{\partial x_j} + \frac{\partial u_j}{\partial x_i} \right) - \frac{2}{3} \left(\mu_t \frac{\partial u_l}{\partial x_l} + \rho k \right) \delta_{ij} \quad (3.3)$$

where μ_t is the turbulent viscosity and k is the turbulent kinetic energy defined as

$$k = \frac{\overline{u'_i u'_i}}{2} \quad (3.4)$$

The turbulent viscosity μ_t is modeled as the product of a turbulent velocity scale, V_t , and a turbulent length scale, l_t , as proposed by Prandtl and Kolmogorov. The constant gives

$$\mu_t = \rho c_\mu l_t V_t \quad (3.5)$$

Both one and two equation models take the velocity scale V_t to be the square root of the turbulent kinetic energy

$$V_t = \sqrt{k} \quad (3.6)$$

The turbulent length scale is algebraically specified in a one-equation model and determined from an additional transport equation in a two-equation model. In the standard k - ε two-equation model it is assumed that the length scale is a dissipation length scale, and when the turbulent dissipation scales are isotropic, Kolmogorov determined that

$$\varepsilon = \frac{k^{3/2}}{l_t} \quad (3.7)$$

where ε is the turbulent dissipation rate.

If k and either ε or l_t are known, the turbulent viscosity can be determined from equation (3.5) and the Reynolds stresses can be computed using equation (3.3), thereby closing the time mean averaged turbulent momentum equations, equation (3.1)-(3.2). The remaining task is to determine the equations for k and ε and the appropriate boundary conditions.

Equations (3.5), (3.6) and (3.7) should be paid more attention because they are needed in the initial guess for the flow field.

In this dissertation, the dependence of the solution on turbulence models has not been studied. A comprehensive assessment has been made by Lakshminarayana on the computation of turbomachinery flows using $k - \varepsilon$ turbulent model. So far, the results by using this model are in a good agreement with the experimental data. And, one thing needs to be mentioned here, all the above equations are from the TASCFlow software user manual.

3.1.2 Two CFD models for centrifugal compressors

Because of the complex geometry of turbomachinery, usually the grid for whole turbine and centrifugal compressor has to be divided into quite a few sub-grids, for instance, impeller grid, diffuser grid, volute grid and exit cone grid. Undoubtedly, the impeller grid has the relative movement to the diffuser grid. Volute grid is stationary relative to diffuser grid. The MFR (Multiple Frame of Reference) capability in CFX-TASCflow3D uses the Stage and Frozen Rotor concepts to catch the relative movement.

So the fundamental to the MFR capability is the fact that the computational domain consists of two (or more) distinct regions that are in relative motion to each other. A sliding interface condition is used to connect two regions together that are in different frames of reference. The sliding interface is implemented in such a way that steady state solutions are supported in each frame or reference. A generic sliding interface approach is used for both Stage and Frozen Rotor interfaces; specific implementation details of the interface condition distinguishes between the two approaches.

A sliding interface condition is used to connect control volumes together on each side of a sliding interface. According to the AEA manual, this sliding interface condition has the following properties:

1. The interface accounts for the change in the frame of reference.
2. The interface supports steady state predictions in the local frame of reference, on each side of the interface.
3. Strict conservation is maintained across the interface, for all fluxes of all equations.
4. The interface treatment is fully implicit, so that the presence of an interface does not adversely affect overall solution convergence.
5. The interface accounts internally for pitch change by scaling up or down (as required) the local flows as they cross the interface.
6. Any number of frame change interfaces is possible within a computational domain.

It is important to note that the extent of the grid surfaces on each side of a given sliding interface do not have to be equal. For example, the grid numbers of impeller on a

rotor and the grid numbers on adjacent diffuser are usually different hence the pitch changes between the components. Unequal pitch is accounted for internally by the sliding interface condition implementation within CFX-TASCflow3D. Conservation is maintained in the sense that the total flow from one frame into the next scales exactly on the surface area based on pitch ratio. So, this character makes the grid generation for the both sides of sliding interface undependable.

3.1.2.1 Stage Rotor

Stage rotor is one of the CFD models that are suitable for turbomachinery simulation. By using this model, one or more blade passages can be solved simultaneously with circumferential “averaging” between the impeller grid and the diffuser grid. Steady state solutions are then obtained in each sub-grid. The stage averaging at the sliding interface between the impeller grid and the diffuser grid incurs a one-time mixing loss. This loss, according to the TASCFlow manual, is equivalent to assuming that the physical mixing supplied by the relative motion between components is sufficiently large to cause any upstream velocity profile to mix out prior to entering the downstream machine component.

Although the unsteadiness in volute is generated by the variation of the flow at the outlet of the rotating impeller, Hillewaert indicates that the mixing of the blade-to-blade flow is very fast. So this is the theory base of the stage model.

Stage analysis is most appropriate when the circumferential variation of the flow is of the order of the component pitch. Since stage model averages between blade

passages in terms of time average interaction effects and neglects transient interaction effects, it is not appropriate when the circumferential variation of the flow is significant relative to the component pitch.

Figure 3.1 is used to shown the stage interface between the impeller grid and diffuser grid. It can be seen only one passage of impeller grid is attached with the diffuser and volute grid. It's assumed that all the other passages of impeller grid experiences the same flow as in the passage shown in the figure. And, the exit flow of the impeller is averaged circumferentially.

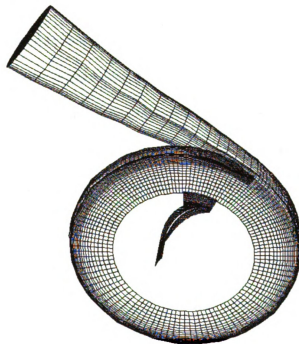


Figure 3.1 the stage rotor

Based on the introduction above, it is easy to understand the reason why there will be always periodic boundary condition exists in the stage model.

3.1.2.2 Frozen Rotor

The frozen rotor can also be used to predict the “steady state” flow of an impeller, a diffuser and a volute, where the impeller is solved in a rotating frame, the diffuser and volute is solved in the stationary frame. As introduced in the TASCFlow manual, the two frames of reference connect in such a way that they each have a fixed relative position throughout the calculation, but with the appropriate frame transformation occurring across a sliding interface. A steady state solution is obtained to a multiple frame of reference problem, with some account of the interaction between the two frames. The quasi-steady approximation involved becomes small when the through flow speed is large relative to the machine speed at the sliding interface.

Contrary to the State Rotor, Frozen Rotor analysis is most useful when the circumferential variation of the flow is large relative to the component pitch.

Again, transient effects at the frame change interface are not modeled. Modeling errors are incurred when the quasi-steady assumption does not apply. Also, the losses incurred in the transient situation as the flow is “mixed” between stationary and rotating components is not modeled.

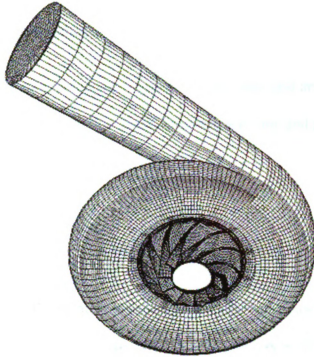


Figure 3.2 the frozen rotor

Pitch change across a Frozen Rotor interface is more difficult to quantify.

TASCFlow manual explain the way to handle this kind of problem is: the flow profiles are preserved as they cross the interface, but are scaled (stretched or compressed) in the direction of rotation by the pitch ratio.

Figure 3.2 is the frozen case for this study. In this model, the exit flow is no longer assumed to be uniform and flows in each passage are not assumed to be periodic either. All the impeller passages, attached with the diffuser grid, will be simulated together. In order to run this case, the first step is to rotate one passage of impeller grid to get all the impeller passages, and then to attach them together, or to use another way to make a one-block impeller grid. The latter is preferred because it is more convenient for the grid attachment and the post processing.

3.2 Integrated tool development

The integrated tool includes sub-grid generation, sub-grid attachment/append, boundary condition definition, initial guess, time step selection and post-processing. All of these respects will be explained in detail as follows.

3.2.1 Sub-grid generation

It is well known that a lot of commercial software can be used for impeller grid generation, such as bladegen and TASCgen. However, until now there is no commercial software specifically used for volute grid generation. In this study, a FORTRAN code was made to generate “butterfly” grids for compressor volutes. The code reads in the volute and diffuser geometry file (from company) and a control file (self-made) first, then writes out input files for TASCGrid, **.gdf*, **.cdf*, **.sdf* and **.idf*. Thereafter, TASCgrid, the commercially available grid generator, can be run to generate all the sub-grids for volute and diffuser. For the view of diffuser and volute grid, please see the figure 3.1 and 3.2.

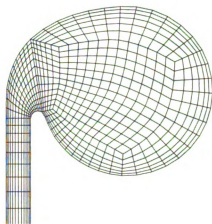


Figure 3.3 Butterfly grid of volute

The grid of the volute is of butterfly section (see figure 3.3) to reduce the grid skewness. The commercial impeller grid generator, TASCgen, is employed to generate the impeller grid. In some cases, an alternative code, Fast_TASC, that was generated by Solar Turbines, Inc, was used for the impeller grid generation. Usually the impeller grid number is 20,000 points for one passage of the impeller, and the whole impeller grid number can be obtained after timing the blade numbers.

3.2.2 Sub-grids attachment and append

There is one integrated tool that has been generated for the sub-grids attachment and append automatically. What need to do is just get the tool first, then follow the procedures below to get the “stage” and “frozen” rotor.

If the “stage” case simulation is desired,

1. Make two new directories--“**volute**” and “**stage**”-- under one directory.

2. Copy all the files under “**Tool/volute**” directory and volute geometry file to your own “**volute**” directory. Modify the volute control file according to the new volute geometry file. Make your own “**input.file**”.
3. Run “**solar.f**”. Make sure you know the z value of the impeller [id,1,kd] node.
4. Run “**subgrid**” to generate the 4 sub-grids. Note: The sub-grids would not be appended together at this time.
5. Copy “**grd**”(one passage grid of impeller), “**gci**”, “**pro**” to your own “**stage**” directory from your *Impeller* directory
6. Copy all the files under the “**Tool/stage**” directory to your own “**stage**” directory.
7. In your own “stage” directory, replace the region definition part *stage.gci* by the region definition part of impeller *gci* file *gci*.
8. Run “**attach_append**”. Then check grid quality. If the grid quality is bad, go back to run the “**solar.f**” again after changing the parameters in volute control file.
9. Redefine the Impeller rotation speed (only the “default” speed), material properties and inflow/outflow boundary conditions in TASCFlow GUI.
10. Give the initial guess (see part 7) and start the run from “solve monitor”.

If the “**frozen**” case is desired,

1. Make two new directories--“**volute**” and “**frozen**”-- under one directory.
2. Repeat 2, 3 and 4 steps of the stage case to generate the volute and vaneless diffuser sub-grids.
3. Copy “**grd**” (one passage grid of impeller) and “**gci**” to your own “**frozen**” directory from *Impeller* directory

4. Copy all the files under the directory **“Tool/frozen_smooth”** to your own **“frozen”** directory.
5. Replace the region definition part of **“frozen.gci”** in your **“frozen”** directory by that of **“gci”** in your impeller directory.
6. Run **“answer.for”** to generate all the answer files for batch files. Notice: You should keep the blade number and the blade grid size at hand before you run the **“answer.for”**.
7. Run **“Impeller.bat”** file to generate all the impeller grids.
8. Run **“attach_append”** to attach all the impeller grids and all the volute sub-grids.
9. Run the macro **“REGION_DEF”**.
10. Redefine the Impeller rotation speed (only the **“default”** speed), material properties and inflow/outflow boundary conditions in TASCFlow GUI.
11. Give initial guess and run the whole compressor simulation.

Notice: So far, for frozen case, the blade number is up to 17. If you have more blade numbers, a little bit change on **“answer.for”** and **“solar30.mac”** should be done before you run frozen case.

3.2.3 Boundary Conditions

Inlet boundary conditions are assigned as total pressure, total temperature, flow angles, turbulence intensity and turbulence eddy length scale. Outlet boundary condition is defined by mass flow rate.

As mentioned above, equations (3.5), (3.6) and (3.7) are used for the estimation of the turbulence parameters.

There are two sample boundary conditions files have been done respectively for stage and frozen rotor. Just copying the two files to the working directory, all the boundary condition will be defined automatically. Of course, material properties should be modified manually

3.2.4 Initial guess

According to the following rule to generate the initial guess, it has been proved to be very efficient.

1. Be sure that the design mass flow rate is selected first;
2. The velocity = $0.9 \times$ the INLET velocity; align the K node direction;
3. The pressure = $0.65 \times$ inlet total pressure value;
4. The temperature = $0.85 \times$ inlet total temperature value;
5. Tu intensity and Eddy length scale are from spreadsheet (same as the values that can make impeller alone case converge);
6. Off-design cases use design condition converged result as initial guess.

In some cases, this kind of initial guess still has big difficulties. Even if it converged very well at first beginning, the solution curve waves continuously and will never converge further when the maximum residual almost reaches the 1.0×10^{-4} . This is because a bad time step has made a hurt at the very beginning already.

Usually, in commercial CFD software, such as StarCD and Fluent, there is a relaxation factor that can be used to help converge. However, in TASCFlow, there is no such a kind of parameter to control the convergence. The converge process in TASCFlow strongly depends on the initial guess and time step selection. Once the initial guess is set appropriately, the rest thing is how to choose a appropriate time step to make the simulation converge. Fortunately, there is a similar function parameter in TASCflow to control the relaxation—“*dtime*”. When obtaining steady state solutions, the time step by using this parameter effectively provides relaxation to the solution procedure. Relaxation is necessary because the CFX flow code is solving a set of non-linear equations as a sequence of linear problems. The role of the time step becomes more important as the problem non-linearity increases. So the best way to make the impeller, diffuser and volute case converge is to set the initial guess as mentioned above first, then use the “*dtime*” instead of the “*etfact*” parameter to control the converge process as follows,

I. Set the $dtime = \frac{1 \times 10^{-5}}{RotationSpeed \omega(r/s)}$;

II. If it looks converge and the trend is pretty good after 30-50 steps, set

$$dtime = \frac{1 \times 10^{-4}}{RotationSpeed \omega(r/s)} \text{ (Otherwise set } dtime = \frac{1 \times 10^{-6}}{RotationSpeed \omega(r/s)} \text{)}$$

III. If everything is ok after another 20 steps, ten times the old *dtime* parameter again.

IV. The correct method should increase *dtime* in this way until the solution converged and finally the *dtime* can be as big as 1000. But, since the parameter *etfact* has been proved to be accurate enough to guarantee a correct solution, feel free to change the parameter from *dtime* to *etfact* when the trend is pretty good. Thus, we can leave the computer run overnight, no need to sit in front of it to modify the

dtime value from time to time. Usually, the *etfact* should be set around 5. 3 is preferred. This is a worry-free value.

Two cases that cannot converge even set the *etfact* as 1 for the same initial guess has been made converged by using this method.

3.2.5 Post-processing

A postprocess macro—“solar30.mac”—is also ready for use. The specific heat at constant pressure, specific heat ratio, blade numbers, tip diameter of impeller and I grid number at pinch position would be asked for input while you are running the macro.

The following five equations were built in the macro for the performance prediction. The equation (3.8), (3.9) and (3.10) are from the technical handbook at Solar Turbines, Inc.

$$\Phi = \frac{Q_1}{\frac{\pi}{4} \times D_{tip}^2 \times U_{tip}} \quad (3.8)$$

$$H_{isen} = 778.3 \times C_P \times T_1 \times \left[\left(\frac{P_2}{P_1} \right)^{\frac{k-1}{k}} - 1 \right] \quad (3.9)$$

$$\psi_{isen} = 63.34 \times \frac{H_{isen}}{U_{tip}^2} \quad (3.10)$$

$$c_p = \frac{p - p_4}{p_{04} - p_4} \quad (3.11)$$

$$\omega = \frac{P_{04} - P_0}{P_{04} - P_4} \quad (3.12)$$

Equation (3.11) and (3.12) are for the pressure recovery coefficient and total pressure loss coefficient calculation. The subscript 4 means the pinch position and 0 means total properties.

After reading the “solar30.mac” in, run “initialize” first, then follow the screen output to get the desired output. In order to get the tablet output, please run the “volute_post”.

The impeller output is in the “Inflow & outflow of Impeller” block. Here the impeller outlet is at the pinch position. If a different position would be selected as the impeller outlet, please input the desired I grid number when answering the question “Please input the I grid number at the pinch position” while running the “volute_post”.

The results in “Flow Properties in Vaneless Diffuser Outlet”, “Flow Properties in Volute Throat” and “Exit Cone Flow Properties” are 360-degree circumferential averaged value.

The results in “Circumferential Flow Properties in VOLUTE” are radial (from diffuser outlet) mass averaged result. The radial area position (K direction) starts from 11 and the step is 10. The last station in this block is at the tongue position. However, if different circumferential K size was defined in the volute control file, corresponding modification should be made in the “solar30.mac”.

The results in “Circumferential Flow Properties at Diffuser Outlet” are mass averaged in two adjacent circumferential K grids, see the rectangular enclosed by thick lines in figure 3.4.



Figure 3.4 Averaged area at diffuser outlet

The actual circumferential angle for the two circumferential flow properties depends on the tangential node distribution. If some important position was missed, please modify the macro to satisfy the requirement.

3.3 Code robustness and grid improvement

3.3.1 Code robustness

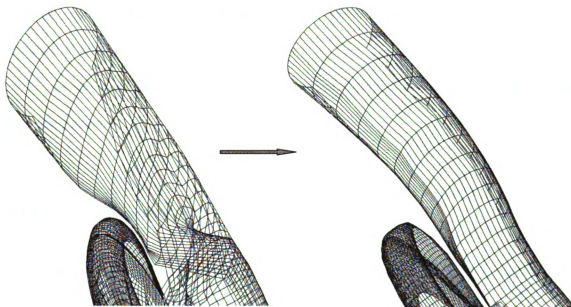


Figure 3.5 One example of code robustness

At very beginning, the code for volute and diffuser grids generation has many bugs in it. For one case, maybe the code works fine, but, there are always a lot of problems for grid generations if the volute and diffuser geometry file was changed. One example of the problems is shown in figure 3.5. In this figure, the problem is from the starting point of exit cone sections are different from the ones of volute section in the geometry file. We can see that there are many cross grids occur near the tongue position in the left figure in figure 3.5. This kind of grid will incur quite a few negative control volumes in the volute grid, so it even cannot be read in by TASCFlow. After debugging the code, the right one is shown in the right figure in figure 3.5. It can be seen all the control curves near tongue position are parallel now.

And, many other problems are also solved by making the code robust. For example, the code is no longer sensitive to the data sequence in the volute and diffuser geometry file, point numbers on the half circle at the volute/diffuser interface and the distance of adjacent points.

In one word, this code is very robust for the routine use for the volute and diffuser grid generation.

3.3.2 Two new functions in the code

Besides generating the grids according to the original geometry file, there are another two new functions added in the code.

The first one is the volute volume can be changed freely. Figure 3.6 shows an enlarged volute (outside contour) based on the original one (inner contour). The butterfly

grid control curves are in the middle. Of course, the volute volume can also be decreased in the same way. Thus, the effect of volute volume on the performance of the whole compressor can be investigated because this new function makes the volute volume change as many times as you want. However, because the exit cone keep unchanged in this process, it is inevitable to meet a geometry “step” on the connection surface between volute and exit cone. Another disadvantage is there is no experimental data to validate the CFD result of the modified volute since there is no such a volute exist at all. So this function is only for research interest, or for the numerical test at the beginning of a volute design.

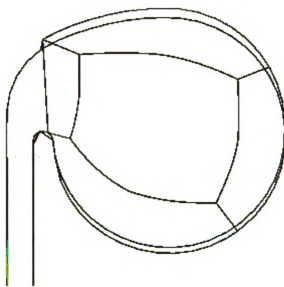


Figure 3.6 Enlarged volute

The second function is that the shroud wall of the vaneless diffuser can be moved to or away from the hub wall. Since the diffuser is the component that connects the impeller and volute, any grid combination of volute and impeller is possible if the width of the diffuser can be changed randomly. So this new function can be used to investigate

any combination of current volutes and impellers. For this method, the experimental data are always available for the CFD results validation because we can use same way to build up a test rig at the Aero Test Facility. Figure 3.7 is the example to move the shroud wall of the diffuser to hub wall. This analytical method was adopted in Chapter 5 and 6.

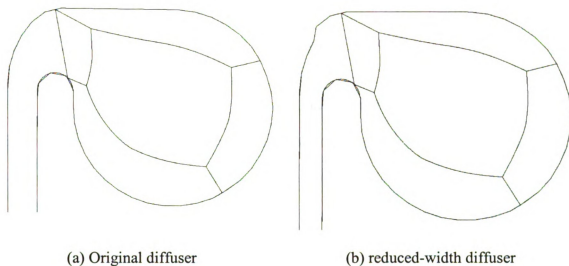


Figure 3.7 Reduced-width vaneless diffuser

3.3.3 Grid quality improvement

Even if the volute and diffuser grids can be generated successfully, there are a lot of jobs to do on the grid volume, skew and aspect, i.e. grid quality. In figure 3.8, it can be seen that the half circle became smoother and grid angle increased a lot from the left figure to the right figure. Since the skew angle in TASCFlow requires more than 20 degrees, this improvement reduce a great deal of warnings, even errors.

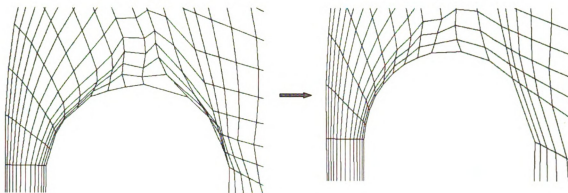


Figure 3.8 Grid improvement (1)

Figure 3.9 shows the twist grid control curves from the last volute section to the first exit cone section. Notice, here only the control curves are plotted in order to give a clear view. Sometimes, TASCFlow would not give any warnings for this kind of grid. However, it will take a much longer computer time to get a converge solution based on this kind of grid. So to correct this defect is profitable. The figure of 3.9 (b) is the corrected control curves. It looks much better now. And, the new grid only took one third of total time of the old grid to get the final converge solutions.

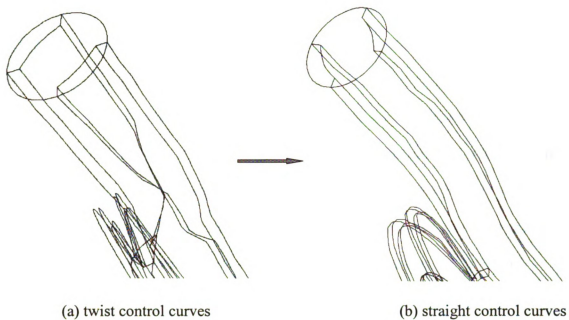


Figure 3.9 Grid improvement (2)

3.4 Aero Test Facility

The Aero Test Facility is located at Solar Turbines, Inc. Kearny Mesa Facility, San Diego, California. From the test report prepared by Dr. Jean-Luc Di Liberti, we can get a clear conception of the experiment.

The test article and closed loop piping are indoors. Air or nitrogen can be the test gas. A gearbox coupled with an electric motor drives the test article. Oil and seal gas is supplied to the compressor and gearbox with facility resources.

Two valves in parallel operation control compressor flow. The valves are located downstream of the discharge flange. The discharge gas is cooled by water/gas heat exchangers.

The heat exchangers use plant resources for cooling water. Auxiliary pumps, coolers and valves are used to control the electric motor, loop pressure and temperature and seals.

Flow was determined using a bellmouth venturi located upstream of the compressor inlet flange. Four temperatures, four total pressures and four static pressures are measured at the venturi, compressor inlet and compressor discharge ports so there is sufficient instrumentation to determine flow, head and efficiency. Four measurements provide sufficient instrumentation for redundant practice and assess the flow field.

At the compressor flanges, the 4 probes are located 90 degrees apart and at 4 different immersions satisfying equal areas.

The data acquisition system is proprietary software purchased/designed by Solar Turbines, Inc. Pressures are required with a pressure systems Inc. (PSI) system. All measured pressures are referenced to ambient pressure and calibrated on line during the test.

A SCXI temperature system incorporating type T thermocouples was used to measure temperatures. The thermocouples are calibrated with a reference RTD and calibration coefficients are developed to provide an accuracy of $\pm 0.2^{\circ} F$ in the anticipated temperature range.

Raw data was reduced online with the proprietary software. Three files: pressures, temperatures and reduced data are stored at the end of each test.

The facility, or system stability is a result of the interaction of: suction pressure and temperature control systems, test article thermal inertia, oil supply temperature, seal leakage, and the loop and instrumentation plumbing. Gross values such as speed, flow

and suction values stabilized within 3-5minutes after a flow change. The system averaged consistent fluctuations of approximately ± 0.5 Psi, and $\pm 1.0^{\circ} F$.

In the experiments, the data quality was very good. When data is averaged a minimum of 25 seconds, the standard deviation of efficiency is usually within ± 0.1 points.

Chapter 4

Solution repeatability and previous work verification

4.1 Introduction

Two single-stage centrifugal compressors were simulated in this chapter. There are two reasons to run the cases. The first one is to check the solution repeatability, i.e. the reliability of the CFD method. The second one is to verify the basic flow structures in diffusers and volutes that have been given in the papers mentioned in chapter two.

All the information about the theory background of the CFD method and the test facility has been introduced in chapter 3. And, since this chapter is not focus on the comparison research of the compressors, the compressor geometries and the test procedures are not discussed here. What we are interest in is to take a look at the match between the CFD results and the experimental data, and to understand the flow phenomenon based on the CFD analysis.

4.2 The study for D3-1 compressor

The performance figure (figure 4.1) is for the D3-1 case at Solar Turbines, Inc. The impeller is a shared one for D3-1 and E2 stage compressor. The difference between the two compressors is the widths of the two diffusers. Here, six points including the design condition were run for the comparison with the test data. The test data were read from the figures in the D3-1 test report that was written a few years ago. It shows that the CFD results match the experimental data very well. The CFD points are above the experimental curve mainly due to the fact that the CFD model did not incorporate the

leakage flow in the labyrinth between the shroud outer wall and the machine case, and the back surface friction of the impeller was also not taken into account.

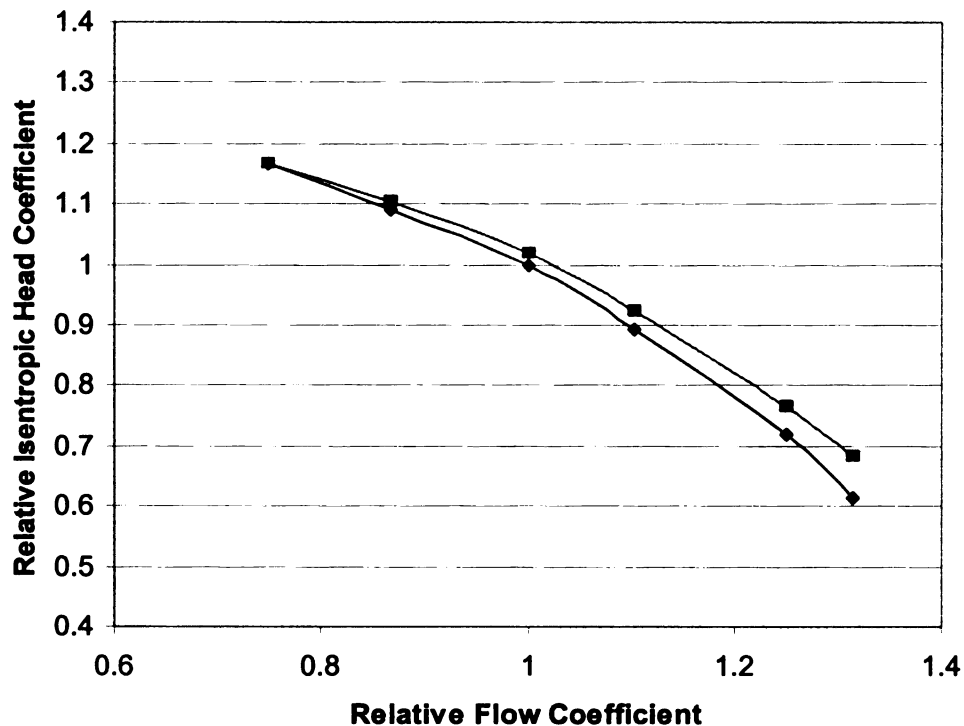


Figure 4.1 Compressor performance

The efficiency at different locations in the D3-1 stage case is shown in Figure 4.2.

From this figure, it can be seen the design mass flow always has the best efficiency.

Apart from the design mass flow (75% vs. 125% design mass flow; 86.8% vs. 110.4% design mass flow), the high mass flows have a good performance. For low mass flow cases (75% and 86.8% design mass flow) the loss in diffuser is big and the loss in the volute cone part is small. For design mass flow and high mass flow, the loss in vaneless diffuser is kind of small. However, it becomes very big in the volute cone part. Note that the volute cone part is from station 7 to station 8.

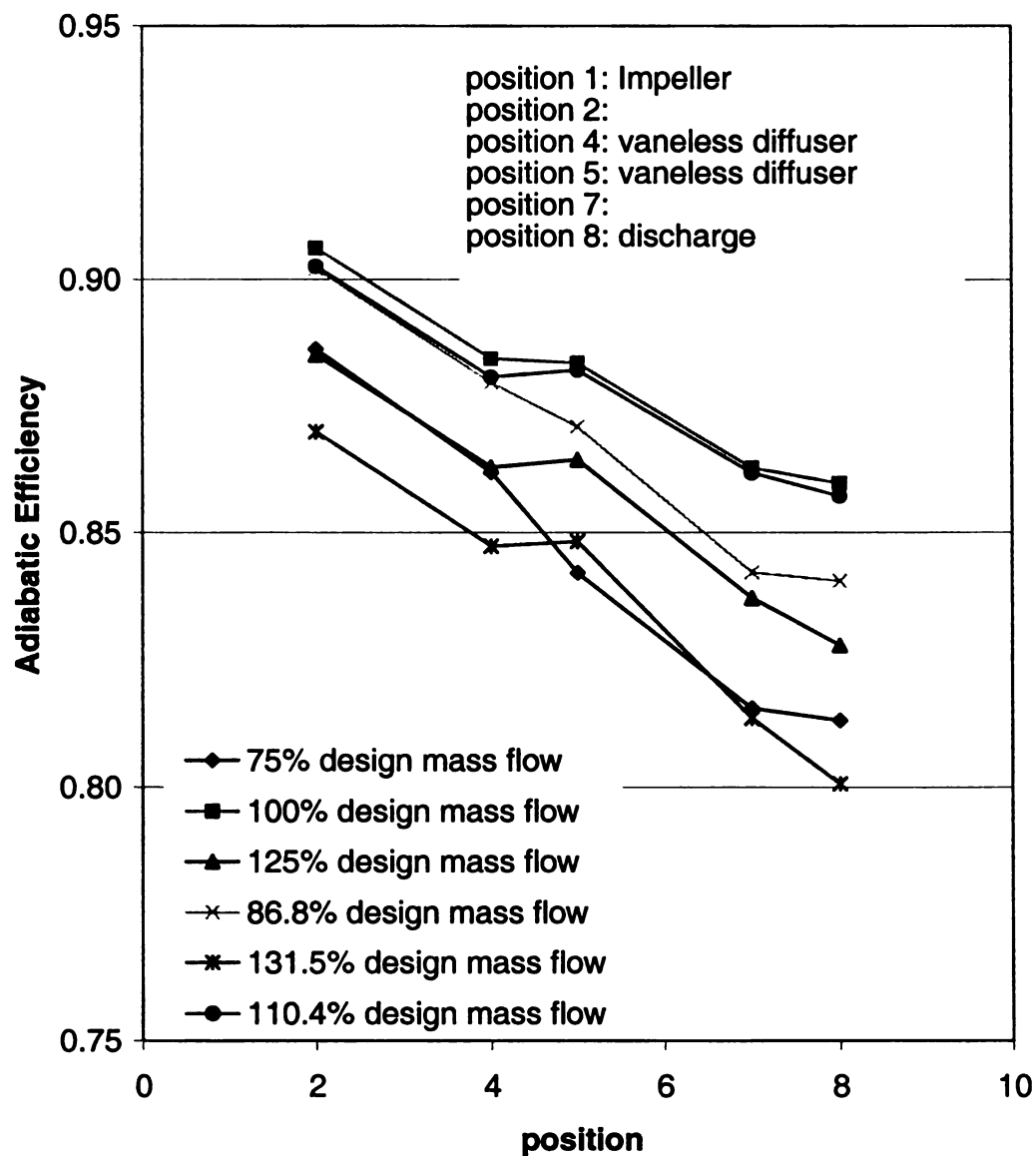


Figure 4.2 Efficiency of different stations at different mass flows

This trend can also be proved from figure 4.3. It shows that the total pressure drops more at low mass flow than at high mass flow in the vaneless diffuser. And this situation reversed in volute cone part.

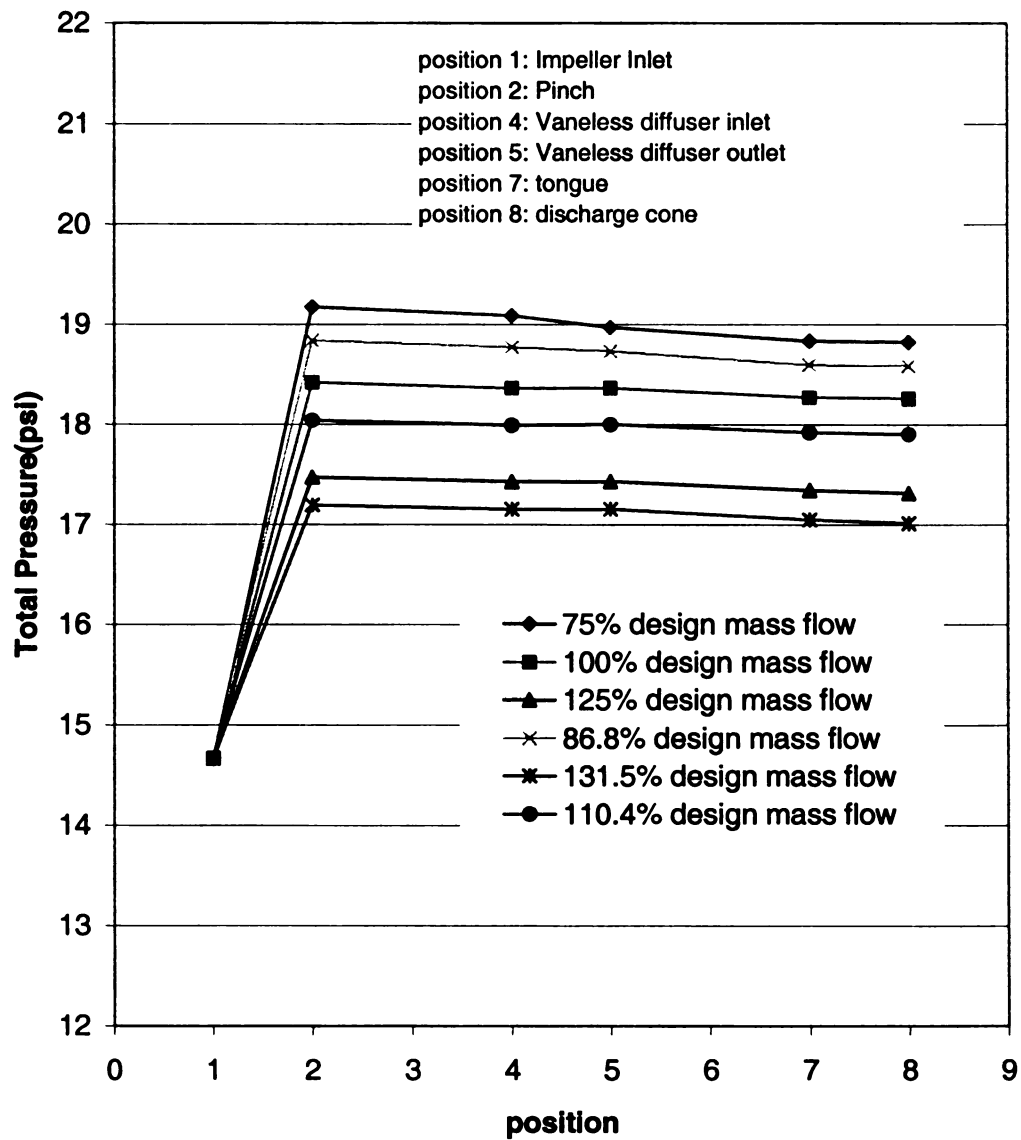


Figure 4.3 Total pressure of different stations at different mass flows

According to the static pressure map, figure 4.4, the static pressure at low mass flow is always higher than the static pressure at the high mass flow at the same station. This result can also be found numerically from figure 4.5. For instance, at the volute

inlet, the static pressure is 2.215E2 at 75% mass flow, 2.162E2 at design mass flow and 2.071E2 at 125% mass flow.

At high mass flow (110.4% and 125% design mass flow), the volute is too small to accumulate so much fluid and the through-flow velocity is increasing between vaneless diffuser outlet (station 5) and tongue (station 7). This results in a static pressure decrease between volute tongue and compressor outlet. From the tongue to the volute outlet, the static pressure recovered a little bit and increased again because the cross section area of the exit cone becomes bigger.

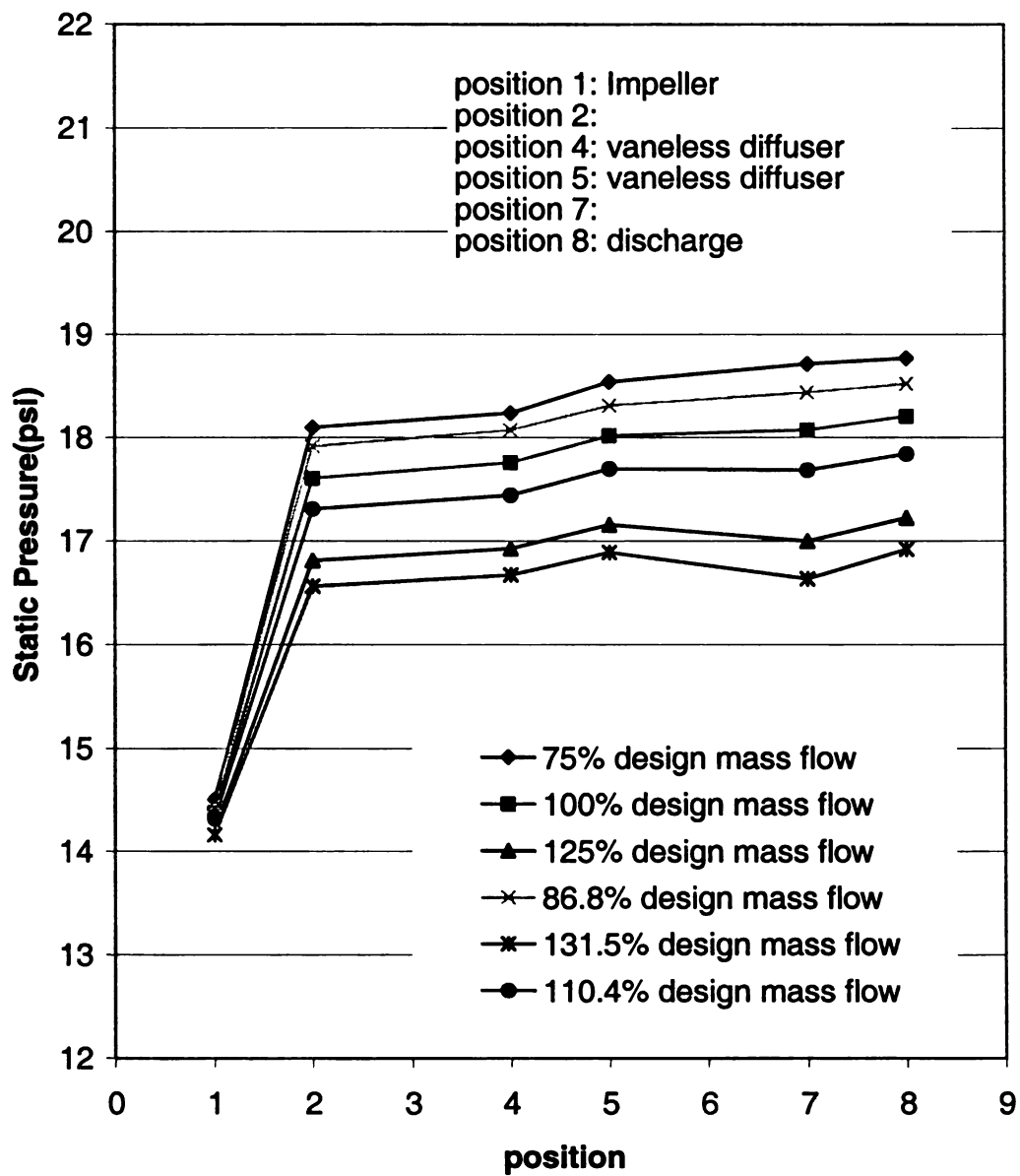


Figure 4.4 Static pressure at different stations at different mass flows

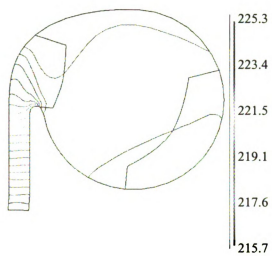
And, from the figures 4.6 and 4.7, it can be found that the radial velocity is $7.749\text{E}2$ at 75% mass flow, $1.217\text{E}3$ at design mass flow and $1.469\text{E}3$ at 125% mass flow at the volute inlet part. For tangential velocity, it is $-2.396\text{E}3$ at 75% design mass flow, $-2.52\text{E}3$ at design mass flow and $-6.336\text{E}2$ at 125% design mass flow.

The higher static pressure at low mass flow (figure 4.4) should lead to a lower radial velocity and higher tangential velocity. This means the radial velocity is lower at low mass flow than the radial velocity at high mass flow. The small radial and large tangential velocity at the impeller outlet means the fluid would move a longer distance from the impeller outlet to the volute inlet. Long distance (long pathline) flow leads a bigger friction loss in the diffuser. It will lead an adverse pressure gradient in the boundary layer and the separation occurs in the hub wall. Figure 4.8 shows the phenomenon. This is the reason why the loss in the vaneless diffuser is bigger at low mass flow. So we can expect it will be much helpful to shorten the length of vaneless diffuser at low mass flow and lengthen the length at high mass flow.

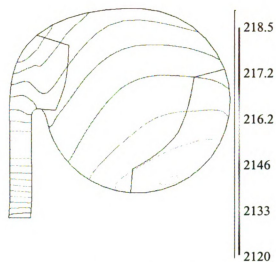
One interesting phenomenon is that the CFD results indicate the tangential velocities are also low in low mass flow. This is also can be explained from the high diffusion and high friction losses because of the long pathlines of the fluid particles.

It is common now to expect a large radial velocity at high mass flow. Observing the figure 4.7 at 125% design mass flow carefully, it can be found the radial velocity hit the shroud wall is so severely that it leads to a reverse flow in the hitting part (green contour line part which means a positive value) when the radial velocity is big enough. This is the reason why the losses in the volute are relative bigger when the mass flow is higher than the design mass flow. We can call this phenomenon as a volute stall.

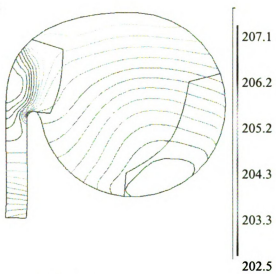
This phenomenon can also be obtained from the figure 4.9. In all of these figures, radial velocity evolved into the swirl velocity after the fluid flows into the volute. A low static pressure at the impeller outlet leads to a large radial and a small tangential velocity at the volute inlet and therefore a strong swirling motion occurs inside the volute channel. So the swirl velocity in the volute is related to the radial velocity component at the volute inlet. The bigger radial velocity at high mass flow is, the bigger the loss in the volute would be.



75% design mass flow



100% design mass flow



125% design mass flow

Figure 4.5 Static pressure distribution at three mass flows

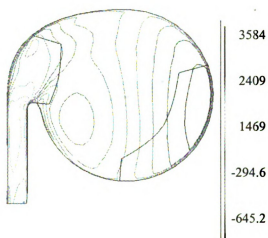
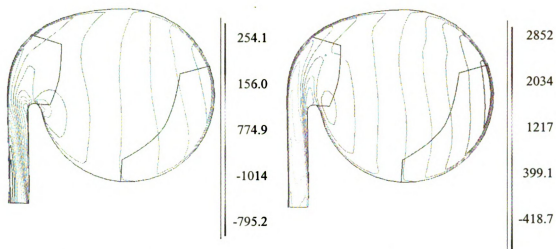
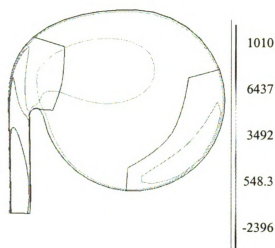
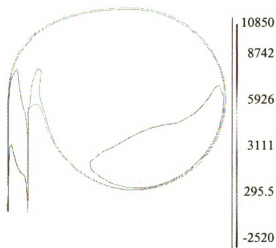


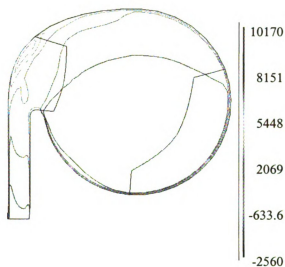
Figure 4.6 Radial velocity distribution at three mass flows



75% design mass flow



100% design mass flow



125% design mass flow

Figure 4.7 Tangential velocity distribution at three mass flows

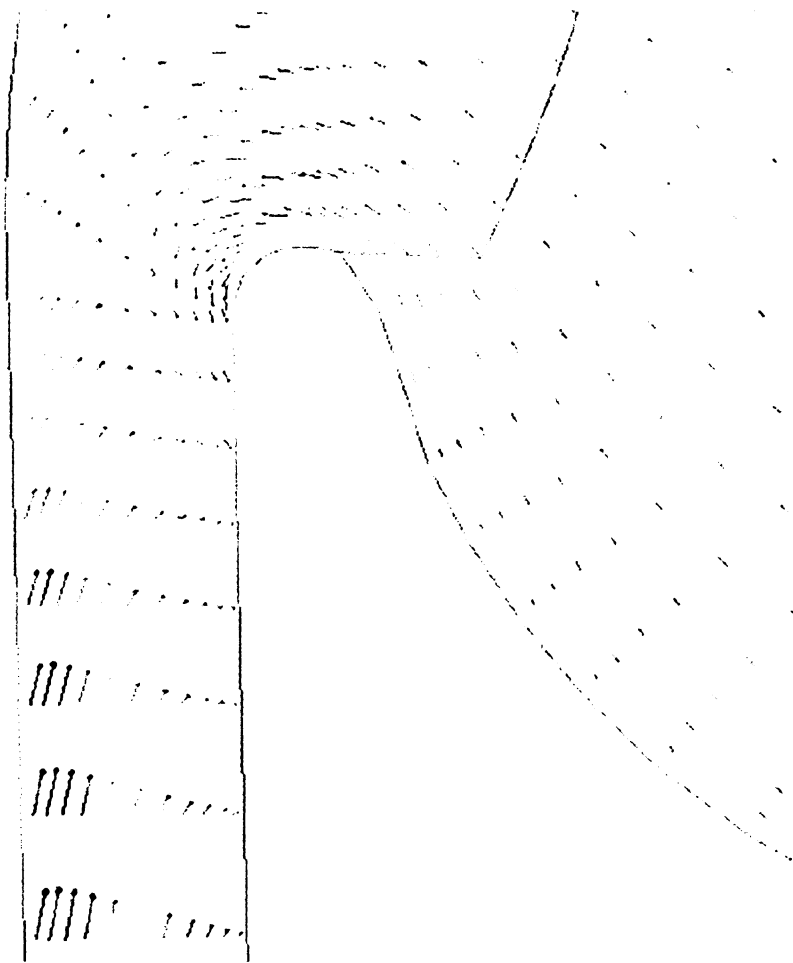
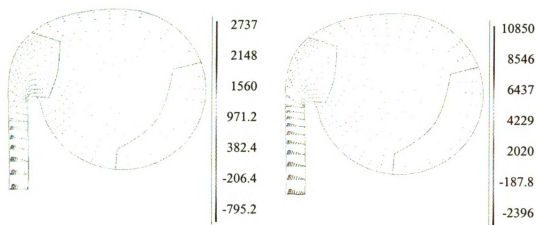
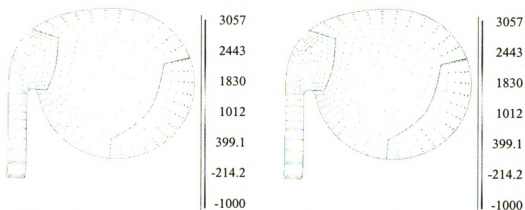


Figure 4.8 Diffuser stall



75% design mass flow



100% design mass flow



125% design mass flow

Figure 4.9 The contour plot of radial velocity

4.3 The study for D2 compressor

The volute and diffuser grids were generated by the same way of the self-coded program as the one in the chapter 3. After two cases, the program for grid generation has been improved greatly. It won't be sensitive to the volute geometry file so much as before.

As far as the CFD model and boundary conditions, same methods were used as the models in the chapter 3.

One more thing I want to mention is that only stage case was run for this case.

In figure 4.10, the difference between the experimental data and calculation data is kind of big. The reason is that there is no "actual" experimental data available for this case. The experimental data for comparison in this figure is from the prediction value. And, another possible reason is the geometry data of this volute at a few critical stations are not available. The author only can measure them from one drawing from the company and calculate the actual value from a scale factor. However, the error exist in this model won't affect the final conclusion.

From figure 4.11, the trend is the same as the analysis of the D3-1 case. But, we can find the adiabatic efficiency became very bad when the mass flow is higher than design mass flow (125% design mass flow). It gave us a hint that we might need a big volute for the impeller that is used in this compressor.

Since it has been proved the diffuser length and tongue position have strong influences on the performance of a centrifugal compressor at off-design conditions, the diffuser and tongue position of volute will be kept unchanged in our numerical

experiment. Because the axial position of the volute can affect the centrifugal compressor performance and the flange position limits axial position of the volute, the axial position of the volute will also be kept the same as the original volute.

Thus the method to enlarge the volute is just to enlarge the volute volume before the tongue position, at the same time the cone part was kept unchanged. Figure 3.6 shows the way how the volute volume was enlarged.

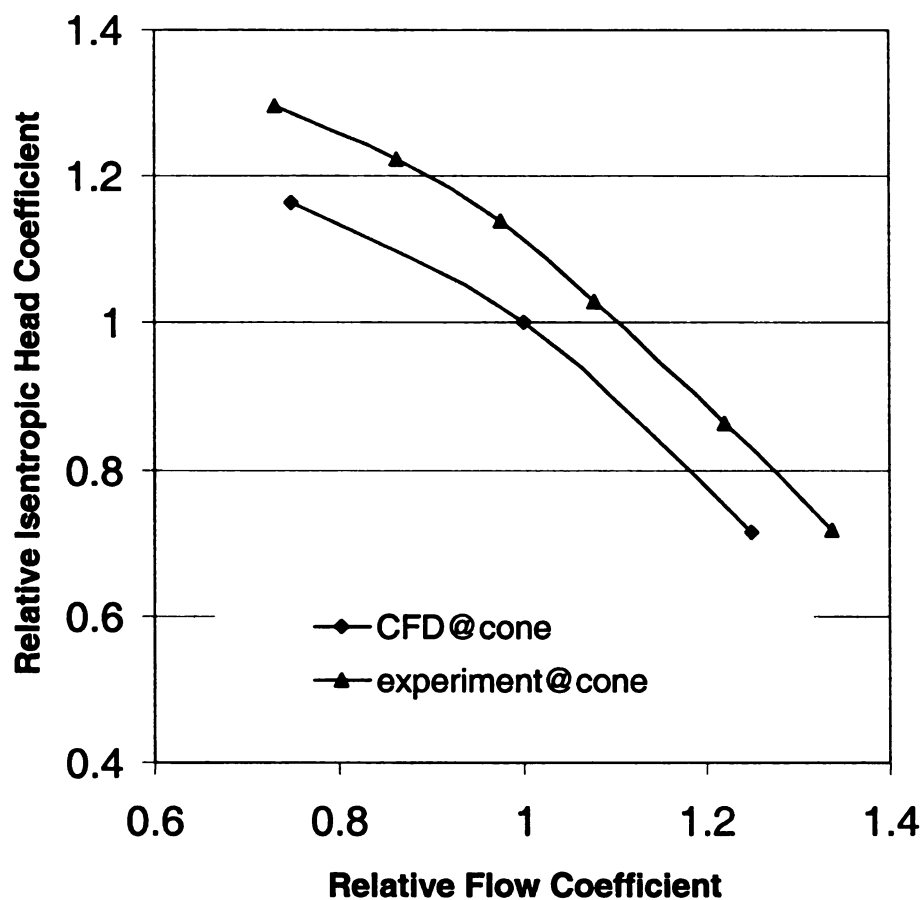


Figure 4.10 Compressor performance

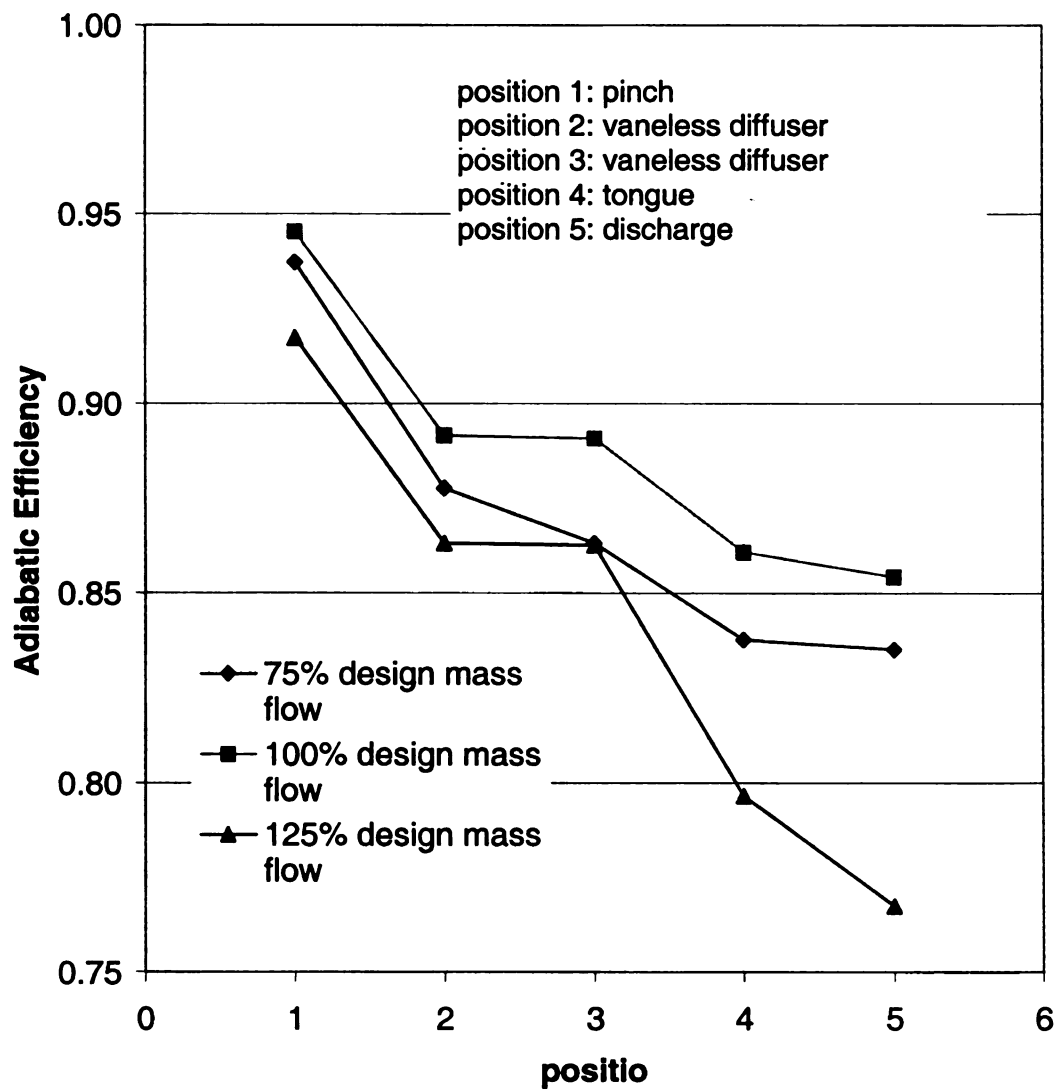


Figure 4.11 Efficiency of different stations at different mass flows

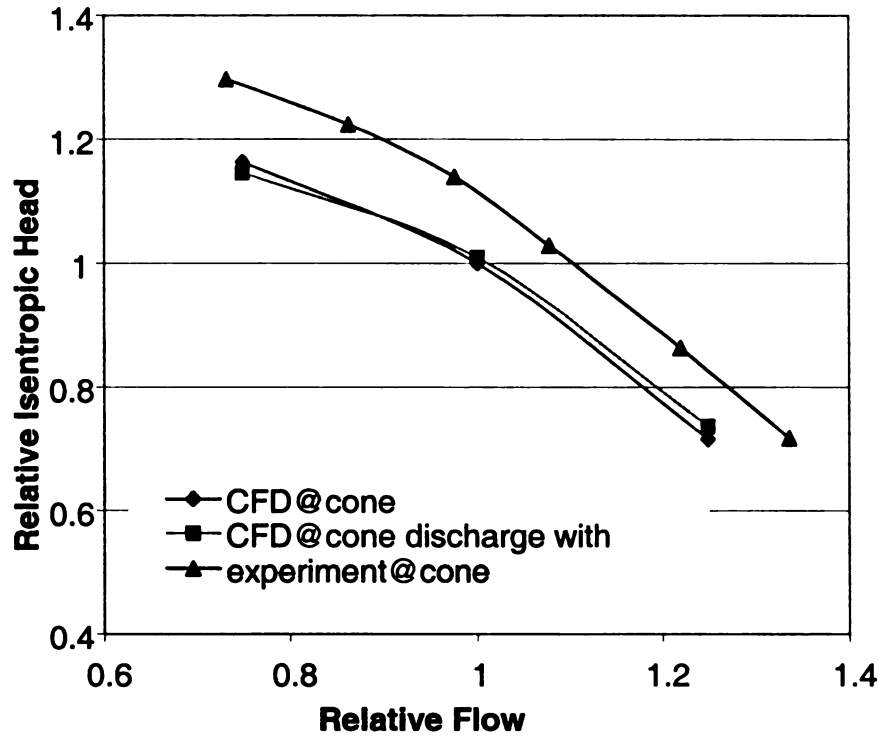


Figure 4.12 Performance comparison of the two volutes

Figure 4.12 shows the compressors performance with the enlarged volute and the original volute. From this figure, we can see that at the design and high mass flow, the isentropic head improved a little bit in the enlarged volute configuration. However, at low mass flow, this change hurt the performance a little bit.

Figure 4.13 can make this idea more clear. The efficiency is almost the same for the design and low mass flow (around 0.5% up in design mass flow and 0.5% down in low mass flow). But, at high mass flow, the efficiency increased by 3%!

Figure 4.14 and 4.15 give the total pressure and static pressure comparisons for the original volute and the enlarged volute. At design and low mass flow, the two configurations have the similar total and static pressure distributions. At high mass flow,

both the total and static pressures were improved a lot in the enlarged volute configuration.

This means that if the volute volume is enlarged without changing the tongue position, diffuser width/length and the volute axial position, a 3% efficiency gain can be expected at least at high mass flow for this volute and impeller configurations. At the same time, the compressor performance will almost keep the same as the original compressor performance at design and low mass flow.

This method indicates a way to improve the performance at high mass flow without hurting the low mass flow performance.

Conclusions

From the analysis above, quite a few conclusions can be deduced.

The integrated tool introduced in chapter 3 is very robust and reliable for the compressor performance prediction.

For this kind compressor configuration, circular volute/vaneless diffuser with backswept impeller, the diffuser stall usually occurs at the hub wall around the volute inlet station.

Volute stall usually occurs at the shroud wall near the volute inlet region at high mass flow.

Large radial velocity at the impeller outlet is the main reason for the big swirl loss in the volute.

The function to change a volute volume freely is very useful for performance improvement, especially in the beginning of a volute design.

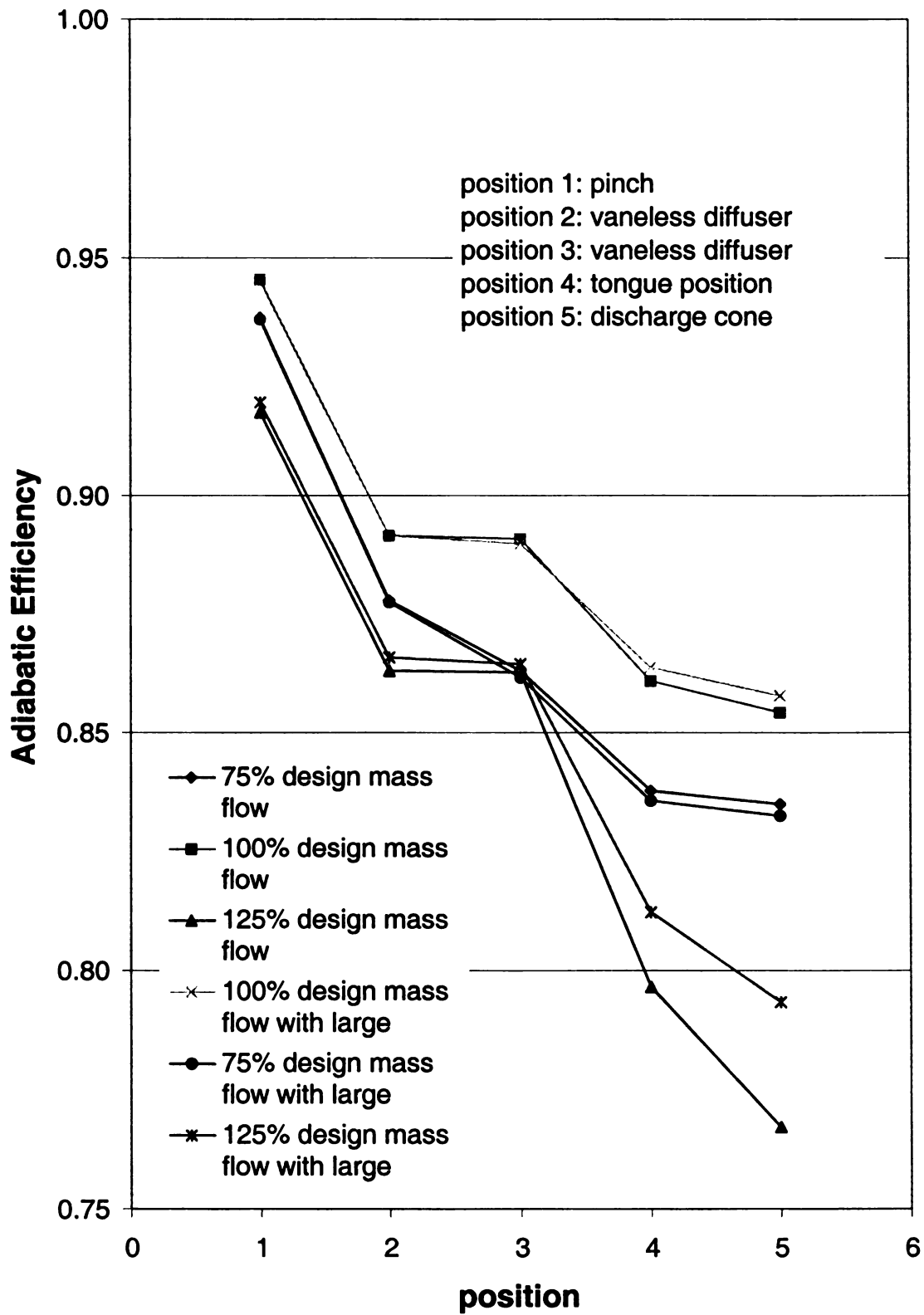


Figure 4.13 Efficiency comparison between large volute and the original one

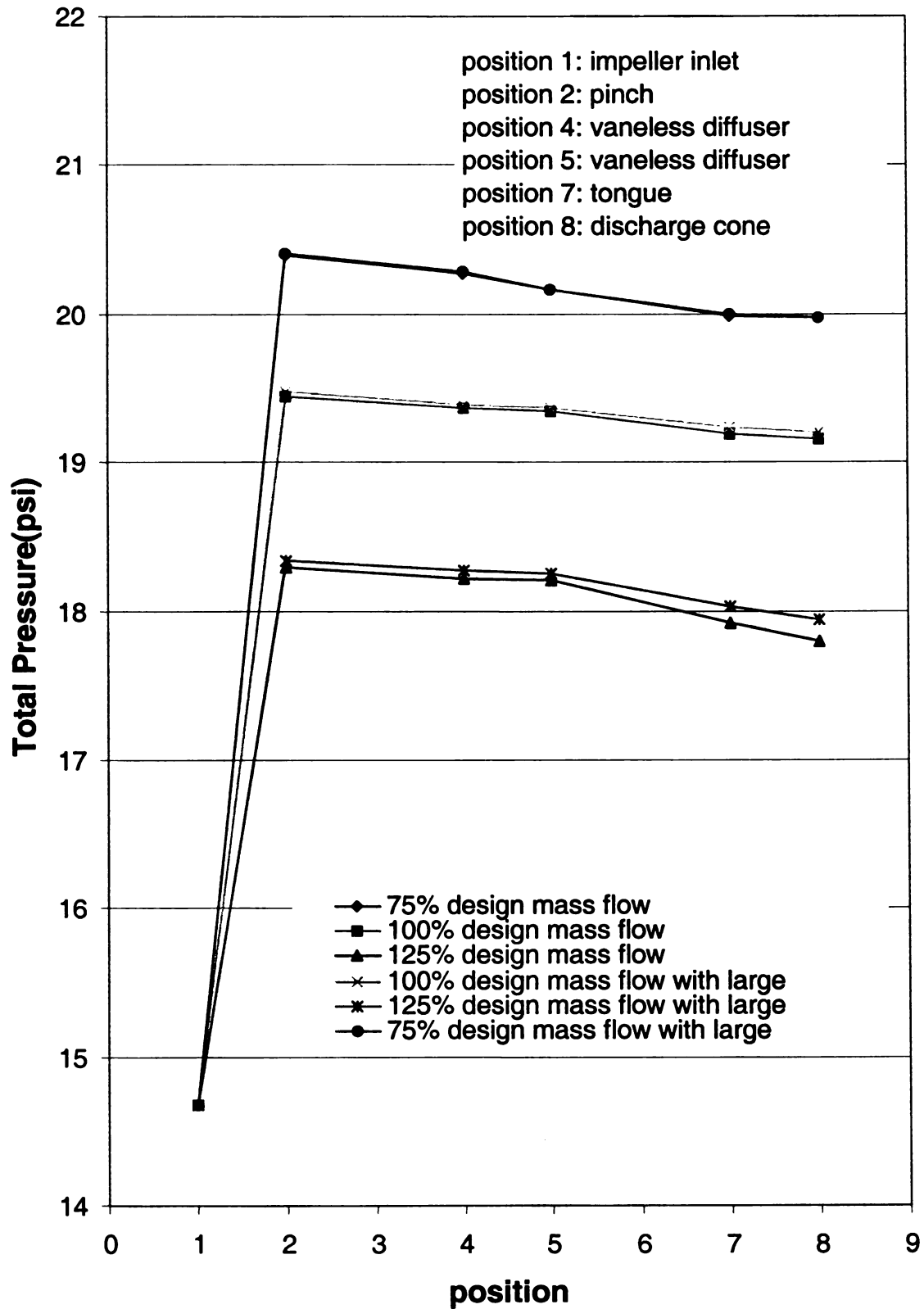


Figure 4.14 Total pressure comparison between large volute and the original one

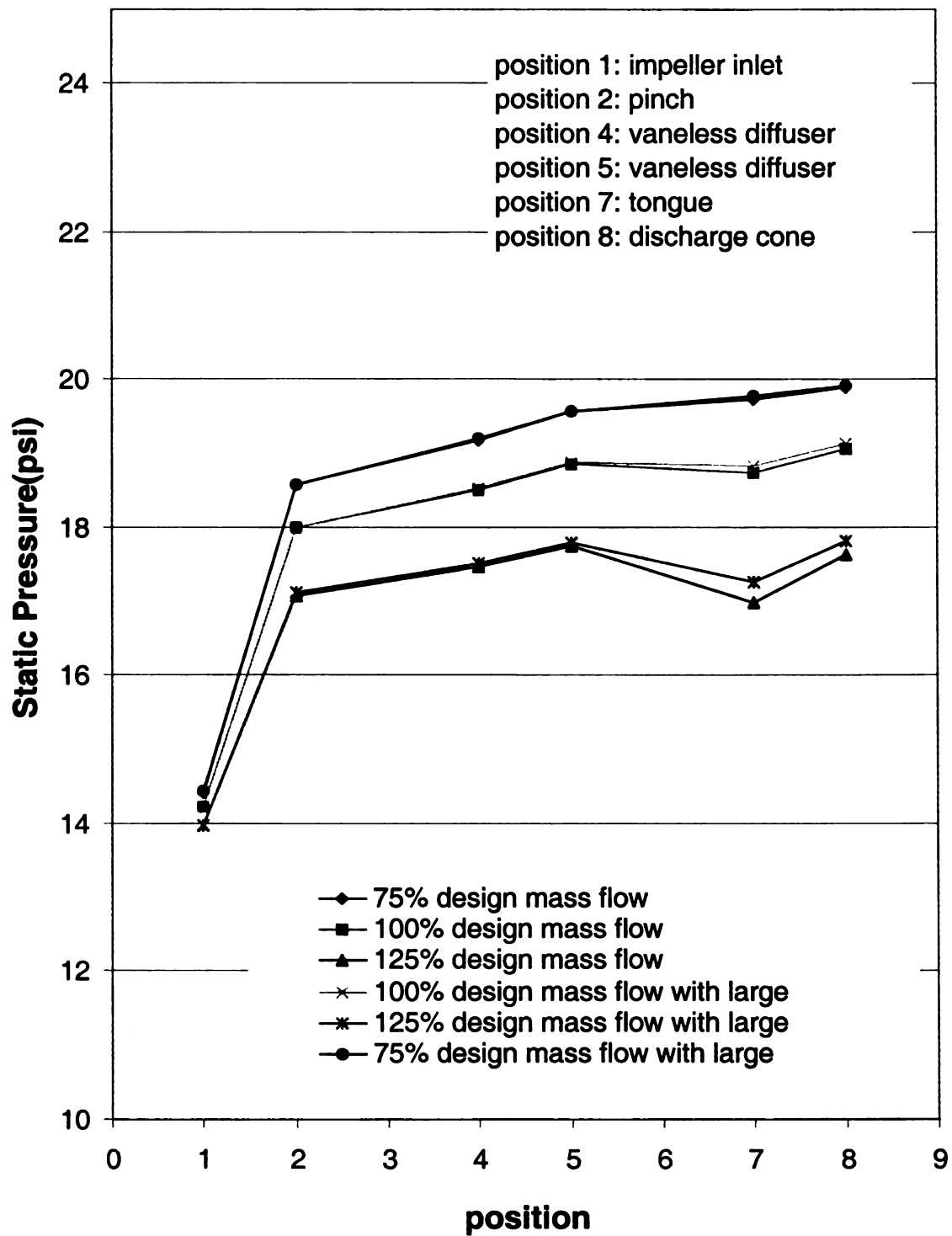


Figure 4.15 Static pressure comparison between large volute and the original one

Chapter 5

Performance investigation of two different volutes and same impeller

5.1 Introduction

Volute are widely used in industrial compressors as the transition from the impeller-diffuser to the pipelines, because of their simple structure, easy production and wide operating range. However, there are only very few documented data on internal flow measurements in volutes.

Volute, conic diffuser and sudden expansion discharge loss account for 4-6 points of efficiency decrement in a typical centrifugal compressor stage. The flow in a volute is highly complex. It is strongly believed that understanding of the detailed flow structure in a volute will provide insights on minimizing the losses by isolating the mechanisms that contributes to entropy generation. The result will be a more efficient centrifugal compressor product for customers and users and a product at higher profitability levels for manufacturers.

Lendorff and Meienberg have investigated two symmetric volutes and one overhung volute. The results indicate that the overhung volute has a better performance. Mishina and Gyobu presented a detail test results about different shape volutes in 1978. The data show a preference for circular cross section volute if the centerline diameter is not small. Fahua et al has studied the flow in overhung volute by using one passage grid of impeller to attach with a volute/diffuser grid. This paper limits the discussion to the flow axial distortion since the exit flow at impeller exit was averaged. Ayder et al. measured and simulated the elliptic cross section volute, and, compared the performance

at high, medium and low mass flow. Hagelstein et al. tested a rectangular volute at high mass flow. Euler method with a correction for friction effects is used in this paper. According to Hagelstein, this method predicts the tendency of the losses and the pressure rise, but less accurate to predict the volute performance. The unsteadiness in volute is generated by the variation of the flow at the outlet of the rotating impeller. But, the unsteadiness decreases very soon because of the rapid mixing of the blade-to-blade flow. So only a small error can be anticipated if the flow in volute is assumed to be steady (Hillewaert).

This chapter presents the experimental and numerical investigation on the performance of the two different overhung volutes with flat-top circular cross sectional area to the same centrifugal compressor impeller. The experimental data were measured from flange to flange firstly, then three Kiel probes were installed at pinch position circumferentially. At the same time, a detailed numerical simulation of the performance of the two volutes has been carried out. Two computational models, stage and frozen, using the k- ϵ turbulence model and the wall function, has been used to predict the internal flow of the both volutes. A good agreement between experimental data and numerical simulation results was found. The overall performance of the two volutes was also discussed in detail. Attention was focus on the effect of different volutes on the impeller, diffuser and the whole compressor performance, and the comparison of the two CFD simulation methods. The objective to predict the compressor performance followed by a volute through an inexpensive, fast and reliable way is achieved after the experimental data validation.

5.2 The Investigated compressors

The same impeller with two different exit components (small volute vs. large volute) is scaled from the product of the Solar Turbine, Inc. The two configurations are as follows:

The first configuration consisted of the scaled impeller with the scaled volute that was designed for this impeller at Solar Turbines, Inc. This volute will be marked as small volute.

The second configuration used the same impeller as the one in the first configuration, but another scaled volute from another compressor was used as the exit component this time. This volute will be referenced as large volute.

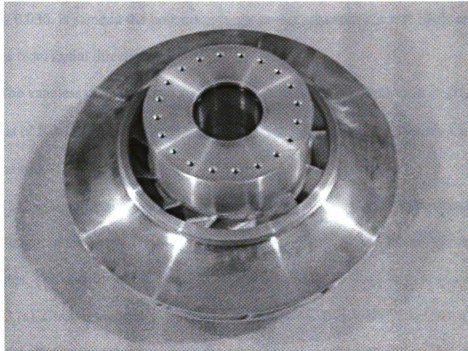


Figure 5.1 Tested impeller

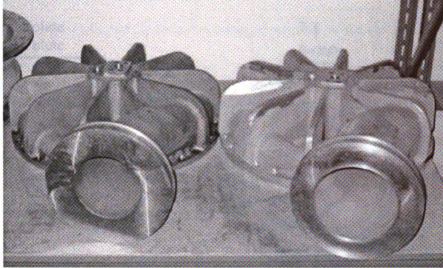


Figure 5.2 Small and large volutes

The shrouded impeller with 13 blades (figure 5.1), which the tip/diameter ratio (b_2/D_2) is 0.036, is same in the both compressor configurations. The exit blade angle is – 60 degree from radial direction.

The vaneless diffuser is pinched 40%, which means the pinch ratio (b_3/b_2) is 0.60, at a radius of $R_3=1.10 \times R_2$. The width of the vaneless diffuser is also same for the both configurations.

The large volute was generated by increasing the axial position and decreasing the diffuser length of the small volute a little bit. The figure 5.2 shows the outside view of the two volutes. The contour of the two volutes at tongue position (station 7) is shown in figure 5.3 (a). Circumferentially, the other cross-sectional area ratio of the two volutes is same as the ratio in the tongue position. For the cone part, the area ratio of the two

volute at the same axial position is 1.25. And, the circumferential angle distribution of volute and the position of station 7 and 8 can be found in figure 5.3(b).

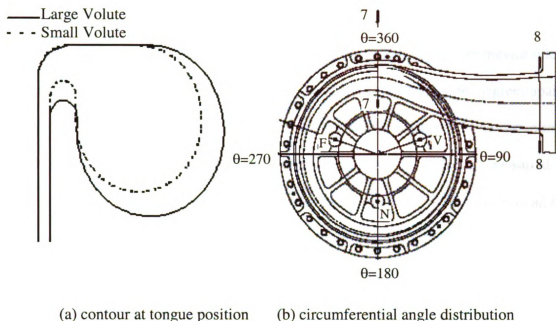


Figure 5.3 Compressor configurations

5.3 Test Facility and test procedure

The Aerotest Facility, as introduced in chapter 3, is located at Solar Turbines, Inc. Kearny Mesa Facility, San Diego, California. The test article and the closed loop piping are indoors. Air was the test gas for all the two compressor configurations. As far as the instrumentation, please reference the test report prepared by Dr. Jean-Luc Di Liberti for detail.

A bellmouth venturi located upstream of the compressor inlet flange was used to measure the flow. All pressures are referenced to ambient pressure and calibrated on line during the test. Solar Turbines, Inc. has an SCXI temperature system incorporating Type T thermocouples was used to measure temperatures. The thermocouples are calibrated

with a reference RTD and calibration coefficients are developed to provide an accuracy of $\pm 0.2^{\circ}\text{F}$ in the anticipated temperature range.

In the flange-to-flange rig tests, the compressor stage was insulated and equipped with 4 total pressures, 4 static pressures and 4 total temperatures at the compressor inlet and discharge port. At the compressor flanges, the 4 probes are located 90 degrees apart and at 4 different immersions satisfying equal areas. And, for each speed line, a minimum of eight flow set points were obtained. From the pressures and temperatures measured above, the flange-to-flange performance and components static pressure recovery can be calculated.

After completion of a flange-flange test, Kiel probes were installed at pinch position at a fixed angle and the volute backface was not insulated any more. The Kiel probes were located at three different circumferential locations (F, N and V, see figure 5.3 (b)) for the both volute configurations. So the impeller performance can be estimated from the measurement of these probes since the pinch position is only 10% downstream of the impeller tip.

A few rotation speeds, 13,100rpm, 16,030rpm, 19,240rpm, 20,640rpm and 21,865rpm, were measured for the two compressor configurations at Solar Turbines, Inc. In this paper, only the 19,240rpm rotation speed was analyzed.

5.4 Computational Method

Three-dimensional, compressible, steady flow computations were carried out, at the Michigan State University, by using the commercially available computational fluid dynamics code, CFX-TASCflow. This code solves the Reynolds averaged Navier-Stokes

equations in primitive variable form. The k- ϵ turbulence model was employed for these simulations. “Wall functions” were supplied to model the momentum and heat transfer processes for turbulent flows in the near-wall region.

The impeller grid was generated from the commercial impeller grid generator, TASCgen. TASCgrid was used to generate the volute and diffuser grid. However, all the complicated input files for this software were produced from a self-made FORTRAN code at the turbomachinery lab at Michigan State University. The volute grid is of butterfly section so as to reduce the grid skewness because a bad grid skewness might cause the converge problem (figure 3.3). The Multiple frame of reference (MFR) capability in CFX-TASCflow3D uses the “stage” and “frozen” rotor concepts. A sliding interface is implemented in such a way that steady state solutions are supported in each frame. Two flow models in the MFR frame, stage rotor and frozen rotor, were adopted for the simulation.

For stage cases, please reference to 3.1.2.1 for theory detail. For the whole compressor “stage” grid, please see figure 3.1. The basic idea for this model is that it’s assumed that all the other passages of impeller grid experience the same flow as in the impeller passage shown in the figure 3.1. And, the exit flow of the impeller is averaged circumferentially. So only one passage was modeled here and the periodic condition was defined for this impeller passage.

For frozen rotor, see 3.1.2.2, all impeller passages are simulated together. The exit flow of impeller is no longer assumed to be uniform and the flows in each passage are not assumed to be periodic either. Thus, frozen rotor analysis can be used to investigate the circumferential variation of the flow. Same as in the stage case, the transient effects at the

interface between impeller and diffuser are not modeled. Please go to figure 3.2 for the whole frozen model grid.

For each impeller passage, the grid size is 36,860 points. So the whole impeller has 479,180 points. The volute size is 145,535 points.

The inflow boundary conditions were based on the total pressure, total temperature, inflow velocity direction, turbulent eddy length scale and turbulent intensity. The mass flow was used as outlet boundary condition. Experience shows that this kind of boundary conditions are very robust in the simulations.

The calculation was considered to be converged when the nondimensionalized maximum residuals are reduced to 1.0×10^{-4} , and it was also confirmed that the final solutions were unchanged after further iterations reduced these errors to 1.0×10^{-5} or 1.0×10^{-6} .

Since the purpose of this chapter is to focus on the compressor performance, such a kind of compressor grid is fine enough (Gu). The influence of the turbulence model and the wall function used in this paper has not yet been studied.

5.5 Results and discussions

For stage case, design and 6 off-design conditions were run for each volute. For frozen case, because of time-consuming, 3 off-design conditions plus the design condition were run for each volute. The design condition was always the first point to run for each simulation. Thereafter, the result of design condition was used as the initial guess of the off-design conditions in the same model. For all the simulations, the machine mach number is 0.66.

5.5.1 Compressor Performance

The compressor performance, i.e. from impeller inlet (station 1) to cone diffuser outlet (station 8), is given in figure 5.4. Firstly, it can be seen the CFD simulation results match the experimental data very well except at high mass flow. The biggest error is in small volute that is near 10% at high mass flow. Second, as far as the head coefficient is concerned, the difference between the “stage” and “frozen” case of same volute can be neglected. Thus, the stage case is preferred if only the flange to flange performance is interested since it takes much less computer time than frozen case. Third, the CFD simulation did not incorporate the leakage flow in the labyrinth between the shroud outer wall and the machine case. Moreover, the “smooth” wall was an assumption in the simulation. So the CFD lines are always above the experimental data lines. It can also be noted, for small volute, the difference between CFD points and experimental points become bigger and bigger from low mass flow to high mass flow. But, for large volute, the difference is almost constant. Since the leakage flow is always there, this might because the surface roughness has more effect in small volute. Fourth, the small volute performance is better when the normalized flow coefficient is lower than 0.86; the profit lies on the large volute if the normalized flow coefficient is bigger than this value. The same cross-point is around 1.0 in the stage and frozen case.

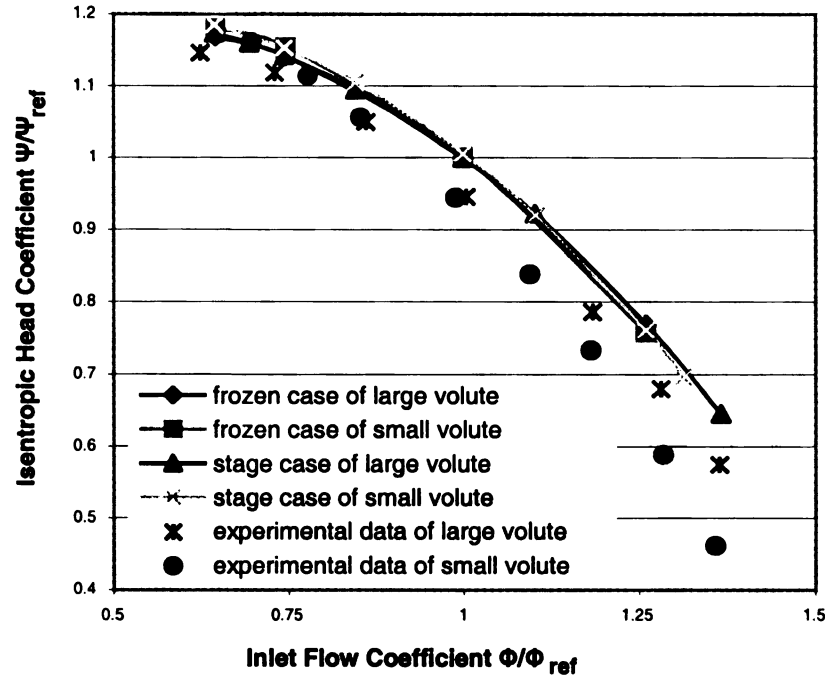


Figure 5.4 Compressor performance

The flange-to-flange (from station 1 to station 8) isentropic efficiency is presented in figure 5.5. From this figure, we can see the frozen case can predict the efficiency “trend” very well. At high mass flow, as shown in this figure, the large volute improved the efficiency significantly. At low mass flow, the harmfulness to efficiency of large volute is kind of small. For stage case, the benefit of large volute is not so obvious because the exit flow of impeller is averaged circumferentially. This figure can be used as a proof to explain how big the non-uniform circumferential pressure affects the compressor performance. Another interesting thing is the peak efficiency is almost same for both volutes. This phenomenon is very clear no matter in experiment, stage case or frozen case. The difference between the experimental data and CFD results is that the peak efficiency of small volute is at a lower mass flow than the one of large volute in experiment, but, for CFD results, they’re almost on same flow coefficient.

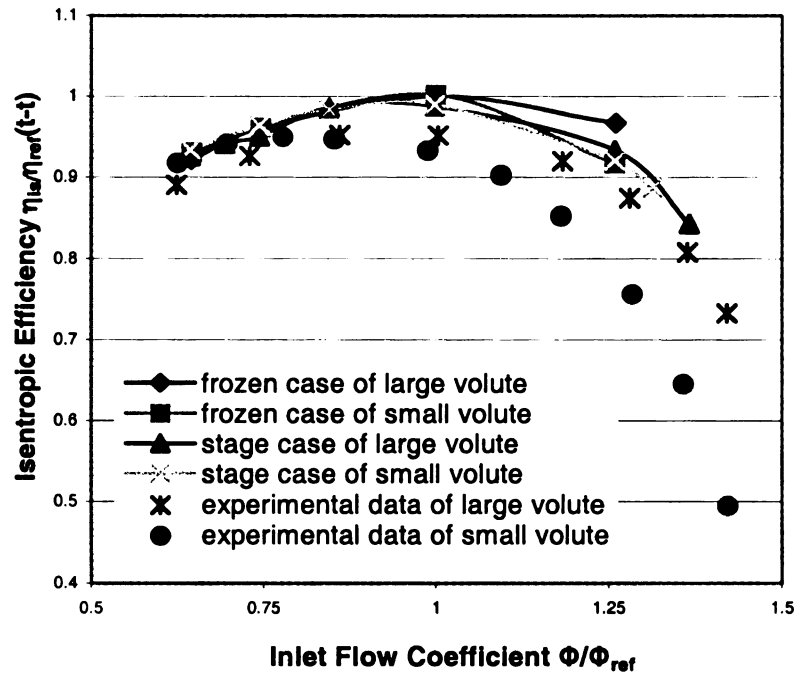


Figure 5.5 Compressor efficiency

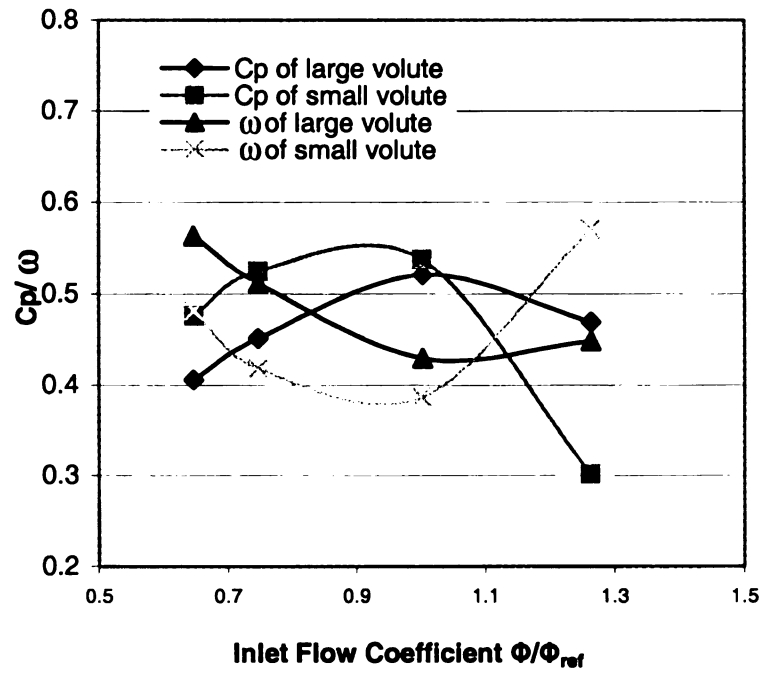
From figure 5.4 and 5.5, we can find frozen case can predict the differences existing between the two volute configurations at high mass flow although there is an almost 10% error for the small volute case at high mass flow. Stage case, no matter head or efficiency, cannot predict the differences between the two volute configurations that have been shown by experimental data. So, as far as the “trend” is concerned, the frozen case looks better. However, from accurate point, stage case is not worse than frozen case in the whole compressor performance prediction.

At Solar Turbines, Inc., the pressure recovery from diffuser outlet to volute throat at design condition was set as zero in the process of volute design. Thus in this paper the diffuser outlet was chosen as the reference station to do the pressure recovery and loss coefficient calculation. In order to get the whole idea of the compressor performance, equations (5.1) and (5.2) were used to compute the pressure recovery and loss coefficient

between station 4 and station 8 respectively. And the results are given in figure 5.6. The pressure recovery and loss coefficient between station 4 and 5 will be shown later.

$$C_p = \frac{P - P_4}{P_{04} - P_4} \quad (5.1)$$

$$\omega = \frac{P_{04} - P_0}{P_{04} - P_4} \quad (5.2)$$



(a) Frozen Case

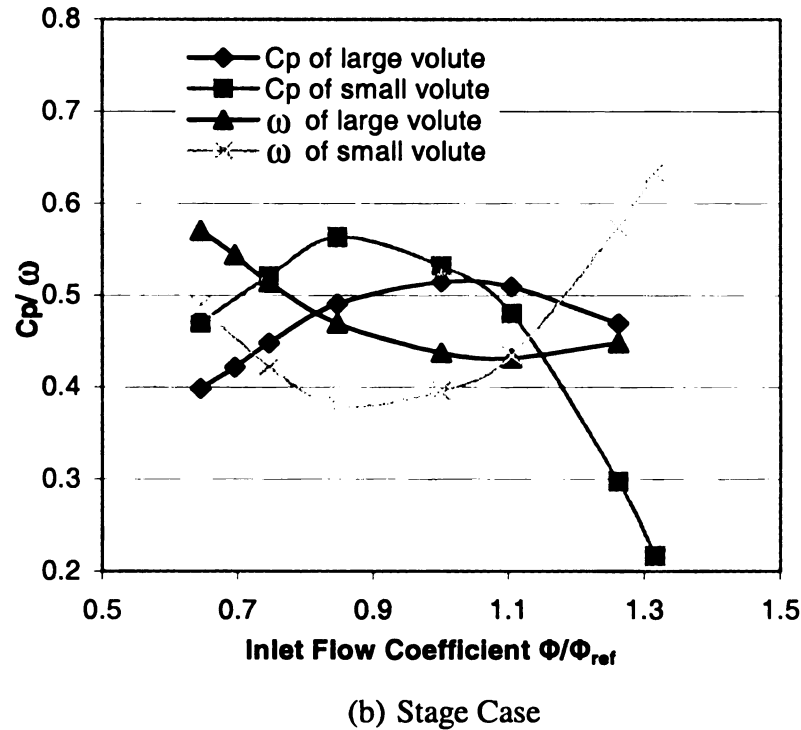


Figure 5.6 Pressure recovery and loss coefficient at exit cone

At same flow coefficient, the frozen case 5.6 (a) and stage case 5.6 (b) give same value. So we can use either map to discuss the result. When the normalized coefficient is 1.03, the pressure recovery C_p is same for both volutes. The loss coefficient ω is same when the normalized coefficient is around 1.13. When the flow coefficient is lower than 1.03, the pressure recovery C_p of large volute is lower and the loss coefficient ω of large volute is higher. But, when the normalized flow coefficient continuous decreases, the properties differences between the two volutes become smaller. When the flow coefficient is higher than 1.13, the benefit lies on large volute. Furthermore, the differences become bigger and bigger when normalized flow coefficient goes way to choke side. It means the large volute performance will be better and better when the mass flow is higher and higher. The author has the experience that enlarged volute can improve

the compressor performance at high mass flow and impair the performance at low mass flow. In figure 5.6 (a), after comparing the two points where normalized flow coefficient is 0.65 and 0.75, we can find the difference between the two volutes is a little bit smaller at 0.65 that means the performance of large volute recovered a little bit. This is more obvious in figure 5.6 (b) since more points were run for the stage cases. The biggest difference for the two volutes at low mass flow is around 0.85. At a “lower” mass flow, the recovered performance of large volute can be seen by eyeball. At low mass flow, the reason that the performance of large volute get bad first, then recovered a little bit at a “lower” mass flow is from the truncated diffuser, see figure 5.3 (a). A shorter diffuser can make the fluid particle flow path inside the vaneless diffuser shorter so as to reduce the friction loss that is the main loss in diffuser at low mass flow. From this figure, it can be found how big the effect of diffuser length on the low mass flow performance since radius ratio of the two diffuser outlets is only 1.05. The reason why the large volute performance is better and better when the flow coefficient approaches the choke side is due to the small volute volume is too small. At high mass flow, this disadvantage can produce an accelerating flow that can cause a strong non-uniformity in the volute that can propagate back to upstream. We can see this result pretty clear in later discussion.

5.5.2 Impeller and Vaneless Diffuser Performance

The performance from impeller inlet (station 1) to pinch position (station 3), shown in figure 5.7, was used as the estimation of the impeller performance in order to compare CFD results with experimental data. The experimental data were from the three

probes installed on pinch position circumferentially, where V probe is on 72 degree, N probe on 180 degree and F probe on 288 degree (see figure 5.3 (b) for the three positions). The experimental data were from the average value of these three probes. Since the pinch position is located only 10% downstream of impeller outlet, this performance is referred as impeller performance. It can be seen that the experimental data of the two volutes are pretty close except a little bit difference exists at low mass flow. The CFD results, especially the frozen case result, match the experimental data very well from surge side to choke side. The discrepancy between stage case and experimental data is bigger only when the normalized flow coefficient is around 0.75. This can be understood from the assumption of the stage case. As mentioned above, the exit flow at the impeller outlet was averaged circumferentially for stage cases. So this phenomenon (big difference between stage case and experimental data exists at low mass flow) gave us a strong hint that there is a severe circumferential pressure distortion for both volutes at low mass flow which stage case cannot catch.

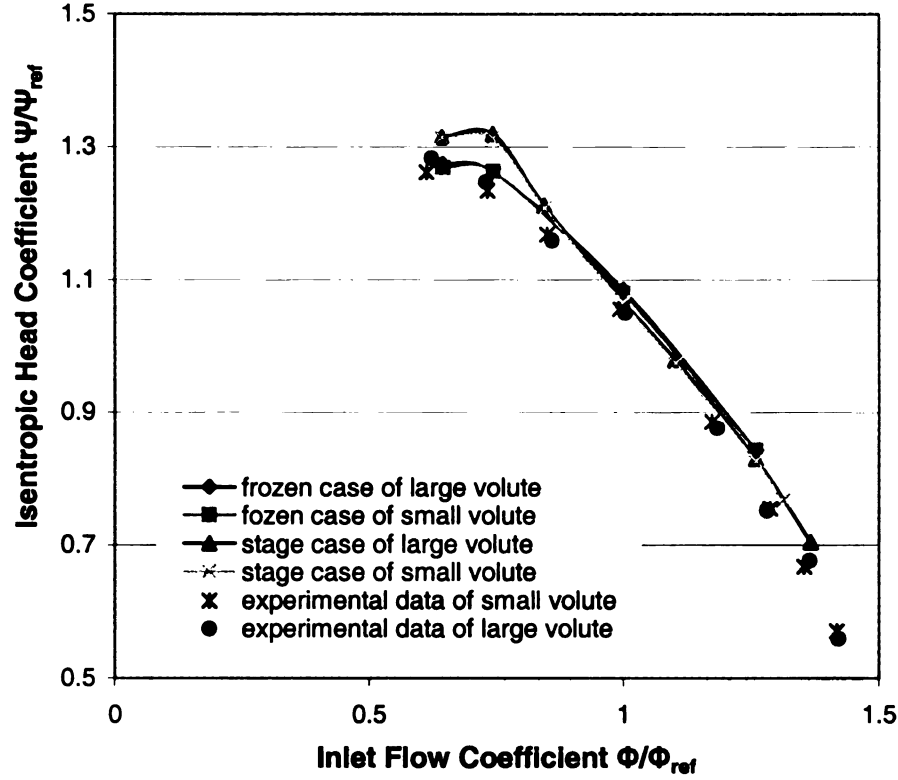
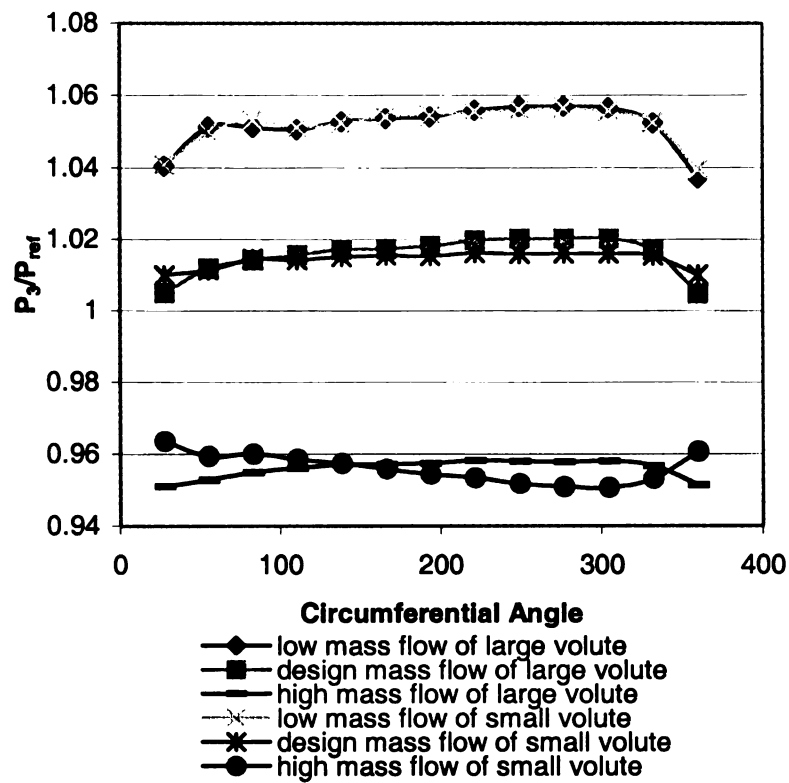


Figure 5.7 Impeller performance

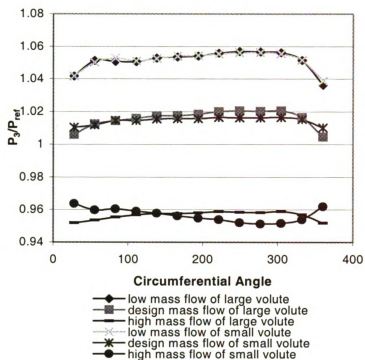
Figure 5.8 is the circumferential pressure distribution of both volute configurations at pinch position in frozen cases. All circumferential mass averaged results (b). These averaged results are based on the averaged area shown in figure 5.9. The rectangular area enclosed by thin lines along the radial direction is used for the spanwise average and the radius ratio is only 1.01. The rectangular area enclosed by thick lines along the pinch position is for the circumferential average and it only occupies 1.54 degree circumferentially. So please keep in mind that the circumferential average also includes spanwise average. The small spanwise area (along the radial direction) is exactly on one circumferential angle. However for 5.8 (b), the averaged circumferential angle of the small rectangular area along the pinch position was used for the circumferential

location. The first reason to do such a kind of circumferential average is because there is spanwise variation exists. Second, all the data are mass averaged value and there are more mass flow go through this face relative to the spanwise averaged area. What's more, the author also has interest to take a look at the results of different averaged methods. As far as what's the spanwise variation, please see the reference 3 for detail. Nowadays, it is well known that the uniform circumferential pressure distribution at impeller outlet is one design objective of turbomachinery. Here, the pinch position was selected instead of impeller outlet due to the same reason as before. It can be noticed that the figures 5.8 (a) and 5.8 (b) gave the same trend throughout the low, design and high mass flow no matter what averaged methods were used. And, no matter in 5.8 (a) and 5.8 (b), the static pressure distribution curves for two volutes have same trend at design and low mass flow. The only difference between the two mass flows is the low mass flow has more non-uniform distribution. Especially from 300 degree to 80 degree, the static pressure distortion is more severe, where is near the tongue position. This is the reason why the frozen cases have a better impeller isentropic head prediction than stage cases. Between 360 and 80 degree, the small volute has a better distribution than large volute at low mass flow. So the impeller matched with small volute has a little bit better performance than the one with large volute when the flow rate is lower. At high mass flow, the static pressure distribution has the opposite trend for large and small volute, i.e. the static pressure decreases for small volute and increases for large volute when the azimuth angle is less than 300 degree, and increases for small volute and decreases for large volute between 300 and 360 degree. And, the large volute has a flatter curve than the small

volute has at high mass flow. If compare the high and low mass flow, it also can be found that the pressure distortion level is more severe at low mass flow.



(a) spanwise average



(b) circumferential average

Figure 5.8 Circumferential static pressure distribution at pinch position

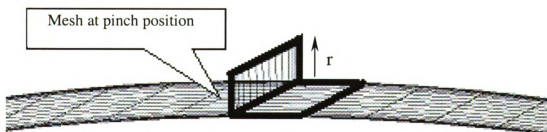


Figure 5.9 Spanwise and circumferential averaged area

The circumferential static pressure distribution at vaneless diffuser outlet is given in figure 5.10. Just like the phenomenon at impeller outlet, at low and design mass flow the large and small volute almost have same static pressure distribution from 30 degree to 300 degree. Near tongue position, i.e. from 300 degree to 360 degree, the large volute shows a little better distribution. This tendency is more obvious at high mass flow at the tongue position where the static pressure in large volute is 181% higher than the one in small volute.

According to common sense, the fluid left the impeller outlet will follow a logarithm spiral path. But, compare figure 5.8 and 5.10, we didn't find the range of pressure distortion enlarged, shrunk or shifted when the pressure distortion propagated from diffuser outlet to pinch position. It needs to be investigated further whether or not this phenomenon is from the use of a narrower diffuser, computational model or something else.

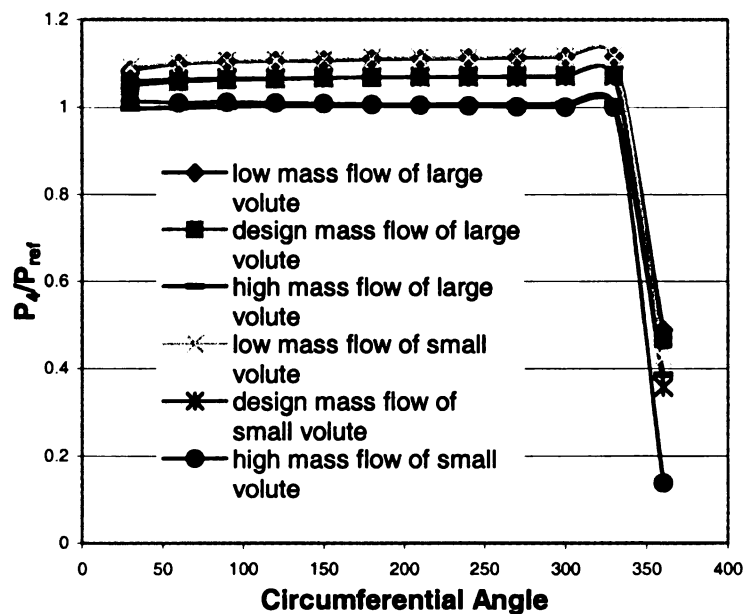
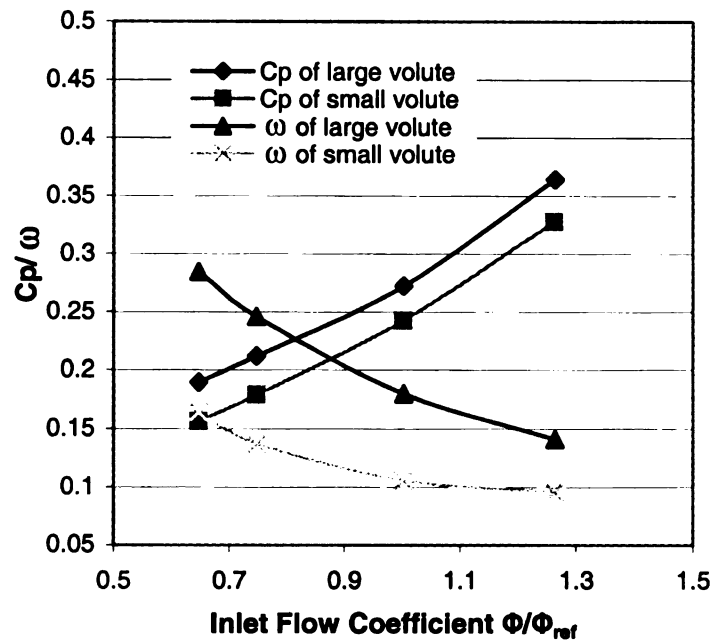


Figure 5.10 Static pressure distribution at vaneless diffuser outlet

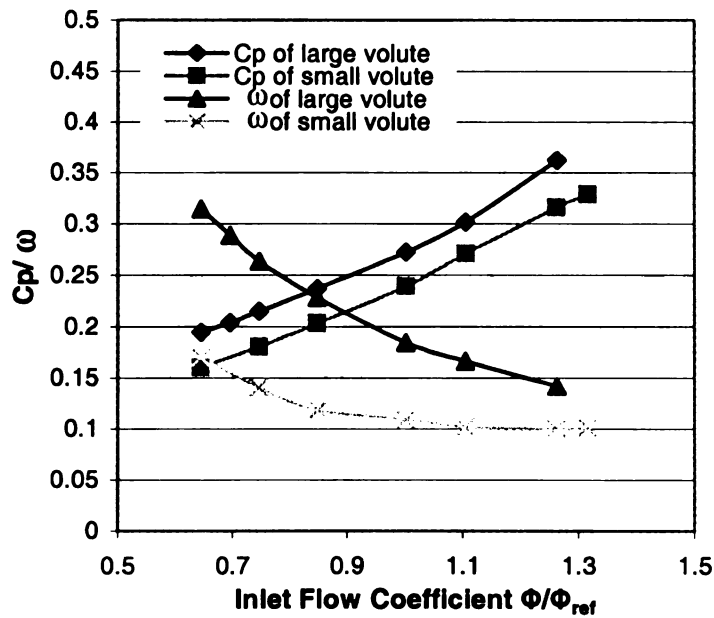
5.5.3 Volute Performance

As mentioned above, the pressure recovery between diffuser outlet and volute throat was chosen as zero at the design mass flow in the volute design process. The flow properties at the diffuser outlet (station 4) and volute throat (station 5) are circumferential (360 degree) mass averaged, and tongue position (station 7) is radial mass averaged. Again pressure recovery and loss coefficient relative to station 4 were calculated by using the equation (5.1) and (5.2). The results are shown in figure 5.11 and 5.12 respectively.

As show in figure 5.11, the pressure recovery increases and loss coefficient decreases in both volutes when flow coefficient becomes bigger. The difference between loss coefficients of the two volutes at surge side is kind of bigger. At the choke side, the difference become smaller and smaller. Accordingly, the differences between the pressure recoveries of the two volutes become bigger at choke side from (b) since stage case has more points. This means the enlarged throat of the large volute make a detriment on surge side, but benefit on choke side. In both volutes, the design criterion of zero pressure recovery coefficients at the beginning of volute design is not satisfied. Anyway, both volutes exhibit a desired performance at throat position.

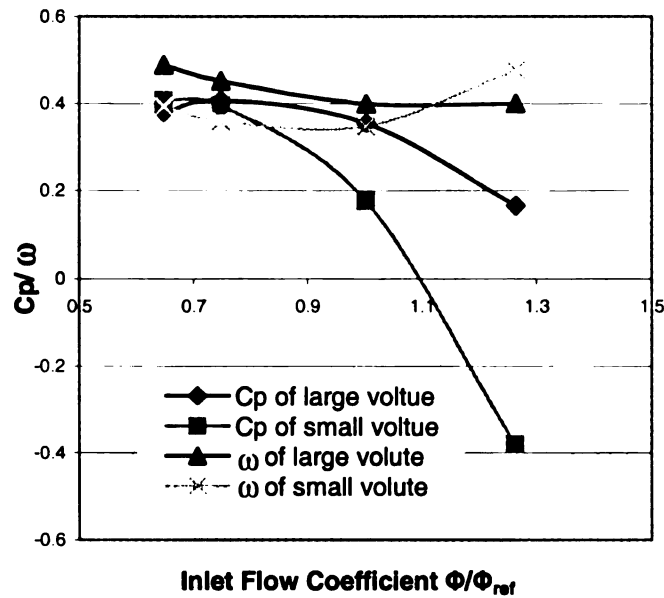


(a) Frozen Case

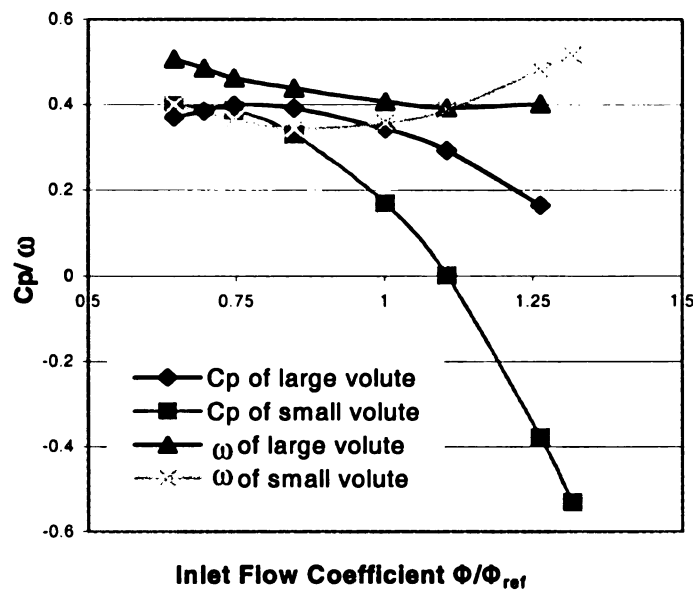


(a) Stage Case

Figure 5.11 Pressure recovery and loss coefficient at volute throat



(a) Frozen Case



(b) Stage Case

Figure 5.12 Pressure recovery and loss coefficient at tongue position

The pressure recovery coefficient and the loss coefficient at station 7 relative to station 4 are shown in figure 5.12. We can see in this part the performance get worse. The

loss coefficient is very high. And, pressure recovery coefficient goes down continuously for both volutes. Especially for small volute at high mass flow, the loss coefficient goes up dramatically and pressure recovery coefficient goes down to negative when the normalized flow coefficient is large than 1.1. When mass flow is less than design mass flow (around 1.0), the performance of the large volute at tongue position is even much better than the performance of small volute. So, great attention should be focus on this “performance neck” —tongue position—in volute design.

The circumferential static pressure in volutes is also calculated by using mass averaged method. The results are given in figure 5.13. We can see the large volute and small volute match each other very well at design and low mass flow except only some differences exist near tongue position. At high mass flow, the static pressure in small volute always goes way down throughout the flow. But, large volute presents a desired performance. It seems the small volute volume can only accelerate the fluid in it. So it leads a pressure drop that is the source of non-uniform pressure distribution at diffuser outlet and pinch position. This proves the theory in Ayder et al paper.

Compare figure 5.10 and 5.13, we can find that the static pressure distribution at diffuser outlet and in volute can be completely different. The volute acts back on diffuser outlet only through the volute throat. So future research is urgently needed on the throat radial position, angle and size.

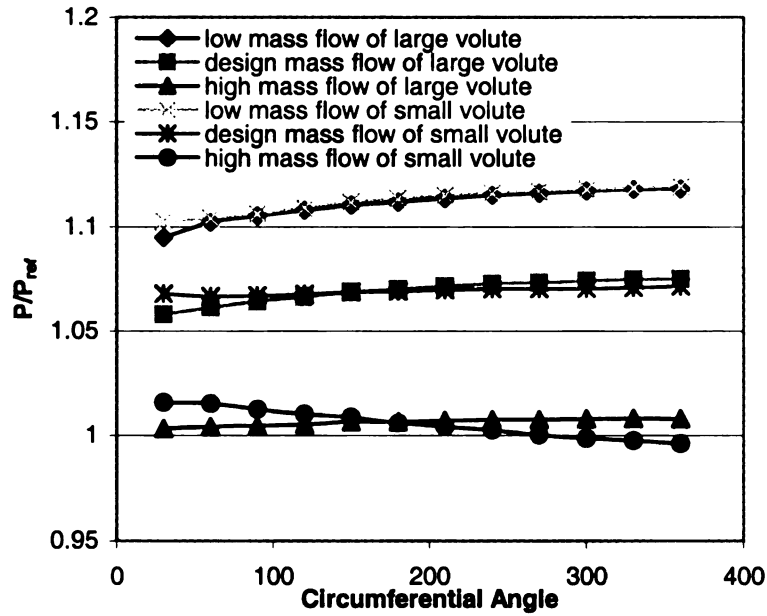


Figure 5.13 Static pressure distribution in volutes

Conclusions

Two volutes with same impeller are investigated by using frozen case and stage case in this paper. The CFD results have been compared with the experimental data.

- From the analysis above, it has been shown the results of frozen and stage method in CFD code “TASCflow” match the experimental data very well except for the whole compressor performance at high mass flow. And, only frozen case can predict the performance difference exists at high mass flow for the both volute configurations.
- For impeller performance, frozen method is preferred because of the assumption of stage case. For the same reason, frozen method should be

selected if the circumferential distortion downstream of impeller outlet is interested.

- The large volute almost has the same maximum efficiency as the small volute has. From experiment data, the peak efficiency for different volutes lies in different flow coefficient. But, CFD results didn't catch this characteristic.
- The volute volume plays an important role in compressor performance at high mass flow. If combined with an improved diffuser, a little bit shorter diffuser used here, large volute won't impair the performance much at low mass flow.
- The zero pressure recovery from diffuser outlet to volute throat in the volute design was not satisfied; and an enlarged throat is benefit for the static pressure distribution at vaneless diffuser outlet at high mass flow.
- No pressure distortion shift was found between pinch position and diffuser outlet by the two computational models.
- For small volute, the performance is very bad at tongue position at off-design condition. A large volute improves the performance at tongue position even at lower mass flow than design point.

Future work of the two configurations should be focused on the effect of the volute throat part and tongue position on the whole compressor, the impeller/volute interaction, and the flow structures inside the impellers, diffusers and volutes.

Chapter 6

Flow Structures Investigation and Comparison

6.1 Introduction

Volute is an important component whose function is to collect the flow from the periphery of the diffuser and deliver it to the outlet pipe. Even in low-speed compressor and pump applications where simplicity and low cost count for more than efficiency, it is the diffuser not the volute that can be omitted. Nowadays, one popular design objective for volute is to achieve a uniform pressure distribution at the volute inlet because the circumferential distortion that occurs inside the volutes would propagate back to upstream and cause flow fluctuation among impellers. This would make the efficiency drop of the whole machine.

Recently, the study on volute/impeller interaction caught more and more interest. T. Elholm, et al. investigated the three-dimensional velocity distributions in two different cross sections of a pump volute by means of LDV. He found that the leakage flows in the tongue region could increase or decrease the flow in the volute and therefore influence the circumferential pressure distribution. Ayder, et al. showed by measurement that the variations of the total and static pressure distribution at the different volute cross sections and at the vaneless diffuser exit in a centrifugal compressor with a volute of elliptic cross sections. The centrifugal forces due to the swirl velocity in the volute cross section was believed to have more influence on the static pressure distribution. Hillewaert, et al.

simulated a volute/impeller interaction by an unsteady flow calculation in the impeller and a time-averaged flow calculation in the volute. There is no average total pressure reduction found in his calculation method that was explained as no mix out in the diffuser, contrarily to the rapid mixing at the impeller exit. Fahua, et al. has studied the flow in overhung volute by using one passage grid of an impeller to attach with a diffuser grid. This paper limits the discussion to the flow axial distortion since the exit flow at impeller exit was averaged. Thus, this paper investigated the volute/diffuser interaction axially only. Fatsis, et al. suggested using the acoustic Strouhal number to quantify the relative effects of the rotation and pressure wave propagation in order to decide whether or not the flow in volute can be modeled as a steady flow. According to the suggestion in this paper, the pressure wave propagation in the two compressor configurations investigated here is much faster than the rotation of the impeller. That means the pressure perturbation finishes traveling over the passage at almost the same time as when the impeller moves to a new position. Thus, the steady model can be used to study the pressure distortion due to the volute.

The performance prediction and CFD/TEST data comparison of same impeller with two different volutes have been done in chapter 5. So there is no performance comparison in detail in this chapter. In this chapter, the interaction of the impeller with the two overhung volutes and the flow structures in the two compressor configurations would be investigated by using the CFD result from the “frozen rotor” because no circumferential averages were made in this model. The k- ϵ turbulence model and the wall function built in this model were used to predict the internal flow of both the volutes. The reliability of the model has been validated in the last chapter, too. For the study presented

in this chapter, attention was focused on the effect of volute tongue, volume and cross section channel curves on the impeller and the compressor performance, especially at off design condition. The research has been divided into two parts. Firstly, this chapter concentrates mainly on the effect of volute tongue on different impeller passages. The second part of this chapter describes the flow structure in the parts of volute that makes the differences in the two different volutes.

It's better to emphasize that the large volute was generated by increasing the cross-sectional area of the small volute through increasing the axial position of the small volute.

An experimental test of the performance of the two configurations was carried out at Solar Turbines Inc. A good agreement between experimental data and numerical simulation results was found and shown in chapter 5.

Corresponding improvements for volute design based on the CFD analysis in this chapter and the test data were also presented.

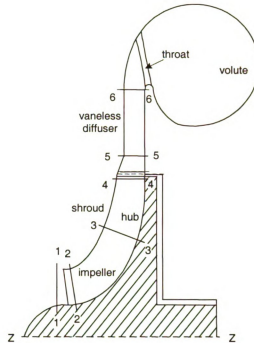


Figure 6.1 Compressor Configurations

6.2 Compressor Geometry and Computational Method

The geometries of the two compressors have been introduced in chapter 5. However, there are four new stations that were added in the wheel, which has 13 blades, namely, station 1, 2, 3 and 4 (see figure 6.1). Therefore, the flow field among the blades can be investigated in detail. Note: the nomenclature in this chapter is a little bit different from the ones used in previous chapters. In this chapter, the station 4 is near the impeller tip, station 5 at pinch position, and station 6 at the vaneless diffuser outlet. The large volute was generated mainly by increasing the axial position and decreasing the diffuser

length a little bit of the small volute. The tongue position of both the compressor configurations starts at zero azimuth angle. The contour of the two volutes at tongue position (station 7) is shown in figure 6.2 again because here volute wall has been divided into four parts to facilitate the later description. There is no clear dividing points between the different walls (for example, between the outer wall and the shroud wall). These wall concepts are only qualitative. One thing need to be mentioned is circumferentially the other cross-sectional area ratio of the two volutes is the same as the ratio in the tongue position. For the cone part, the area ratio of the two volutes at the same axial position is 1.25, the differences between the two configurations are that the large volute has a larger volume and bigger throat. The vaneless diffuser length is just a little bit shorter; the radius ratio of the two vaneless diffuser outlets is 1.05.

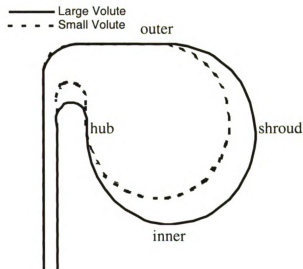


Figure 6.2 Volute geometry at station 7

The impeller grid was generated from the commercial impeller grid generator, TASCgen. TASCgrid was used to generate the volute and diffuser grids. The volute grid consists only of butterfly sections so as to reduce the grid skewness because small grid

angles can make the convergence difficult. A sliding interface between impeller and diffuser grid is implemented in such a way that steady state solutions are supported in each frame. There is no need to keep the impeller grid number and shape the same as the diffuser grid number and shape at the connection interface.

All impeller passage grids, diffuser grids and volute grids have been shown in figure 3.2. The exit flow of impeller can be non-uniform and the flows in each impeller passage are not assumed to be periodic. Thus, this analysis method can be used to investigate the circumferential variation of the flow. The transient effects at the interface between the impellers and the volutes weren't taken into account in this model.

For each impeller passage, the grid size is 36,860 points. So the whole impeller has 479,180 points. The size of volute and diffuser is 145,535 points.

The inflow boundary conditions were based on the total pressure, total temperature, inflow velocity direction, turbulent eddy length scale and turbulent intensity. The mass flow was used as the outlet boundary condition. Experience shows that this kind of boundary conditions are very robust in the simulations.

These calculations was considered to be converged when the nondimensionalized maximum residuals are reduced to 1.0×10^{-4} , and it was also confirmed the final solutions were unchanged after further iterations reduced these errors to 1.0×10^{-5} or 1.0×10^{-6} .

6.3 Test Facility and Experimental Method

The Aerotest Facility is located at Solar Turbines, Inc. Kearny Mesa Facility, San Diego, California. The test article and the closed loop piping are indoors. Air was the test gas for all tests. The compressor stage was insulated and equipped with four total

pressures, four static pressures and four total temperatures at the compressor inlet and discharge port in order to determine the machines head, efficiency and flow. After completion of the flange-flange test, Kiel probes were installed at pinch position at a fixed angle and the volute backface was not insulated any more. The Kiel probes were located at three different circumferential locations (V, N, and F in figure 5.3 (b)) for both the volute configurations, which means the impeller performance can be estimated from the measurement of these probes since the R_5 is only 1.1 times of the R_4 . Flow enters through an inlet guide vanes (IGV's). The IGV deswirled the inlet flow and provides flow with zero swirl to the impeller eye.

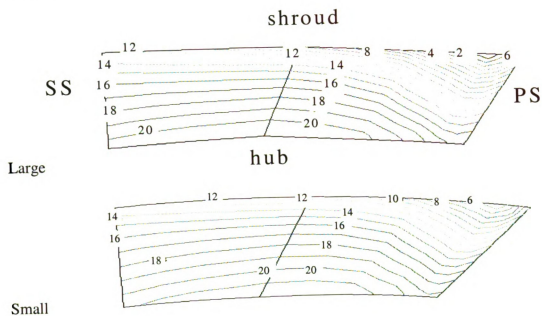
As far as detailed test instruments and test procedure, please reference chapter 5 for detail.

6.4 Results and discussion

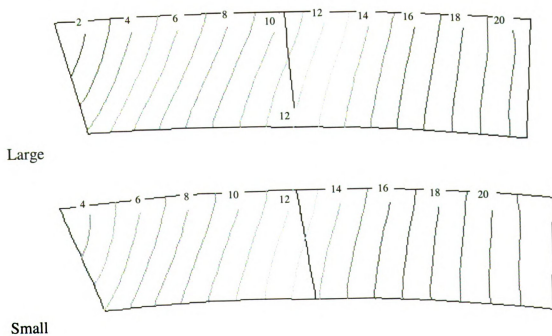
For both the configurations, design and three off-design conditions have been run by using the “frozen rotor” model when the machine Mach number is 0.66. In this chapter, only the 75% design mass flow and 125% design mass flow conditions were taken out as the representation of the low mass flow and high mass flow. And, the discussion begins from the impeller analysis, and then go through the vaneless diffuser, ends at volute structure investigation.

Flow Analysis in Impeller:

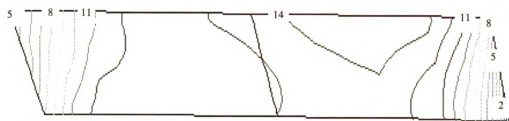
Station 2:



Station 3:



Station 4:



Large



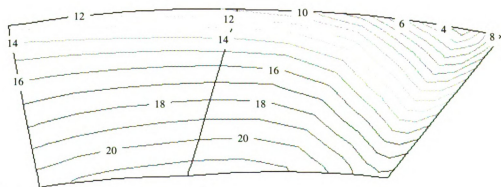
Small

Large Volute

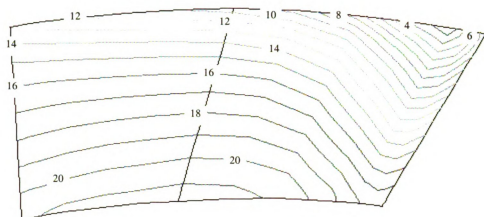
Small Volute

(a) Nearest to the tongue

Station 2:

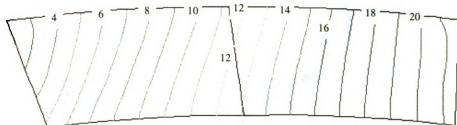


Large

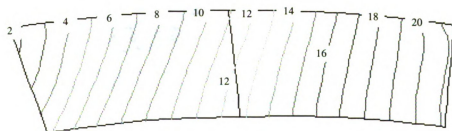


Small

Station 3:



Large

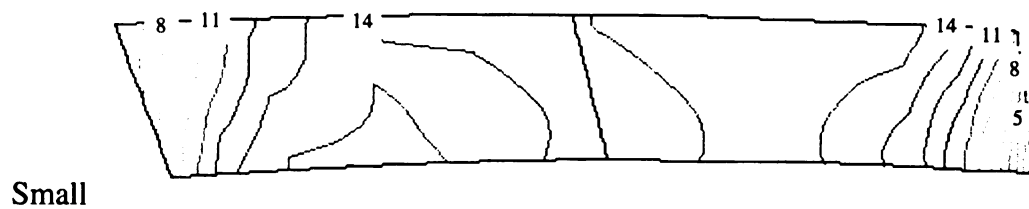


Small

Station 4:

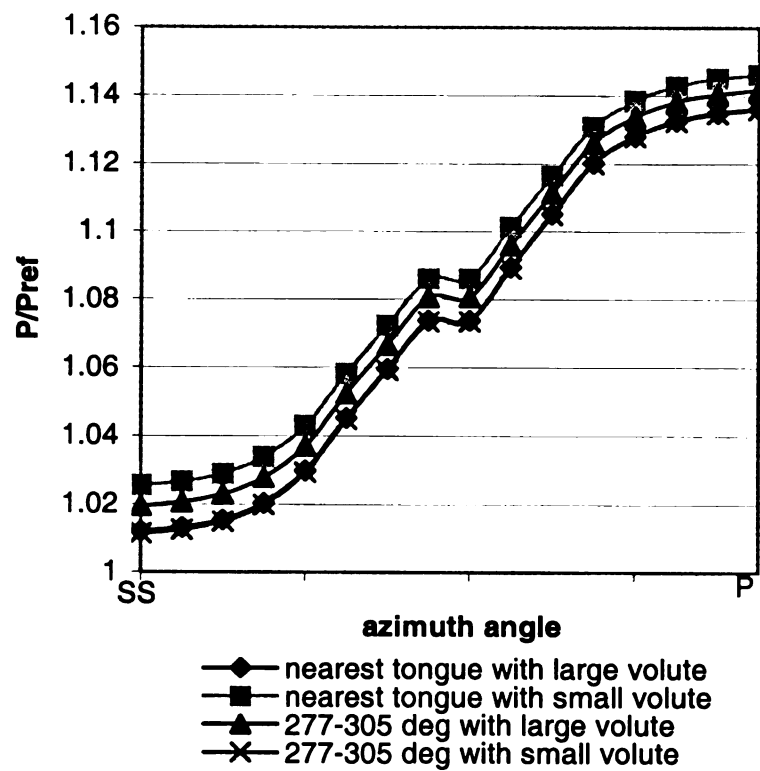


Large

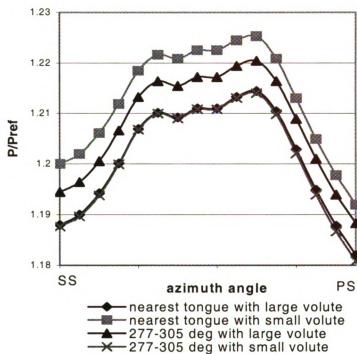


(b) Farthest away from the tongue

Figure 6.3 Static pressure at high mass flow



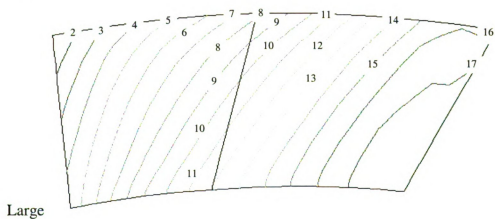
(a) station 3

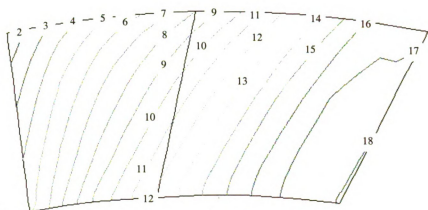


(b) station 4

Figure 6.4 Midspan static pressure distribution at high mass flow

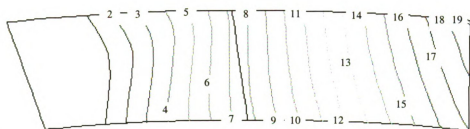
Station 2:



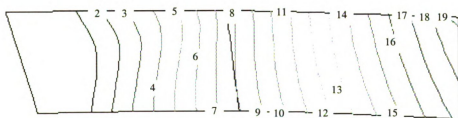


Small

Station 3:

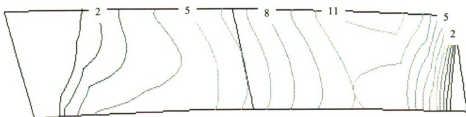


Large

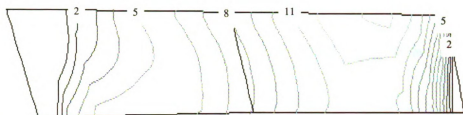


Small

Station 4:



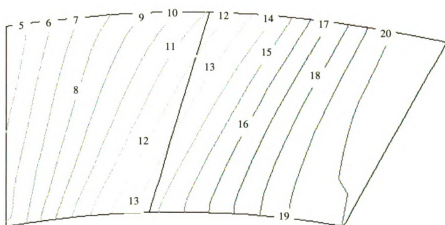
Large



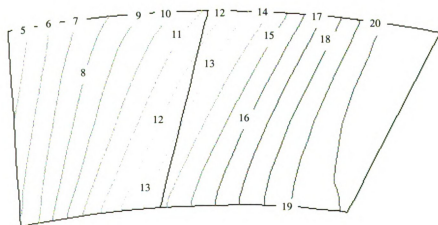
Small

(a) Nearest to the tongue

Station 2:

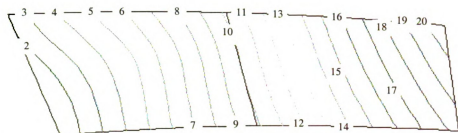


Large

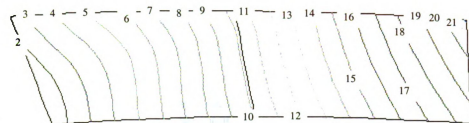


Small

Station 3:



Large

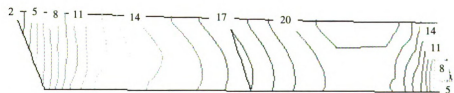


Small

Station 4:



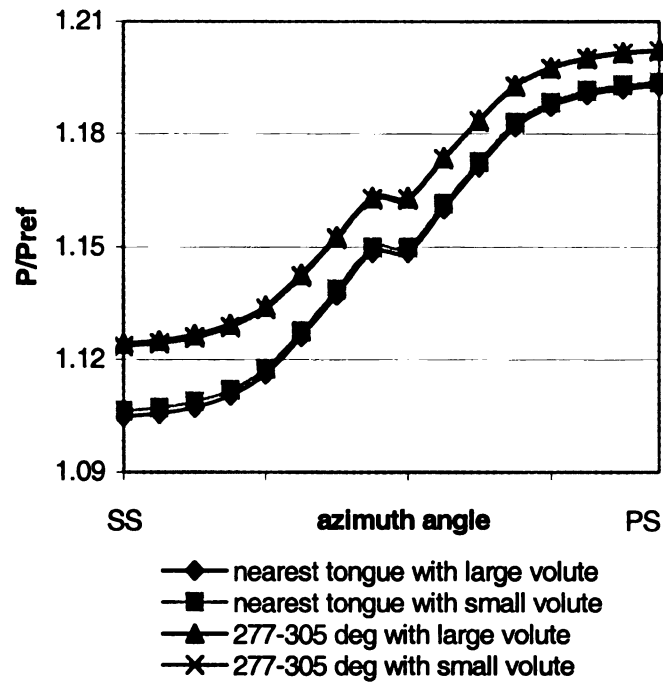
Large



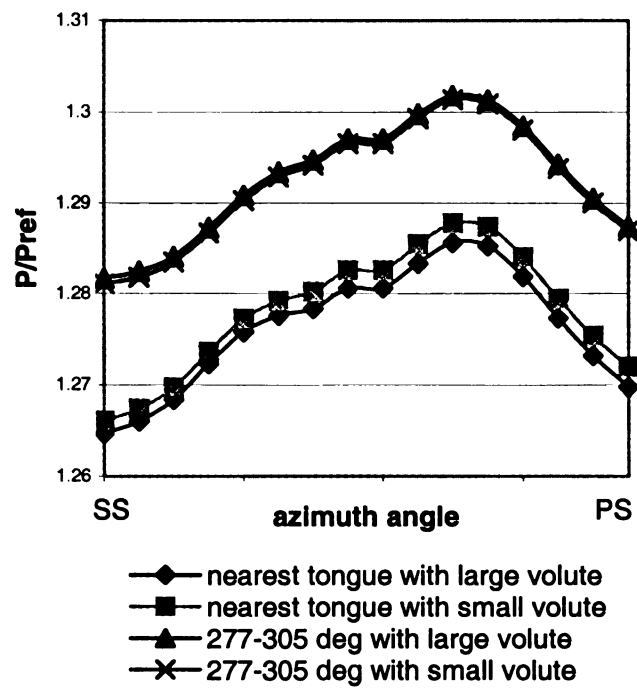
Small

(b) Farthest away from the tongue

Figure 6.5 Static pressure at low mass flow



(a) station 3



(b) station 4

Figure 6.6 Midspan static pressure distribution at low mass flow

Figure 6.3 represents the static pressure distribution among the impellers at high mass flow, the part (a) is nearest to the tongue and part (b) is farthest from the tongue. All the four sides have been marked in the first figure at station 2 in figure 6.3 (a), where “large” means in large volute configuration, and “small” means small volute configuration. All the other stations have the exact same border definition as in this station. So they are not tagged any more.

For both volutes, they exhibit similar trends at the three stations. The static pressure at station 2 nearest to the tongue region (Fig. 6.3 (a)) shows a gradient in the shroud-to-hub direction due to the high centrifugal acceleration at large mass flow. At this station the pressure on the suction side is higher than on the pressure side. So the impeller has a negative loading on the leading edge at high mass flow. And the low-pressure region is also located at the shroud/pressure-side corner. At station 3, the pressure gradient is no longer shroud-to-hub. Moreover, blade loading becomes positive at this station, and the low-pressure region changes to shroud/suction-side corner. At station 4, the pressure exhibits an almost symmetry distribution. The low-pressure region is on both shroud/suction-side and hub/pressure-side corner.

However, except the same trend shown above, there are also some differences exist between the two compressor configurations. Regardless to which station, at the same location, the pressure in the large volute is lower than the pressure in the small volute. The largest adverse pressure gradient of the static pressure between station 2 and 3, or between 3 and 4 is on the shroud/pressure-side corner and hub/suction-side when fluid flows from station 2 to 3. This pressure gradient is more than two times than other

corners at least. This pressure rise occurs as the fluid turns through the bend while reducing the relative velocity.

The flow field among blades farthest from the tongue at high mass flow was shown in figure 6.3 (b). It can be seen the impeller also has a negative loading at station 2 and the pressure gradient also becomes pressure-to-suction direction at station 3 and 4. However, it can be found that the two volutes exhibit almost same trend and same magnitude in all three of the stations. That's means the tongue effect can be neglected around this location.

Since the pressure gradient is pressure-to-suction side at station 3 and 4, the midspan pressure distributions at these two stations should be representative of the field pressure distribution among blades. Because of too many lines (13 lines among 13 blades), only two lines, minimum and maximum pressure curves, are shown in figure 6.4 for each configuration. All the other pressure distribution curves fall into this range limited by the two extreme curves. For large volute configuration, the minimum pressure distribution between neighbor blades is nearest to the tongue position; the maximum pressure distribution is between 277 degrees and 305 degrees. For small volute, the phenomenon reversed, the maximum pressure distribution is nearest to the tongue position; the minimum pressure distribution is between 277 degrees and 305 degrees. The minimum pressure distributions for both configurations are nearly the same. The discrepancy between maximum curves becomes bigger when the flow goes way to impeller exit from station 3 to 4. Also, the small volute configuration has a wider pressure distribution range that means a more non-uniform pressure distribution circumferentially. Thus at high mass flow, the tongue position gives rise to a more severe

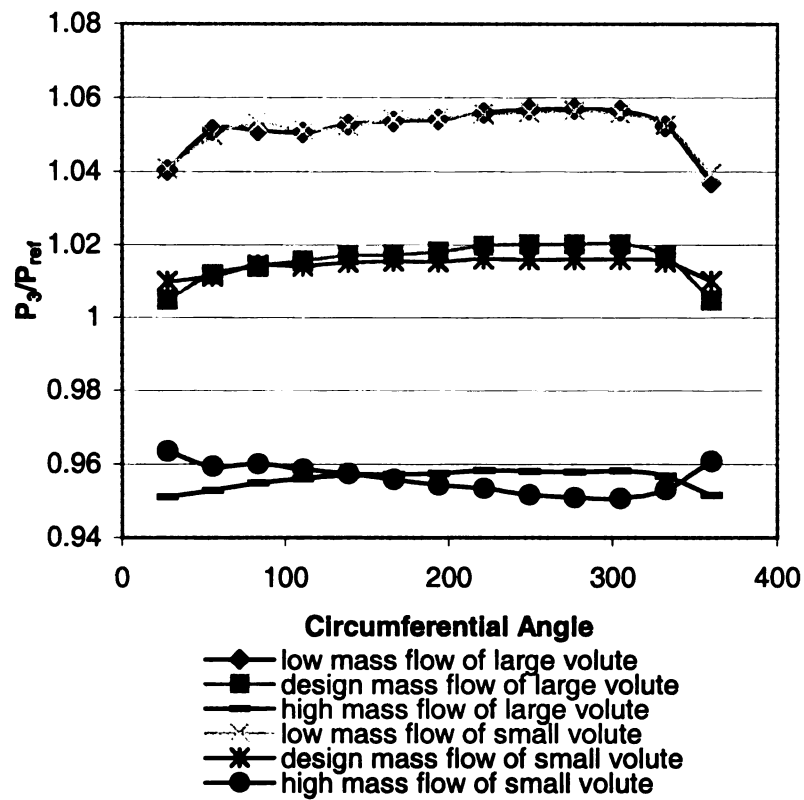
pressure distortion among impellers in small volute configuration. And, one extreme is always nearest the tongue position; another extreme is always around 290 degrees (i.e. upstream of the tongue). This means that the minimum pressure at high mass flow is not always located upstream of the tongue as Hagelstein et al. pointed. The position (minimum pressure) also depends on the volute volume and throat because those two factors are the only differences exist between the two investigated compressors. It's well known nowadays that the circumferential distortion among blades is caused by the distortion in volute. Therefore this problem will be discussed in the upcoming volute part section.

At low mass flow, the static pressure gradient at station 2 is not shroud-to-hub direction any more (figure 6.5) throughout the impeller flows. At station 3 and 4, the tendencies are the same as the one at high mass flow. Far away from the tongue, both configurations exhibit almost same pressure distribution. Nearest to the tongue position, the tendency is the same, but the pressure in impeller with large volute is a little bit smaller than the pressure in impeller with small volute at same position.

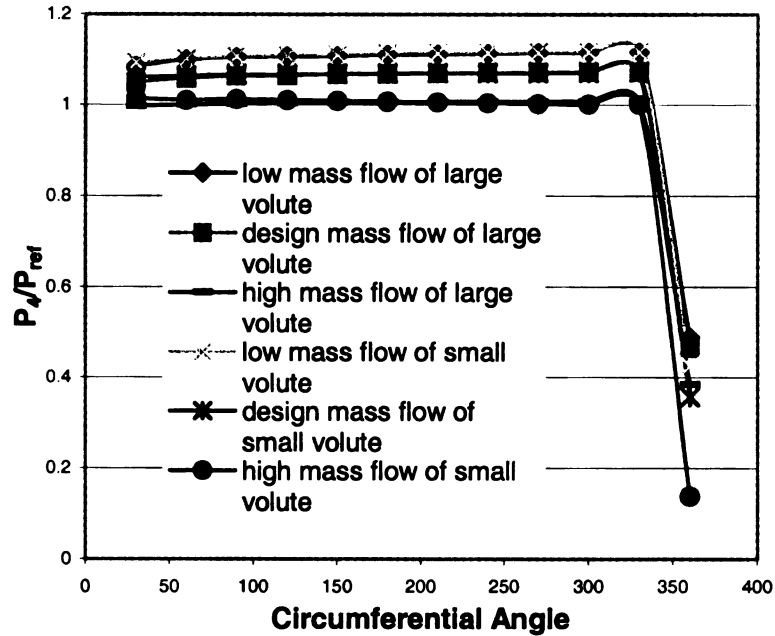
Figure 6.6 shows the midspan pressure distribution at station 3 and 4 at low mass flow based on the same reason mentioned above. It can be seen the minimum pressure distribution is nearest to the tongue position for both volutes this time. Also, for both volutes, the maximum pressure distribution is between 277 degree and 305 degree. From the figure 6.6 (b), it can be seen the small volute cause less severe pressure distortion among the blades because the range between maximum and minimum pressure is smaller at low mass flow.

From a comparison of figures 6.4 and 6.6, it can be concluded that the distortion in different impeller passages at low mass flow is more severe than the distortion at high mass flow.

Flow analysis in vaneless diffuser



(a) At pinch position



(b) At vaneless diffuser outlet

Figure 6.7 Circumferential static pressure distribution

Figure 6.7 is a mass averaged pressure value distribution at the pinch position and at the diffuser outlet. The most severe pressure distortion is between 270 and 360 degrees. In the figure 6.7 (a), it can be found that the trend for both volutes at low mass flow is the same and the trend is opposite at high mass flow. Especially at high mass flow, from 270 degrees to 360 degrees, the range of pressure change is consistent with the trend among impellers (fig. 6.4 (b)). So from the pinch station to the stations inside the impellers, no pressure distortion shift is found although circumferential pressure distribution inside the impellers is more non-uniform. Just like the phenomenon at the pinch position, at low and design mass flow, the large and small volute almost have the same static pressure distribution when the azimuth angle is less than 270 degrees at the diffuser outlet. Near

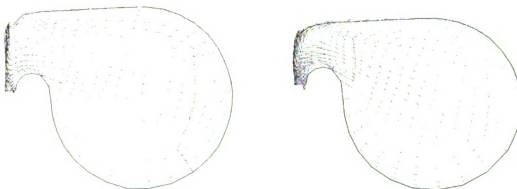
tongue position, i.e. from 270 to 360 degrees, the large volute shows a little better pressure distribution. This tendency is more obvious at high mass flow at the tongue position where the static pressure in the large volute is 181% higher than the pressure in the small volute. Again, the position with severe distortion is the same at the pinch and among the impellers. No phase shift can be found by the frozen case.

Flow structure in volutes:

270 degrees



357 degrees



(a) Large volute

(b) small volute

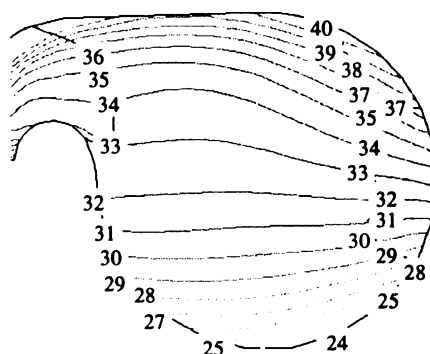
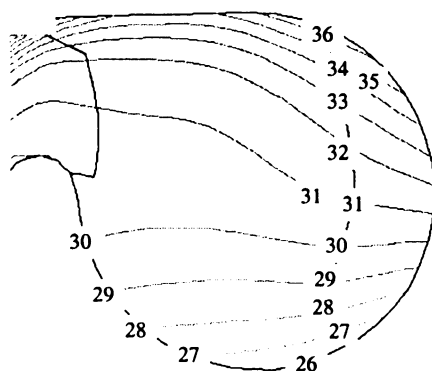
Figure 6.8 Volute flow patterns at low mass flow

It is well known that the swirling flow exists over all the sections of volute. Gu, et al. indicates that the high energy loss at high mass flow is because of the existence of a twin vortex downstream of the tongue which is induced by the low radial velocity at the shroud side; at low mass flow the high loss is from the recirculation upstream of the tongue that is because the fluid at the hub side cannot exit the volute. According to the impeller analysis, the zone between the blades that is affected most by volute is from 277 to 360 degrees. Thus the comparison of the swirling flow of the two volutes at low mass flow in this range is shown in figure 6.8 first. Ayder, et al. shows that the second flow exists in the inner-hub wall corner in their rectangular volute. Here the volute cross-sections between 270 and 357 degrees are selected to show in figures. At low mass flow the twin vortex exists at 357 degrees (upstream, not downstream of the tongue) in both the volutes. And the position is around the interface of the inner-shroud wall. At 270 degrees, the twin vortex occurs only in the large volute, not in the small volute. No twin vortex flow is found for either volute at high mass flow (didn't shown here) because of the large radial velocity at volute inlet. This proves that the twin vortex is not relative to how big the mass flow is (Gu, et al. found twin vortex at high mass flow). It strongly depends on the flow structure in the volute that is affected by the volute channel curvature and the leak flow around the tongue.

Figures 6.9 and 6.10 show the static and total pressure distributions in the same cross-sections at low mass flow respectively. The pressure in the large volute ranges from numbers 26 to 36 at 270 degrees; number 33 to 37 at 357 degrees. The distribution is more uniform than the distribution in the small volute that is from number 24 to 40 at 270 degrees and from numbers 34 to 40 at 357 degrees. From a comparison of the two volutes

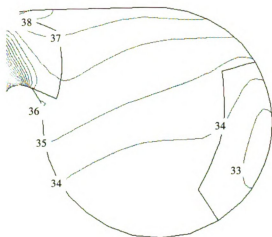
at 270 degrees, it can be found that the pressure gradient is bigger in the small volute. This is because the sharp cross-section curvature of the volute is “strong” enough to make a pressure gradient that is distributed in the inner-outer wall direction. This is helpful to suppress the secondary flow—twin vortex. Around the tongue, i.e. at 357 degrees, neither volute curvature can keep this pressure gradient. This is the reason why the twin vortex occurs from the shroud-inner wall interface. So it should be a good idea to change the large volute cross section curvature from 270 degrees according the small volute shape to get better performance at low mass flow since no twin vortex occurs in the small volute at high mass flow. It will be harmless to high flow performance by this improvement. From the analysis above, it is not hard to understand the reason why the total pressure in the large volute is lower than the total pressure in the small volute at low mass flow.

270 Degrees

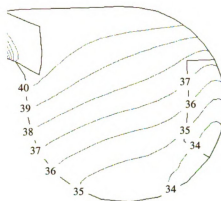


	P/Pref
40	1.3952
38	1.3933
36	1.3923
34	1.3914
32	1.3904
30	1.3895
28	1.3876
26	1.3866
24	1.3856
22	1.3847
20	1.3837
18	1.3828
16	1.3809
14	1.3799
12	1.3789
10	1.3780
8	1.3770
6	1.3751
4	1.3742
2	1.3732
1	1.3722

357 Degrees



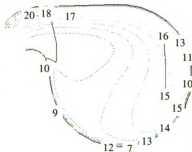
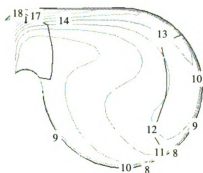
(a) Large Volute



(b) Small Volute

Figure 6.9 Static pressure at low mass flow

270 Degrees



PT/PTref

30	1.3889
28	1.3843
27	1.3824
25	1.3778
24	1.3759
22	1.3722
21	1.3694
19	1.3657
18	1.3639
16	1.3593
15	1.3574
14	1.3556
12	1.3509
11	1.3491
9	1.3444
8	1.3426
6	1.3389
5	1.3361
3	1.3324
2	1.3306
1	1.3287

357 Degrees

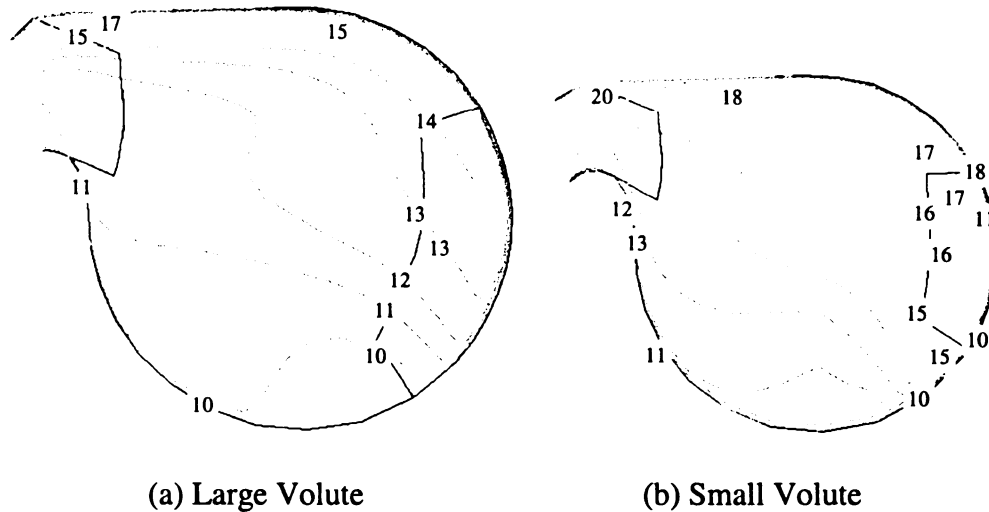


Figure 6.10 Total pressure at low mass flow

Conclusions

This chapter has investigated the flows inside impellers, diffusers and volutes in detail. The frozen method build in CFD code TASCFlow was the tool to do the study. A few conclusions based on the analysis in this chapter are as follows,

No distortion position shift from the vaneless diffuser outlet to fluid interior the blades was found by using the steady state frozen method.

At high mass flow, negative blade loading was found in the blade leading edge.

The distortion in different impeller passages at low mass flow is more severe than the distortion at high mass flow. Same phenomenon can be found at the pinch position.

At high mass flow, the large volute throat benefits the performance more.

For flat-top circular overhung volute, the secondary flow usually starts from the inner-shroud interface. And, the secondary flow strongly depends on the volute channel curvature and the leak flow around the tongue. This phenomenon can occur either at low mass flow or at high mass flow.

The twin vortex flow can occur not only at downstream of the tongue as a few papers indicated, but also at upstream of the tongue. A sharp curvature can help to eliminate this phenomenon in volute. At high mass flow, no twin vortex was found in volute, however, as the analysis in chapter 4, it will give rise the volute stall around the volute inlet region.

BIBLIOGRAPHY

1. Ayder, E., Van den Braembussche, 1991, "Experimental Study of the Swirling Flow in the Internal Volute of a Centrifugal Compressor", International Gas Turbine and Aeroengine Congress and Exposition, Orlando, FL June 3-6, 1991
2. Ayder, E., 1993, "Experimental and Numerical Analysis of the Flow in Centrifugal Compressor and Pump volutes," Dissertation of Von Karman Institute.
3. Ayder, E., Van den Braembussche, R. and Brasz, J. J. 1993, "Experimental and Theoretical Analysis of the Flow in a Centrifugal Compressor Volute," ASME Journal of Tribomachinery, Vol. 115, pp. 582-589
4. Ayder, E. and Van den Braembussche, R., 1994, "Numerical Analysis of the Three-dimensional Swirling Flow in Centrifugal Compressor Volute", ASME Journal of Tribomachinery, Vol. 116, pp. 462-468
5. Baun O. Daniel, Kostner Lutz and Flack D. Ronald, 2000, "Effect of Relative Impeller-to-Volute Position on Hydraulic Efficiency and Static Radial Force Distribution in a Circular Volute Centrifugal Pump", ASME, Journal of Fluids Engineering, Vol. 122, pp. 598-605
6. Biheller, H.J.(1965), "Radial force on the impeller of centrifugal pumps with volute, semivolute and fully concentric casing", ASME J. Engnr for Power, Vol. 87, No. 3, July 1965, pp 319-323
7. Binder, R.C., Knapp, R.T. (1936), "Experimental determination of the flow characteristics in the volutes of centrifugal pumps", ASME Trans., Vol. 58, Nov. 1936, pp649-663
8. Bowermann, R., Acosta, A. (1957), "Effect of the volute on performance of a centrifugal pump impeller", ASME Trans., Vol. 79, No. 5, 1957, pp 1057-1069
9. Brown, W.B., Bradshaw, G.R. (1947), "Design and performance family of diffusing scrolls with mixed flow impeller and vaneless diffuser", NACA TR 936, 1947
10. Brownel, R.B., Flack, R.D. (1984), "Flow characteristics in the volute and tongue region of a centrifugal pump", ASME Paper 84-GT-82
11. Carter, D. (1981), "A finite element analysis of ideal flow in a centrifugal pump volute", M.S. Thesis, University of Virginia, May 1981

12. Copley, D.M., Worster, R. C., Zanker, K.J. (1962), "The flow in a pump volutes and its effect on performance", BHRA SP 724, 8th Conf. On Hydromechanics, April 1962
13. Csanady, G.T. (1962), "Radial forces in a pump impeller caused by a volute casing", ASME J. Engnr for Power, Vol. 84, No. 4, Oct. 1962, pp 337-340
14. Dick, E., Ammi, M. (1991), "Comparison between steady and unsteady one dimensional performance analysis methods for centrifugal pumps", Eruopean Journal M. Vol. 36, No. 3, pp 177-186
15. Elholm, T. (1989), "Experimental study of volute flow in a radial pump", VKI PR 1989-21
16. Escudier, M., 1979, "Estimation of Pressure Loss in Ring Type Exit Chambers," ASME Journal of Fluids Engineering , Vol. 101, pp. 511-516
17. Fatsis, A, Pierret, S. and Van den Braembussche R. A., 1997, "Three-Dimensional Unsteady Flow and Forces in Centrifugal Impellers with Circumferential Distortion of the outlet Static Pressure," ASME Journal of Turbomachinery, Vol. 119, pp. 94-102
18. Gu, F., and Engeda, A., Mike Cave and Jean-Luc Di Liberti, 2001, "A Numerical Investigation on the Volute/Diffuser Interaction Due to the Axial Distortion at the Impeller Exit", ASME, Journal of Fluids Engineering, Vol. 123, pp. 475-483
19. Gu. F., 2000, "Design and Flow Analysis of Volutes for Centrifugal Compressors", Dissertation of Michigan State University
20. Hagelstein, D., Hasemann, H., Keiper, R. and Rautenbeg, M. 2000, "Comparison of Flow Field and Performance of Internal and External Volutes for Centrifugal Compressors," JSME 2000-GT
21. Hagelstein, D., Hillewaert, K., Van den Braembussche, Engeda, A., Keiper, R. and Rautenberg, M., 2000, "Experimental and Numerical Investigation of the Flow in a Centrifugal Compressor Volute", ASME Journal of Turbomachinery, Vol. 122 pp. 22-31
22. Hande, B. A. (1985), "Study of the flow in centrifugal compressor exit collectors", VKI PR 1985-16
23. Hira, D.S., Vasandani, V.P. (1975), "Influence of volute tongue length and angle on the pump performance", J. Inst. Of Engnrs India, Part M.E., Vol. 56, 1975, p 55-59

24. Hillewaert, K. and Van den Braembussche, R. A., 1999, "Numerical Simulation of Impeller-Volute Interaction in Centrifugal Compressors," ASME Journal of Turbomachinery, Vol. 121, pp. 603-608
25. Howard, J.H.G., Abramian M., Herman, P. (1987), "Experimental investigation of impeller and volute flow fields for a low specific speed pump with single and double volutes", ASME/JSME Thermal Eng. Joint Conf., 1987, Vol 3, pp 51-61
26. Inoue, M., Hara, K. and Furukawa, M., 1987, "Experimental Study on the Three-Dimensional Flow Field in a Turbine Scroll," 87-TOKEY-IGTC-9
27. Inversen, H., Rolling, R., Carlson, J. (1960), "volute pressure distribution, radial force on the impeller and volute mixing losses of a radial flow centrifugal pump", ASME J. Engr for Power, Vol. 82, No. 2, April 1960, pp 136-144
28. Jean-Luc Di Liberti, Michael Cave, 2003, ""AeroTest Rig: Summary of A2 Stages Tests"
29. Jose Gonzalez, Joaquin Fernandez, Eduardo Blanco and Carlos Santolaria, 2002, "Numerical Simulation of the Dynamic Effects Due to Impeller-Volute Interaction in a Centrifugal Pump", ASME, Journal of Fluids Engineering, Vol. 124, pp. 348-355
30. Kurokawa, J. (1980), "Theoretical determinations of the flow characteristics in volute", IAHR-AiRH Symposium 1980, Tokyo.
31. Lopez Pena F. (1987), "Study of volutes for centrifugal compressors with constant cross sectional area and simple geometry", VKI PR 1987-05, June 1987
32. Loret, J.A., Gopalakrishnan, S. (1986), "Interaction between impeller and volute of pumps at off design conditions", ASME J. Fluids Engineering, Vol. 108, No. 1, March 1986, pp 12-18
33. Ojeda, W. de, Flack, R.D., Miner, S.M. (1992), "Pressure distributions in a single and two versions of a double volute of a centrifugal pump", ASME Paper 92-GT-20
34. Owarish, H. O., Ilyas, M. and Bhinder, F.S., 1992, "A Two-Dimensional Flow Analysis Model for Designing a Nozzle-less Volute Casing for Radial Flow Gas Turbines," ASME Journal of Turbomachinery, Vol. 114, pp. 402-410
35. Sideris, M. (1988), "Circumferential distortion of the flow in centrifugal compressors due to outlet volutes", PhD. Thesis, RUG-VKI, April 1988

36. Sorokes, J.m., Borokes, C. and Koch, J.M., 1998, "Investigation of the Circumferential Static Pressure Non-Uniformity Caused by a Centrifugal Compressor discharge Volute," ASME Paper No. 98-GT-326
37. TASCflow Version 2.10 and 2.11 Users Online Manual.
38. Tabakoff, W, Sheoran, Y., and Kroll, K., 1980, "Flow Measurements in a Turbine Scroll," ASME Journal of Fluids Engineering, Vol. 102, pp. 290-296
39. Tabakoff, W., Vittal, B. and Wood, B., 1984, "Three-dimensional Flow Measurements in a Turbine Scroll," ASME Journal of Engineering for Gas Turbines and Power," Vol. 106, pp. 516-522
40. Thomas, R.N., Kostrzewsky G.J., Flack R.D. (1986), "Velocity measurements in a pump volute with a non-rotating impeller", Int. J. Heat and Fluid Flow, Vol. 7, No. 1, March 1986, pp 11-20
41. Vn den Braembussche, R. A., and Hande, B. M., 1990, "Experimental and Theoretical Study of the Swirling Flow in Centrifugal Compressor Volumes", ASME Journal of Turbomachinery, Vol. 112, pp. 38-43
42. Van den Braembussche, R. A., Ayder, E., D., Hagelstein, M. Ratenberg and R. Keiper, 1999, "Improved Model for the Design and Analysis of Centrifugal Compressor Volumes", ASME Journal of Trubomachinery, Vol. 121, pp. 619-625
43. Varghese, G., Kumar, T. C. Mohana and Rao, Y. V. N., 1978, "Influence of Volumes Surface Roughness on the Performance of a Centrifugal Pump", ASME J. of Fluids Engineering, Vol. 100, pp 473-476
44. Weber, C.R., Koronowski, M.E. (1986), "Meanline performance prediction of volutes in centrifugal compressors", ASME Paper 86-GT-216
45. Whitfield, A. and Mohd Noor, A.B., 1994, "Design and Performance of Vaneless Volumes for Radial Inflow Turbines Part 1: Non-dimensional Conceptual Design Considerations," ImechE, Vol. 208, pp. 199-211
46. Wilson, D. G., 1993, "The Design of High-Efficiency Trubomachinery and Gas Turbines", The MIT Press, Sixth printing.

MICHIGAN STATE UNIVERSITY LIBRARIES



3 1293 02504 2320